University of Cambridge
Department of Engineering
Trumpington Street
Cambridge, CB2 1PZ, UK

Deployment of a Rigid Panel by Tape-Springs

K.A. Seffen and S. Pellegrino

CUED/D-STRUCT/TR 168

Release date: August 1997

Abstract

Tape-springs are straight, thin-walled strips with a curved cross-section. Following recent proposals for large deployable structures exploiting the structural simplicity and robustness of such springs as deployment actuators, this report presents a study of the deployment of a panel by short tape-springs mounted in parallel. It is shown that a spring deforms by forming an elastically deformed region with zero transverse curvature and uniform longitudinal curvature. It is also shown that the moment-rotation relationship of a tape-spring whose length is systematically varied exhibits properties that are independent of the length. A key feature is that the moment-rotation relationship for many tape-spring geometries can be obtained from relatively few finite-element analyses. It is demonstrated, by theory and experiment, that mounting tape-springs in pairs, with their centres of curvature on opposite sides, results in an energy well which traps the kinetic energy of the panel on lock-out. The panel does not overshoot its fully deployed configuration and disturbance to the spacecraft is thus prevented.

Acknowledgements

Financial support from Matra-Marconi Space UK Ltd is gratefully acknowledged. The first author has been supported by a Research Studentship from EPSRC. The authors thank their colleagues Dr P.J. Long and Dr A. Britto for helping in the design of the panel deployment experiment and the finite-element analysis, respectively. Technical assistance has been provided by Mr R.J. Denston, Mr P.J. Knott, and Mr S. Robertson.

Contents

Principal Nomenclature

$\dot{}$, $\ddot{}$	first and second time derivatives, respectively
$a,\ b,\ c$	perpendicular components of cable length
a_j, a_p	centroidal position of suspension system jib and panel, respectively
$A_1,\ A_2$	areas used in equal area calculations
c'	dimensionless damping factor
$C_x,\ C_y$	coordinates of centre of rotation of panel
D	flexural stiffness of tape-spring
$\mathbf{e}$, $\mathbf{e}^*$	unit vectors
E	Young's Modulus
f_n	natural frequency of vibration of panel
g	acceleration due to gravity
$\mathbf{i},\ \mathbf{j},\ \mathbf{k}$	fixed unit vectors
$I_j,\ I_p,\ I_w$	moment of inertia about centroid of suspension jib, panel and counterweight, respectively
k	initial stiffness of composite hinge
l_j	length of suspension system jib
L	length of tape-spring
$\mathcal{L}$	Lagrangian
$m_j,\ m_p,\ m_w$	mass of suspension jib, panel and counterweight, respectively
M	bending moment (> 0 if it induces opposite-sense bending)
M_+^{max}	peak moment for opposite-sense bending (> 0)
M_-^{max}	peak moment for equal-sense bending (< 0)
M_+^*	fold propagation moment (> 0)
M_-^*	fold propagation moment (< 0)
n	number of pairs of composite tape-spring hinges
$p_1,\ p_2$	tape-spring lengths either side of fold
q_i	generalised coordinate
Q_i	generalised force
$\mathbf{r}$	position vector
R	transverse radius of curvature (undeformed configuration)
t	thickness of tape-spring; time
T	kinetic energy; period of vibration
U	strain energy
z_j	height of suspension system above panel

α	angle of embrace of cross-section
β	suspension system angular coordinate
κ_l, κ_t	longitudinal and transverse curvature changes, respectively
ν	Poisson's ratio
θ	relative rotation between opposite ends of tape-spring; fold angle
θ_+^{max}	relative rotation at maximum moment for opposite-sense bending
θ_-^{max}	relative rotation at maximum moment for equal-sense bending
θ_+^{heel}	relative rotation at snap back during unloading (opposite-sense bending)
θ_-^{ramp}	relative rotation during local-buckling for equal-sense bending
θ_0	initial deployment angle of composite tape-spring hinge

Chapter 1

Introduction

1.1 Deployable Structures

The study of deployable structures is a rapidly evolving technology that deals with the development of structures that can change their geometric and structural properties to meet operational requirements. Everyday examples include umbrellas, folding chairs, tents, *etc.* More complex examples exist in the field of aerospace applications. Spacecraft structures, for example, must be efficiently compacted into relatively small payload volumes for launch before being successfully deployed in orbit. Two deployment methods are used: *controlled* deployment, and *free* deployment. Controlled deployment usually involves an expansion of the structure by means of motors and cables. Free deployment is achieved by releasing the elastic strain energy stored within the folded structure.

1.2 Review of Previous Work

This section highlights work carried out on the bending of *tape-springs*. Tape-springs are thin, transversely curved strips similar to tape-measures and are made from copper beryllium (CuBe) alloy. They have a unique ability to fold/unfold elastically and to *lock* when fully straightened. This property is exploited in actuating free deployment of aerospace structures.

1.2.1 Bending of Tape-springs

The geometry of a typical tape-spring is shown in Fig. 1.1. The cross-section is a uniform, circular arc that subtends an angle α of the order of 180°. The natural radius of the cross-section is R, its thickness is t and the length of the tape-spring is L. Tape-springs are made from flat strips of annealed CuBe pressed into a cylindrical mould and then heat-treated in a furnace. This process *age-hardens*

the CuBe and its material properties are given in Table 1.1.

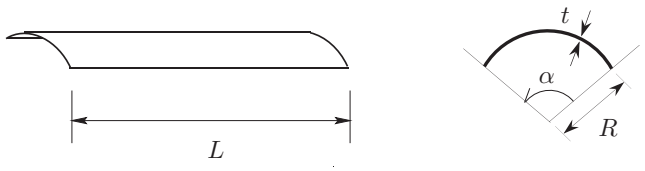

Figure 1.1: Geometry of a tape-spring.

Bending of the tape-spring within its plane of symmetry produces different responses depending on the direction of bending with respect to the direction of curvature of the spring; a tape is said to undergo *opposite-sense bending* if the longitudinal and transverse curvatures are in the opposite sense, see Fig. 1.2(a). A bending moment M that induces opposite-sense bending is defined to be positive, and the corresponding relative rotation θ between the ends is also defined to be positive. Conversely, *equal-sense bending* of a tape, under $M < 0$, induces longitudinal and transverse curvatures that are in the same sense and hence $\theta < 0$, see Fig. 1.2(b).

Young's modulus, E $[N/mm^2]$	131000
yield stress, σ_y $[N/mm^2]$	1175
Poisson's ratio, ν	0.3

Table 1.1: Properties of heat-treated CuBe.

The bending of tape-springs is highly non-linear, and is best explained with reference to the schematic diagram shown in Fig. 1.3.

For small rotations, the applied moment M varies linearly with the relative end rotation θ as the tape bends into a smooth curve.

For opposite-sense bending, as the rotation increases, the cross-section begins to flatten, this effect being most pronounced in the middle, and the moment approaches M_+^{max}. Then, suddenly, the centre part of the tape *snaps through* and the deformation localises in a short, longitudinally curved region, Fig. 1.2(a.ii), while the moment decreases very quickly. In Fig. 1.3 this corresponds to the jump from point A, at the "nose" of the opposite-sense bending curve, to point B. As M decreases, the rest of the tape becomes approximately straight. Then, as the relative rotation is further increased and the ends move closer together, the moment, M_+^*, remains approximately constant (point B to point C); the longitudinal curvature in the central fold is also constant and approximately equal to R, only the arc-length of this fold increases. When the direction of turning is reversed the same path is followed, but when point B is reached the moment does not jump up to point A. Instead, it continues at the same constant level until

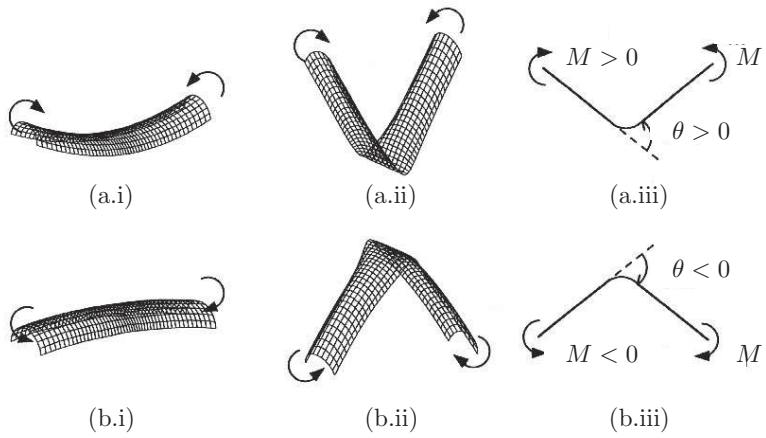

Figure 1.2: Perspective views of tape-springs subject to end moments. (a) *Opposite-sense bending* under a positive bending moment: (i) initial, smoothly-curved deformation; (ii) post-buckled shape; (iii) schematic diagram defining positive relative rotation θ. (b) *Equal-sense bending* under a negative moment.

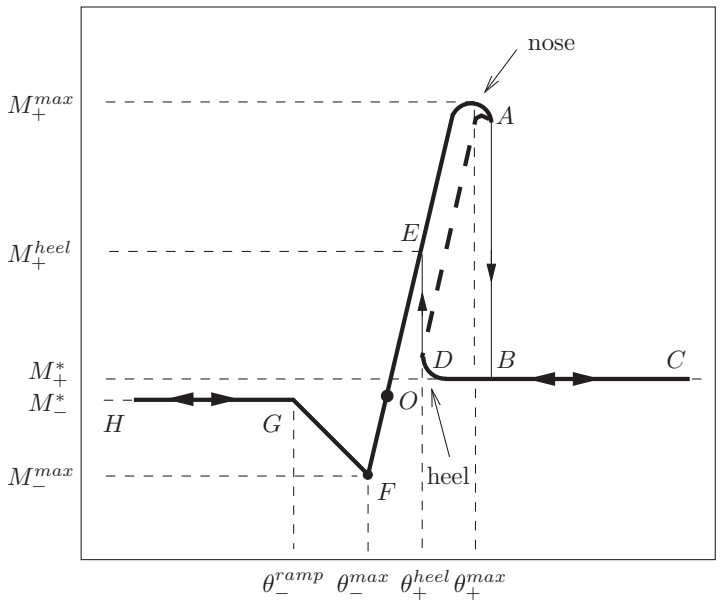

Figure 1.3: Schematic $M(\theta)$ diagram; the origin is at point O. Arrows show the direction in which each part of the path can be followed. The broken line from A to D is unstable.

point D, the "heel" of the opposite-sense bending curve, and at θ_+^{heel} it snaps to point E, which corresponds to a value of M much lower than that attained upon loading. Finally, the path returns to the origin O following the same straight path

followed upon loading.

If the tape-spring is bent in the equal-sense direction, it exhibits a softer response, and the linear behaviour ends much sooner. There is a sudden bifurcation at M_{-}^{max} that results in a flexural-torsional deformation mode with asymmetric, torsional folds near the ends. As the relative end rotation increases, these torsional folds grow in amplitude while they move towards the middle of the tape-spring, as the applied moment decreases. Finally, they coalesce into a central, symmetric fold of moment M_{-}^{*} which has the same characteristics described for opposite-sense bending, Fig. 1.2(b.ii). When θ is decreased, the unloading path practically coincides with the loading path.

Practical tape-springs often have their ends rigidly encased to provide a firm connection between the springs and the surrounding structure. This can be achieved by bonding the ends of the tape-spring to Perspex blocks with epoxy resin; the principal axes of bending of each tape coincides with the centre lines of the blocks. If the tape-spring is sufficiently short, then these rigid ends may constrain flattening of the section under an applied moment. The initial bending stiffness therefore increases as the length of the tape-spring decreases. This effect is more marked for bending in the equal-sense direction; the degree of associated twisting diminishes and the fold may form by snapping through.

1.2.2 Prediction of Moment-Curvature Relationship

Theoretical moment-curvature relationships for tape-springs have been derived by three different authors. The derivation by Wüst (1954) was based on equilibrium considerations and linearised shell theory. Similarly, Rimrott (1966*b*) used energy methods to obtain a non-linear bending expression. Both methods, however, do not describe the associated twisting of the tape-spring when bent in the equal-sense direction. It was Mansfield (1973) that solved this aspect using large deflexion shell theory and variational methods.

All of the above methods were set up with respect to a unit length of tape-spring deforming uniformly. In essence, this implies that end-effects are not considered and that the resulting moment-curvature relationships apply only to long tape-springs.

Numerical predictions where end-effects were included were obtained by Fischer (1995) using finite element analysis. However, the bifurcation into a twisting mode during equal-sense bending was not captured.

A full comparison of the above methods is given by Seffen (1997).

1.3 Aims of the Project and Outline of Report

Matra-Marconi Space UK propose to use tape-springs to deploy a panel from a spacecraft. The panel is essentially rigid and its inertia properties are given. The panel is connected to the main body of the spacecraft by a series of parallel tape-springs, which are relatively short compared to the overall dimension of the panel, and hence, act like finite-length hinges. The deployment of the panel is governed by the combined bending response of these short tape-springs.

Therefore, this study involves the following steps:

- prediction of the moment-rotation behaviour of single tape-springs, for a large range of section geometries;
- deployment performance of a set of tape-springs mounted in parallel;
- design of a gravity-compensated testing apparatus for deploying a rigid panel of variable inertia properties;
- deployment experiments and theoretical modelling;
- evolution of design criteria for deployment of a generic rigid panel.

Chapter 2 begins by presenting detailed data obtained from a finite-element analysis and then quantifies the key features of the moment-rotation relationship of relatively short tape-springs with fixed ends, for a wide range of section geometries.

Chapter 3 investigates the deployment of a mass attached to the tip of a single, short tape-spring. Key issues that are addressed are the folding and deployment of such a system, and the ability of a tape-spring at the end of deployment to straighten out and *lock* the structure into its operational configuration. It is shown that pairs of identical tape-springs, mounted with their centres of curvature on opposite sides, thus forming a "composite hinge", can deploy a mass from an initial folded angle to its intended configuration without overshoot.

The design of a panel, whose inertia properties are similar to panels currently used on spacecraft, is detailed in Chapter 4 along with a suspension system that compensates for the effects of gravity during deployment.

Chapter 5 presents experimental results of the deployment of a panel by two sets of composite tape-spring hinges. A conservative, two-degree of freedom model is derived to take account of the dynamic interaction between the panel and the compensation system during deployment. The predicted deployment behaviour is validated by experiment.

Finally, Chapter 6 considers how the geometry of a composite hinge may be determined using a series of design criteria.

Chapter 2

Moment-Rotation Relationship

The deployment behaviour of a panel connected to a rigid support by a set of tape-springs is dictated by the moment-rotation behaviour of the tape-springs. Available theoretical methods do not sufficiently describe the bending response of short tape-springs with encased ends, as mentioned in Chapter 1. Therefore, this behaviour was computed by means of a finite element analysis. Section 2.1 details a typical finite-element analysis which produces the moment-rotation relationship of a tape-spring with encased ends. Section 2.2 then investigates how the moment-rotation relationship changes when the length and geometric properties of a tape-spring are systematically varied. These relationships are compared and the variations of M_+^{max}, M_-^{max}, M_+^*, M_-^*, θ_+^{max}, θ_+^{heel} and θ_-^{ramp} —which is defined in Section 2.2— with tape-spring geometrical and material parameters are characterised in Section 2.3.

2.1 Finite-Element Analysis

A comparison of the measured moment-rotation relationship of a tape-spring with a finite-element analysis carried out using the finite-element package ABAQUS (Hibbit et al. 1994) is shown in Fig. 2.1. This plot was taken from Fischer (1995).

The tape-spring is modelled by a mesh of S4R5 shell elements: each element is a quadrilateral with four corner nodes, each with five degrees of freedom (three displacement components and two in-plane rotation components). The displacement field within the element is bilinear, and reduced integration with a single Gauss point is used. A typical mesh consists of five elements forming half of the cross-section of the tape (the other half does not need to be modelled because of symmetry) and 48 elements along the length of the tape. Two additional, reference nodes are defined, one on each end section of the tape-spring and coinciding with the centroid of the cross-section.

All nodes lying at either end of the tape are kinematically constrained to the

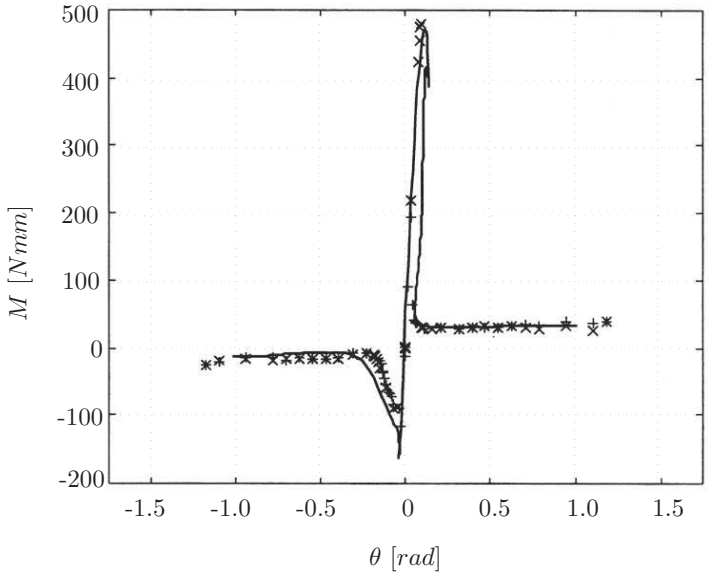

Figure 2.1: $M(\theta)$ relationship for tape-spring with $L = 200\ mm$, $t = 0.1\ mm$, $R = 13.3\ mm$, and $\alpha = 1.85\ rad$. Measurements taken upon loading and unloading denoted by $\times$ and $+$, respectively. Finite-element predictions shown by a continuous line.

corresponding reference node and global kinematic constraints are applied to the reference nodes only. Thus, one reference node is allowed only to rotate about a horizontal axis through the centroid, while the other reference node is allowed to translate in the longitudinal direction and to rotate about a horizontal axis through the centroid. Nodes lying on the longitudinal plane of symmetry are constrained to remain within that plane, but no rotational constraints are applied to these nodes.

Equal and opposite bending couples M are applied at the two reference nodes and the corresponding rotations are calculated.

The two standard solution procedures used in non-linear structural analysis, load incrementation and displacement incrementation, are unsuitable in the present case because neither $M(\theta)$ nor $\theta(M)$ are single-valued functions. The only procedure that can capture the type of behaviour seen in the experiments is the arc-length method pioneered by Riks (1972) and extensively discussed in Chapter 9 of Crisfield (1991). This method can compute a series of points forming a continuous equilibrium path in generalised load/displacement space by controlling the distance, or arc-length, between successive points. The arc-length option available in ABAQUS has been used for all finite-element simulations detailed in this report. Once an optimal set of convergence parameters had been found by a lengthy process of trial and error, generating the complete $M,\ \theta$ equilibrium path for all tape-springs of interest became a straightforward matter.

Note also that for $M < 0$ the finite-element analysis does not capture the torsional buckling of the tape-spring. Instead, it predicts the formation of a local buckle in the wall of the tape, and hence a larger $|M_{-}^{max}|$. It appears that ABAQUS is unable to capture bifurcation points during the course of a geometrically non-linear analysis, and hence the only way of improving these predictions is by seeding an initial imperfection.

2.2 Behaviour of Finite-Length Springs

This section provides insight on the effects of shortening the length of a tape-spring with encased ends on its moment-rotation relationship. More detailed information is obtained from Fig. 2.2, which shows moment-rotation plots for opposite-sense bending of tape-springs with identical cross-sections, of parameters $R = 10\ mm$, $t = 0.1\ mm$ and $\alpha = \ 1.92\ rad$ (110°), but different lengths. Each curve was obtained using the finite-element package ABAQUS. The largest peak moment, M_{+}^{max}, occurs in the shortest tape-spring with a length of 100 mm. Increasing L in steps of 50 mm gradually decreases these peak moments. As expected, the longer the tape-spring becomes, the smaller the influence of the constraint applied by the rigid ends to the flattening of the section in the middle of the tape. Thus, the tape-spring becomes softer and initiation of the fold takes place at a lower bending moment.

The post-buckled behaviour is essentially the same for all lengths, as all plots converge onto a single line. The same constant moment, M_{+}^{*}, is therefore associated with all folds. The rotations corresponding to the heel of each curve vary marginally compared to the peak moment rotations, and appear to tend to a particular value as the length of the tape-spring decreases.

Figure 2.3 shows the moment-rotation relationships for equal-sense bending of a tape-spring with the same cross-sectional geometry as in Fig. 2.2. These curves were also obtained using ABAQUS. The length of the stiffest spring is 100 mm, other lengths that have been analysed are 200 mm and 300 mm. The initial slope of each curve is equal to the pre-buckled stiffness for opposite-sense bending of the same tape-spring. It was noted in the previous section that ABAQUS is unable to capture the bifurcation leading to torsional buckling. Instead, it predicts the formation of a local buckle in the middle of the tape-spring due to compressive bending stresses along the free edge. The initiation of this buckle occurs at the same peak bending moment, M_{-}^{max}, regardless of the length L of the tape-spring. In all cases, the complete formation of the fold is indicated by the plots converging onto a single, constant moment line at a relative rotation θ of about 1 rad.

In practice, end effects cause the asymmetric, torsional folds of Section 1.2.1 to form closer towards the middle of the tape-spring, as L is decreased. Sufficiently short tape-springs will buckle locally in the middle, in preference to forming torsional folds. For the lengths analysed in this section, local buckling occurs in

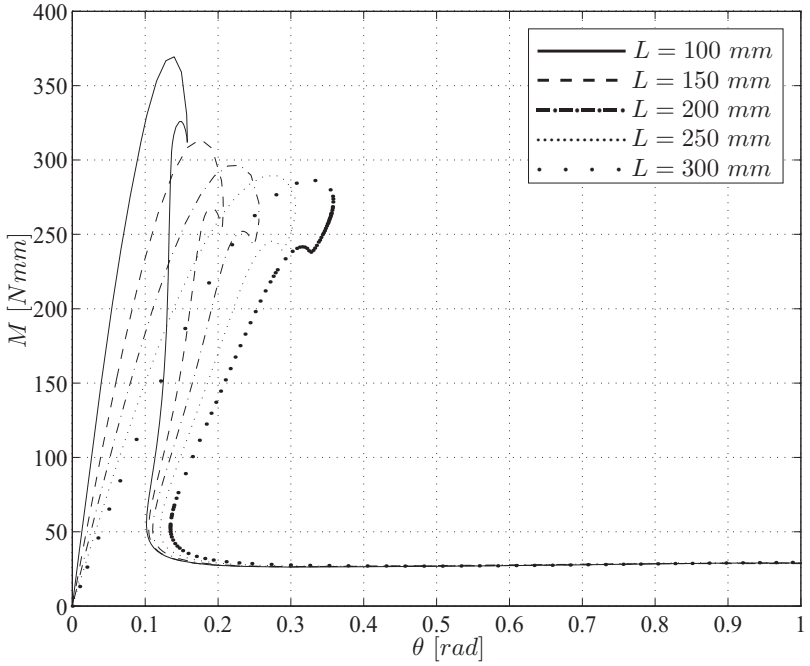

Figure 2.2: Opposite-sense bending of tape-springs with finite length L, $R = 10\ mm$, $t = 0.1\ mm$ and $\alpha = 110°$.

preference to torsional buckling, and hence the finite-element results that are presented are accurate for equal-sense bending.

A final point concerns the portion of the moment-rotation curves between M_{-}^{max} and where the gradient first becomes zero, see Figure 2.3. The rotation associated with this point is denoted by θ_{-}^{ramp}, as the moment-rotation relationship *ramps* down to this value after local buckling has begun. The *difference* in rotations between points on different curves but corresponding to the same moment varies linearly from zero at θ_{-}^{ramp} to a maximum value at M_{-}^{max}. This would indicate that the point of zero slope and the behaviour thereafter are also independent of the length of the tape-spring.

Thus, for a decreasing length of tape-spring, the following may be stated:

- M_{+}^{max} increases;
- θ_{+}^{heel} is approximately the same for relatively short tape-springs;
- M_{+}^{*} and M_{-}^{*} do not vary with L;
- M_{-}^{max} remains the same and the initial bending behaviour is linear, with the same stiffness as for the initial opposite-sense bending, up until this value;

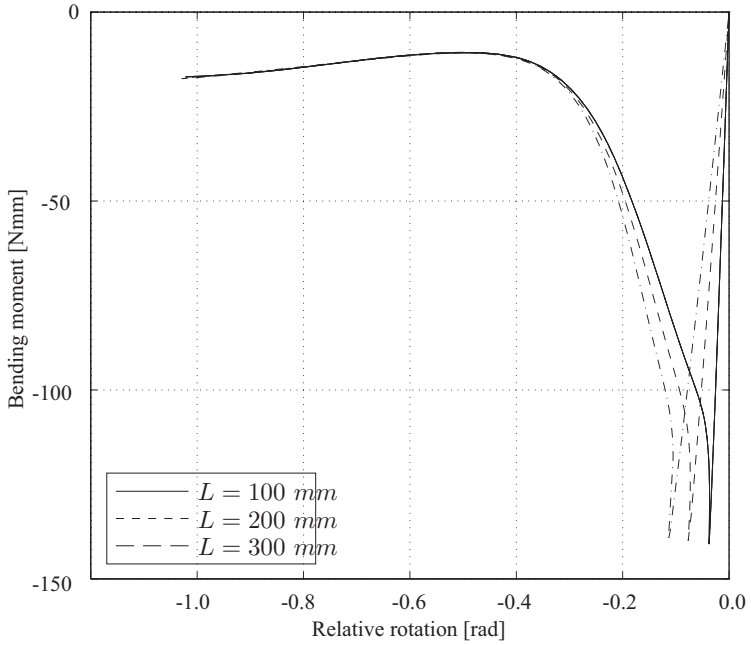

Figure 2.3: Equal-sense bending of tape-springs with finite length L. Geometry of cross-section is the same as in Fig. 2.2.

- for equal-sense bending, the rotation at which the gradient first becomes zero after local buckling, θ_{-}^{ramp}, and the response thereafter, including the rotation at which the fold forms completely, are independent of L;
- the initial slope, before buckling, increases for bending in both senses.

Hence, for opposite-sense bending, the moment-rotation relationship from the heel onwards of a relatively short tape-spring can be obtained from the known relationship of a single length of tape-spring. The same is true for equal-sense bending, from the first point of zero gradient after the peak until complete fold formation. Also, M_{-}^{max} is the same. Separate analyses, however, are necessary to determine the behaviour of different lengths of tape-spring before snap-through in the opposite-sense direction. From this, the value of the initial slope can be used to calculate θ_{-}^{max}, assuming linear behaviour. The portion of the curve that ramps up from the zero gradient point to M_{-}^{max} can be generated from the known relationship by noting that the corresponding rotations vary linearly with L. The region between the nose and the heel of each curve is not required, since this portion of the curve is unstable and, hence, it is of no practical interest.

Therefore, knowledge of a single complete moment-rotation relationship and of the pre-buckled opposite-sense behaviour of the specific tape-spring of interest are all that is required to construct the bending response for a short tape-spring of any length. Thus, computation times can be greatly reduced as only one fully

non-linear finite-element solution is required. This approach is applied to many tape-spring geometries in the following section.

2.2.1 Detailed Results

To avoid yielding the material in the fold region the following limits have to be satisfied by the ratio R/t, see Eq. 6.25

$$\frac{R}{t} \geq \frac{E}{\sigma_y(1+\nu)} \tag{2.1}$$

All tape-springs tested in the course of the present study were made from CuBe sheet of thickness 0.1 mm. However, it was thought that future applications might require greater values of t. Therefore, it was decided to investigate numerically tape-springs with three different thicknesses, *i.e.* $t = 0.1\ mm$, $0.2\ mm$, and $0.3\ mm$. Using Eq. 2.1 and the values of E, ν and σ_y from Table 1.1, the minimum value of R was determined for each of these thicknesses. These values are given in Table 2.1 together with the particular radii that were then chosen to be analysed.

t $[mm]$	minimum R from Eq. 2.1 $[mm]$	values of R $[mm]$
0.1	8.6	10, 20, 30
0.2	17.2	20, 30
0.3	25.8	30

Table 2.1: Range of section thicknesses and radii analysed using ABAQUS.

Fischer (1995) showed that sensible correlations between experimental results and results from a finite-element analysis can only be made for tape-springs with $\alpha = 1.55\ rad$ (89°) and upwards. A separate investigation has also indicated that it is impossible to form a fold by the application of end couples alone for opposite-sense bending of tape-springs with $\alpha > 180°$. Therefore, the range of α was chosen to be from 90° to 170°; in steps of 20° for a thickness of section of $0.1\ mm$, and in steps of 40° for $t = 0.2\ mm$ and $t = 0.3\ mm$ — for each value of R.

For each set of cross-sectional properties, a *master* finite-element analysis was performed using ABAQUS to obtain the complete moment-rotation relationship. This analysis provided the response parameters that are unaffected by a variation in the length of the tape-spring.

For each master simulation, the length of tape-spring was chosen to be $8R\alpha$ or a longer multiple of $R\alpha$, if a complete solution could not be obtained for a length of $8R\alpha$. These lengths are indicated in Tables 2.2 and 2.3 for opposite-sense bending and equal-sense bending, respectively. The number of elements in each

mesh refers to the number in the longitudinal direction followed by the number in the transversal direction.

R $[mm]$	α $[^\circ]$	t $[mm]$	L $[\times R\alpha]$	no. and type of elements	mesh bias	residual tolerances
10	170	0.1	16	48 ×5, S4R5	1.03	10^{-7}, 10^{-1}
10	150	0.1	10	48 ×5, S4R5	1.03	10^{-7}, 10^{-1}
10	130	0.1	8	48 ×5, S4R5	1.01	10^{-7}, 10^{-1}
10	110	0.1	8	48 ×5, S4R5	1.03	10^{-7}, 10^{-1}
10	90	0.1	8	48 ×5, S4R5	1.03	10^{-7}, 10^{-1}
20	170	0.1	22	64 ×5, S4R5	1.02	10^{-7}, 10^{-1}
20	170	0.2	14	48 ×5, S4R5	1.02	10^{-7}, 10^{-1}
20	150	0.1	14	64 ×5, S4R5	1.02	10^{-7}, 10^{-1}
20	130	0.1	12	64 ×5, S4R5	1.02	10^{-7}, 10^{-1}
20	130	0.2	8	48 ×5, S4R5	1.02	10^{-7}, 10^{-1}
20	110	0.1	8	48 ×5, S4R5	1.01	10^{-7}, 10^{-1}
20	90	0.1	8	48 ×5, S4R5	1.02	10^{-7}, 10^{-1}
20	90	0.2	8	48 ×5, S4R5	1.03	10^{-7}, 10^{-1}
30	170	0.2	18	48 ×5, S4R5	1.05	10^{-7}, 10^{-1}
30	170	0.3	14	64 ×5, S4R5	1.01	10^{-7}, 10^{-1}
30	150	0.1	18	48 ×5, S4R5	1.05	10^{-7}, 10^{-1}
30	130	0.1	14	48 ×5, S4R5	1.05	10^{-7}, 10^{-1}
30	130	0.2	14	64 ×5, S4R5	1.01	10^{-7}, 10^{-1}
30	130	0.3	14	64 ×5, S4R5	1.01	10^{-7}, 10^{-1}
30	110	0.1	12	48 ×5, S4R5	1.01	10^{-7}, 10^{-1}
30	90	0.1	8	48 ×5, S4R5	1.01	10^{-7}, 10^{-1}
30	90	0.2	8	48 ×5, S4R5	1.01	10^{-7}, 10^{-1}
30	90	0.3	8	48 ×5, S4R5	1.03	10^{-7}, 10^{-1}

Table 2.2: Tape-spring geometries for which a master analysis has been carried out, for opposite-sense bending.

Also detailed are the dimensions of each finite-element mesh — namely the type of elements used to construct each mesh, and the "mesh-bias". This is the ratio, for successive elements in the longitudinal direction from one end to the middle of the tape-spring, between the square of the length and the square of the width. Thus, for a mesh-bias of "1", the mesh comprises elements of the same longitudinal length. A mesh-bias greater than unity indicates a higher concentration of nodes towards the centre of the tape-spring, to provide a denser mesh where the largest changes in curvature occur. The most important measure of convergence —the tolerances for the force and moment residuals during the course of the solution— had to be redefined from their default values in ABAQUS. Their values were obtained by trial and error and are indicated in the tables.

R $[mm]$	α $[^\circ]$	t $[mm]$	L $[\times R\alpha]$	no. and type of elements	mesh bias	residual tolerances
10	170	0.1	5	48 ×5, S4R5	1.05	10^{-6}, 10^{-1}
10	150	0.1	5	48 ×5, S4R5	1.03	10^{-7}, 10^{-1}
10	130	0.1	5	48 ×5, S4R5	1.05	10^{-7}, 10^{-1}
10	110	0.1	8	48 ×5, S4R5	1.03	10^{-7}, 10^{-1}
10	90	0.1	8	48 ×5, S4R5	1.03	10^{-7}, 10^{-1}
20	170	0.1	6	96 ×10, S8R5	1.00	10^{-6}, 10^{-1}
20	170	0.2	4	48 ×5, S4R5	1.02	10^{-6}, 10^{-1}
20	150	0.1	6	96 ×10, S8R5	1.00	10^{-6}, 10^{-1}
20	130	0.1	6	96 ×10, S8R5	1.05	10^{-6}, 10^{-1}
20	130	0.2	4	48 ×5, S4R5	1.05	10^{-6}, 10^{-1}
20	110	0.1	6	96 ×10, S8R5	1.05	10^{-7}, 10^{-1}
20	90	0.1	4	48 ×5, S4R5	1.05	10^{-6}, 10^{-1}
20	90	0.2	8	48 ×5, S4R5	1.05	10^{-6}, 10^{-1}
30	170	0.2	6	48 ×5, S4R5	1.05	10^{-6}, 10^{-1}
30	170	0.3	5	48 ×5, S4R5	1.05	10^{-6}, 10^{-1}
30	150	0.1	6	96 ×10, S8R5	1.00	10^{-6}, 10^{-1}
30	130	0.1	6	96 ×10, S8R5	1.00	10^{-6}, 10^{-1}
30	130	0.2	4	48 ×5, S4R5	1.05	10^{-6}, 10^{-1}
30	130	0.3	4	48 ×5, S4R5	1.05	10^{-6}, 10^{-1}
30	110	0.1	6	96 ×10, S8R5	1.00	10^{-6}, 10^{-1}
30	90	0.1	6	96 ×10, S8R5	1.05	10^{-6}, 10^{-1}
30	90	0.2	8	48 ×5, S4R5	1.05	10^{-6}, 10^{-1}
30	90	0.3	8	48 ×5, S4R5	1.05	10^{-6}, 10^{-1}

Table 2.3: Tape-spring geometries for which a master analysis has been carried out, for equal-sense bending.

For equal-sense bending, it was sometimes difficult to initiate a buckle in the middle of the tape-spring using S4R5 elements, irrespective of the mesh density and the number of elements. This problem was overcome by either using S8R5 elements, which are 8-noded versions of the S4R5 thin-shell element; or by extending the boundary conditions applied to the reference nodes at either end of the mesh to some nodes along the axis of the tape-spring, thus constraining those parts to rotate like a rigid body and cause the fold to form in the middle of the tape-spring. The same technique had been used by Fischer (1995). The former method resulted in computation times approximately increasing fourfold for a complete solution, compared to simulations using S4R5 elements.

Figures 2.4 - 2.6 summarise the length independent parameters determined from these master simulations.

The values of θ_+^{heel} are plotted in Fig. 2.4, and the magnitudes of M_-^{max} in

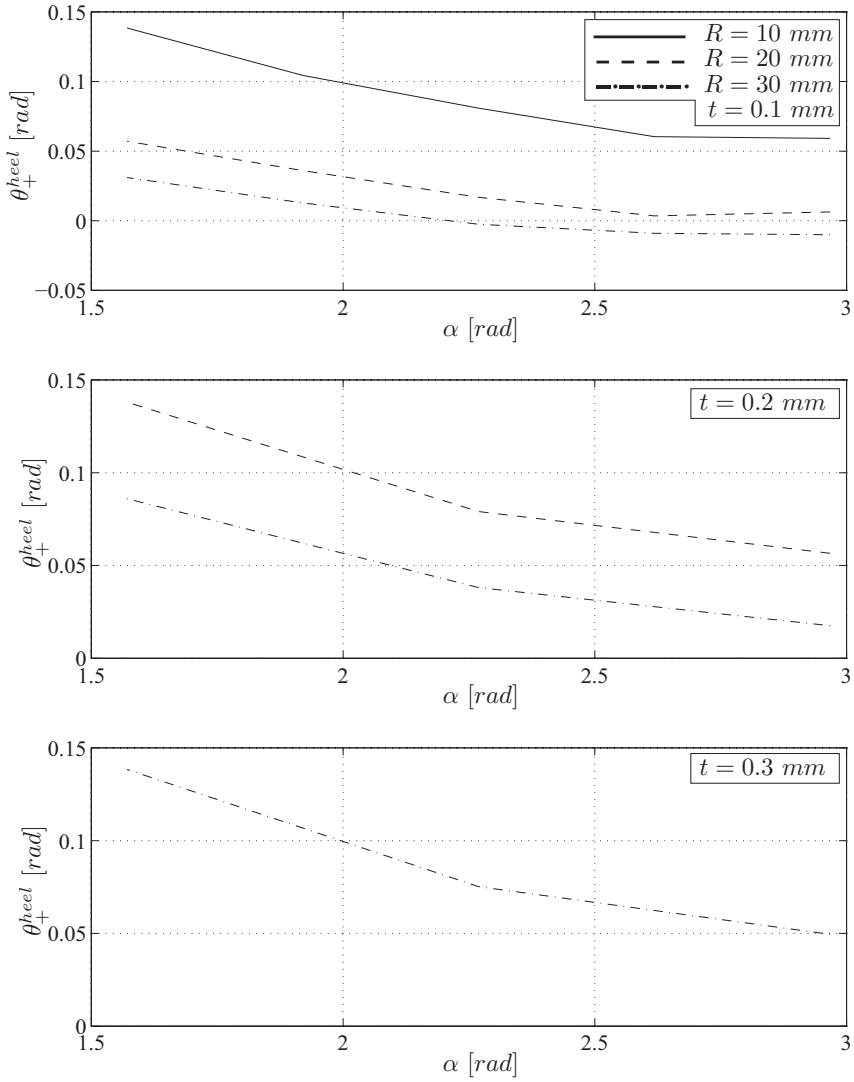

Figure 2.4: Variation of relative end rotation at the "heel", for opposite-sense bending.

Fig. 2.5, against α. Figure 2.6 indicates the values of θ at which the gradient first becomes zero, θ_+^{ramp}, and the associated bending moment, for equal-sense bending.

Secondary finite-element analyses were then performed for spring lengths of $4R\alpha$, $6R\alpha$ and $8R\alpha$, for each of the tape-spring geometries in Table 2.2, to obtain the information on opposite-sense that cannot be obtained from the master analysis. In each of these, 48×5 S4R5 elements were used, along with force and moment residual tolerances of 10^{-7} and 10^{-1}, respectively. Following the assumptions of Section 2.2, the results of these analyses make it possible to construct complete moment-rotation relationships for the full range of tape-springs. Additional secondary analyses were carried out for lengths of $16R\alpha$ and the values of M_+^{max} and

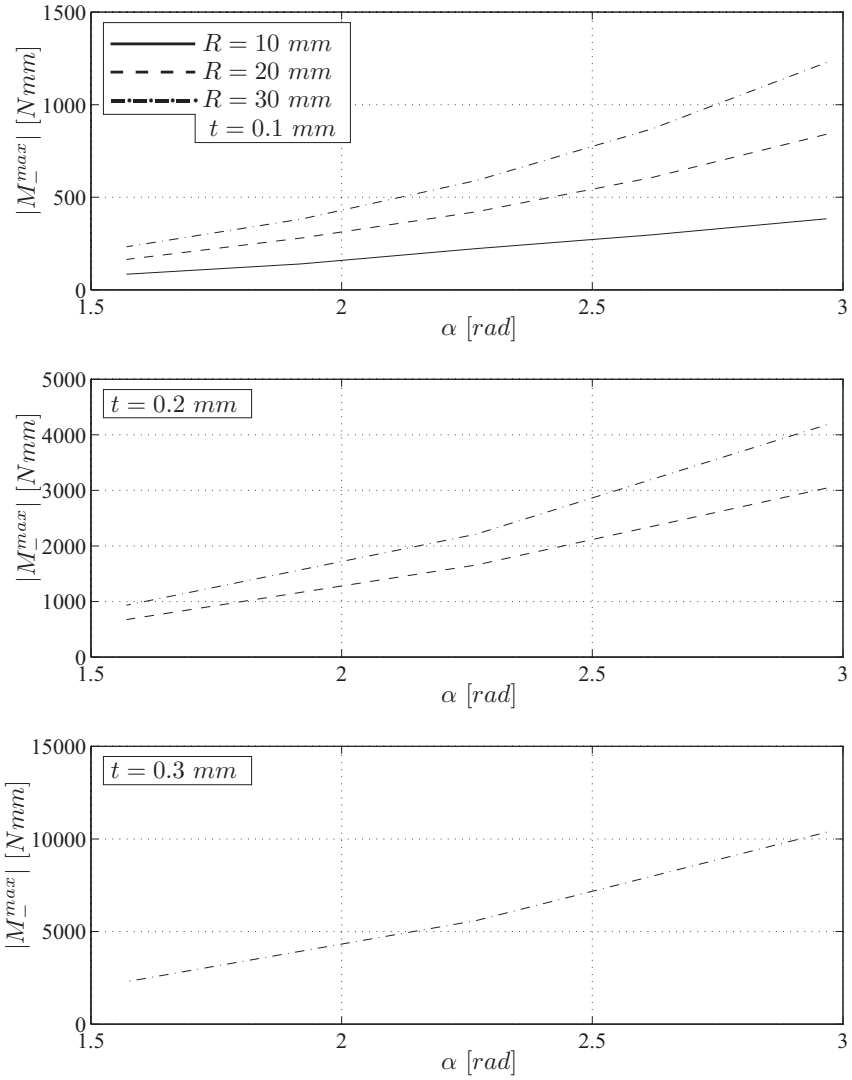

Figure 2.5: Variation of peak moment value $|M_{-}^{max}|$, for equal-sense bending.

θ_{+}^{max} thus obtained will be used in Section 2.3.

Figure 2.7 shows a representative plot in dimensionless form, for opposite-sense bending. Complete plots for all geometries that have been analysed are shown in Appendix A. The dimensionless bending moment is calculated by dividing the actual bending moment by αD, where $D = Et^3/12(1-\nu^2)$. The dimensionless curvature is $R\theta/L$, since longitudinal curvature is approximately the same everywhere along the tape-spring and equal to θ/L. Thus, for given values of R and α, the initial behaviour of tape-springs of different lengths is given by a single straight line, whose slope is a measure of the bending stiffness of the tape-spring. As flattening of the tape-spring begins, the plots diverge accordingly.

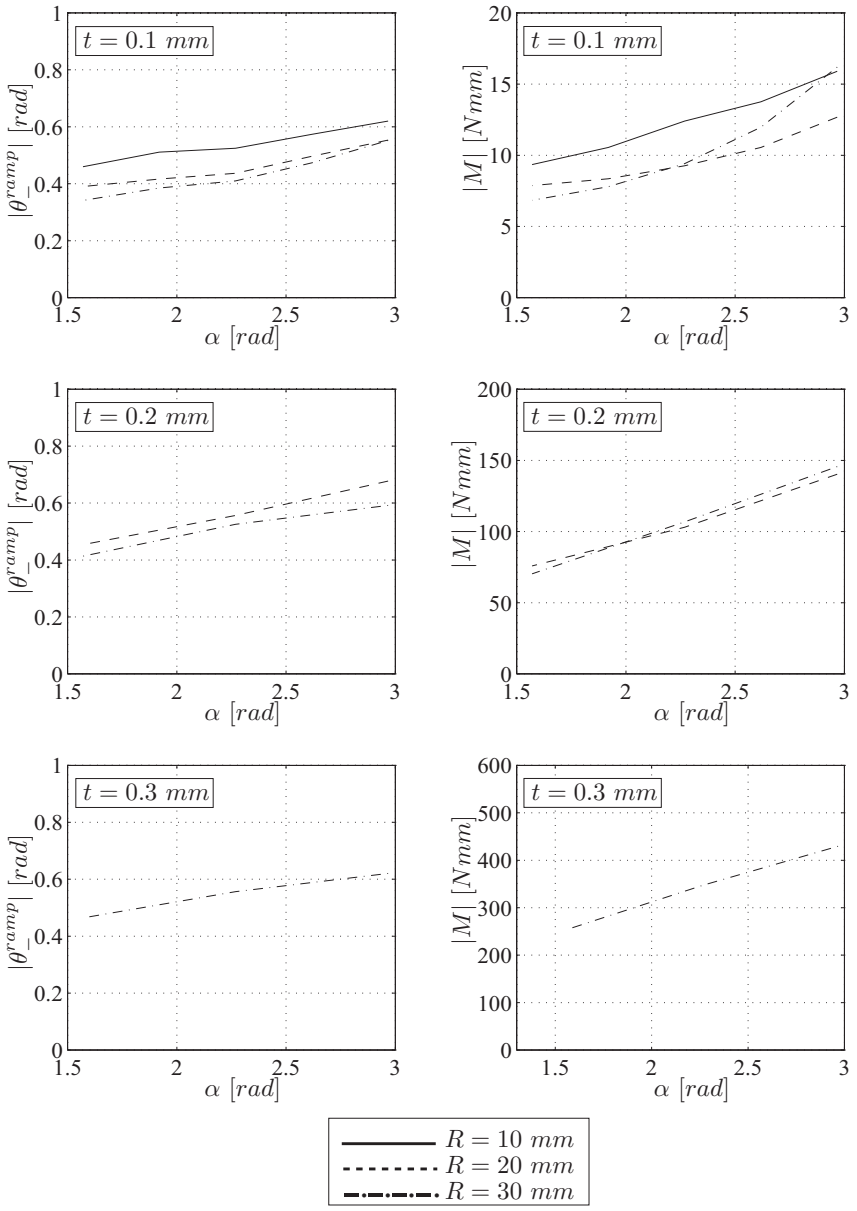

Figure 2.6: Relative end rotation and associated bending moment at the first point of zero gradient, for equal-sense bending.

2.2.2 An Example

The complete moment-rotation relationship of a tape-spring with $R = 20\ mm$, $t = 0.1\ mm$, $\alpha = 1.57\ rad$ (90°) and $L = 200\ mm$ is shown in Fig. 2.8.

A solid curve indicates the *complete* bending response obtained from ABAQUS.

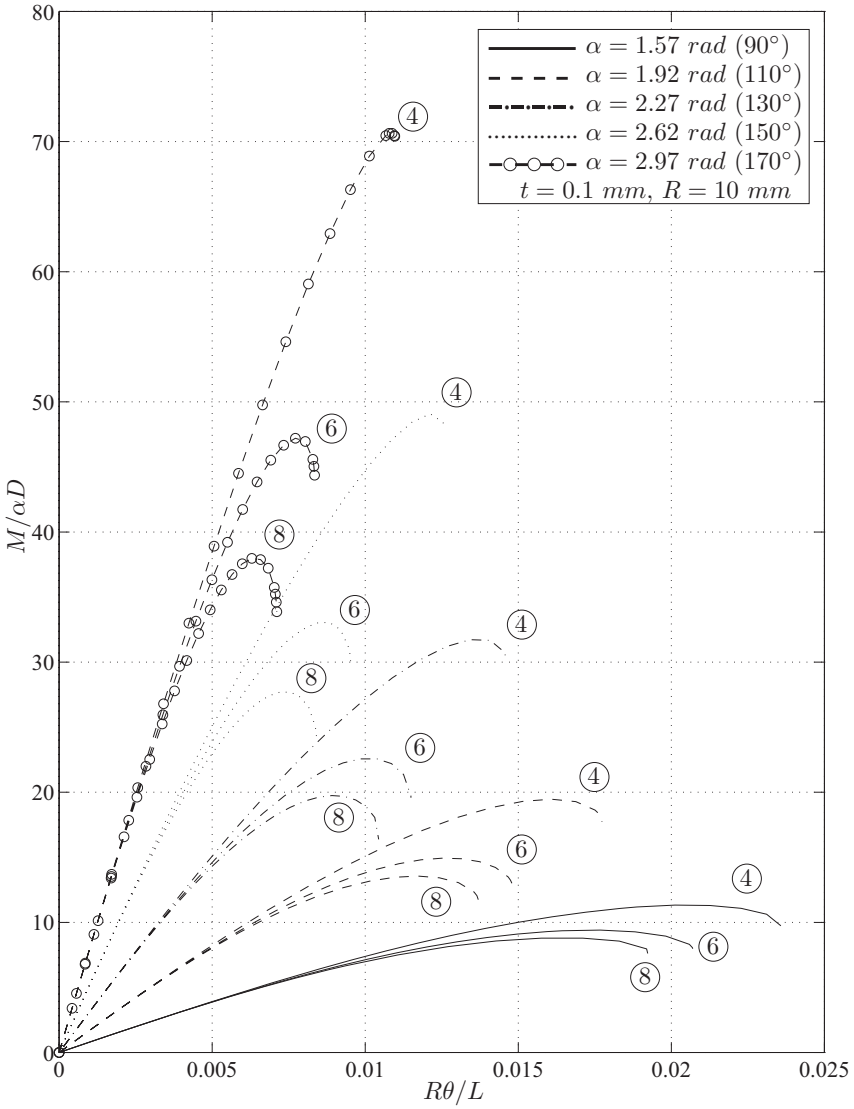

Figure 2.7: Non-dimensionalised moment-curvature behaviour for opposite-sense bending, before buckling. The numbers inside the circles refer to the length of each tape-spring $\times R\alpha$.

The bending response from the heel onwards for a tape-spring of the same cross-section, but length $8R\alpha$ ($\approx 251\ mm$) is denoted by "o". It is clearly obvious, that there is practically no difference with the curve for $L = 200\ mm$.

For equal-sense bending, the response of a tape-spring of length $4R\alpha$ ($\approx 126\ mm$) is shown by "$*$" after the point of zero gradient. Note that there is no difference between these points and the solid curve. The curve represented by "+" was also constructed from the moment-rotation relationship of a tape-spring

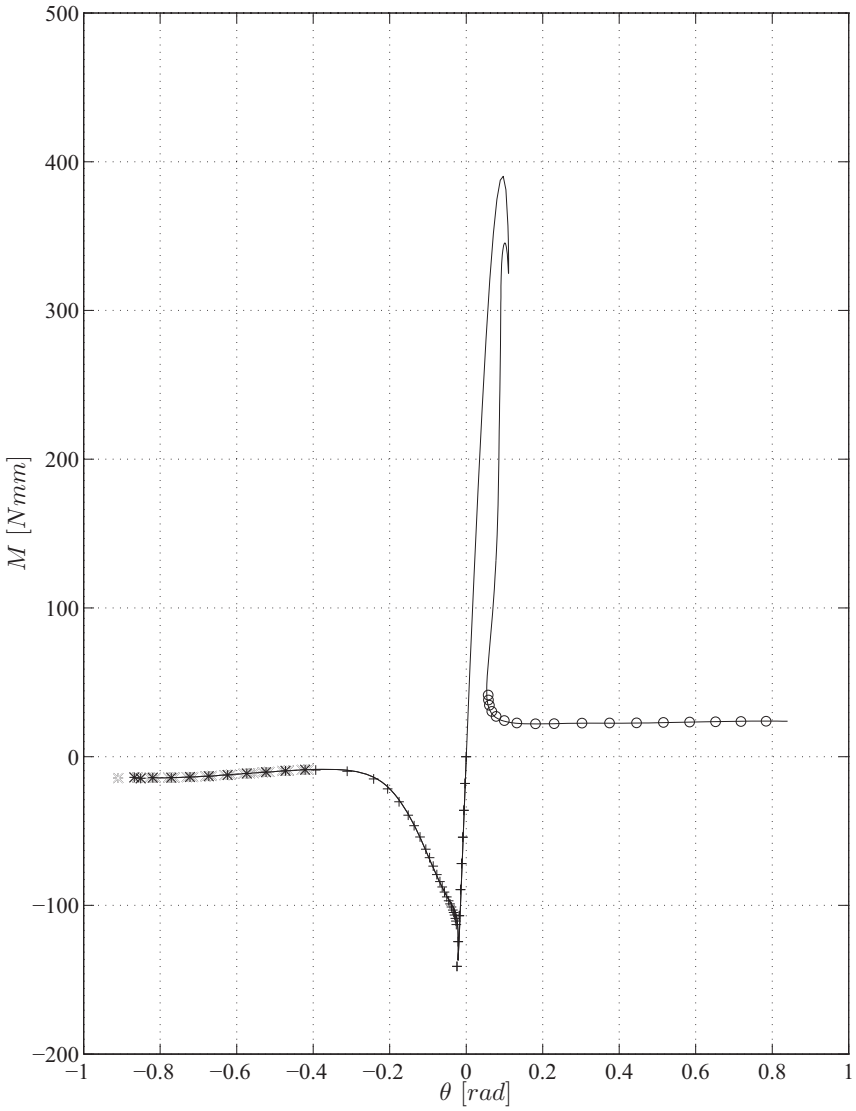

Figure 2.8: Comparison of moment-rotation relationships for tape-spring with $R = 20\ mm$, $t = 0.1\ mm$, $L = 200\ mm$ and $\alpha = 90°$, and other lengths of tape-springs.

of length $4R\alpha$. Again, this curve is practically identical to the underlying solid curve of the longer tape-spring.

2.3 Key Parameters

The key parameters that characterise the bending of finite-length tape-springs will be expressed in terms of their geometry and material properties. This will

provide the basis for the derivation of an *idealised* moment-rotation relationship, *c.f.* Fig. 1.3, without the need for a finite-element analysis. Moreover, useful insight will be gained for the design of composite hinges detailed in Chapter 6.

From Section 2.2, the seven key parameters to be examined are: M_+^{max}, θ_+^{max}, the "heel" rotation for opposite-sense bending *i.e.* θ_+^{heel}, M_-^{max}, the rotation at which the gradient first becomes zero after local buckling for equal-sense bending *i.e.* θ_-^{ramp}, and finally M_+^* and M_-^*.

2.3.1 Expression for M_+^{max}

Figure 2.9 shows several plots of $\log(M_+^{max})$ *vs* $\log(\alpha)$ obtained from finite-element analyses for opposite-sense bending. Within each sub-figure, the values of R and t are fixed, and points marked with the same symbol are for springs with a particular value of $L/(R\alpha)$. Clearly, these points lie on straight lines for each value of $L/(R\alpha)$, which indicates that the corresponding relationship is a power law relationship of the type

$$M_+^{max} = A\alpha^m \tag{2.2}$$

where A is a function of D, R, t and $L/(R\alpha)$, but not explicitly of α, and m is the slope of each line. From dimensional analysis, m can only be a function of R, t and $L/(R\alpha)$, and A must be a linear function of D. Rewriting Eq. 2.2 gives

$$\frac{M_+^{max}}{D} = A'\alpha^m \tag{2.3}$$

and A' is a function only of R, t and $L/(R\alpha)$, and is dimensionless. The values of A' and m are given in Table 2.4. Note that for $R/t = 100$, the corresponding values of A' for equal values of $L/(R\alpha)$ but different values of R, are practically identical. The same is also true for m. This suggests that the table can be condensed down by considering the variation of A' and m with the dimensionless group R/t for each value of $L/(R\alpha)$, see Table 2.5.

Calladine (1983) has shown that the moment-rotation relationship of a finite-length cylindrical tube with rigidly encased ends can be expressed by two separate power laws in R/t, relating to bending and membrane action, respectively. This suggests that a similar relationship may be valid for tape-springs but, because Calladine's analysis is not directly applicable to the present problem, it might be expected that the number of terms might be greater than two. Therefore, it can be written

$$A' = a_1\left(\frac{R}{t}\right)^{b_1} + a_2\left(\frac{R}{t}\right)^{b_2} + \cdots + a_s\left(\frac{R}{t}\right)^{b_s} \tag{2.4}$$

where s is the total number of terms, and b_1 to b_s are constants. The terms a_1 to a_s are functions of l only, where

$$l = \frac{L}{R\alpha} \tag{2.5}$$

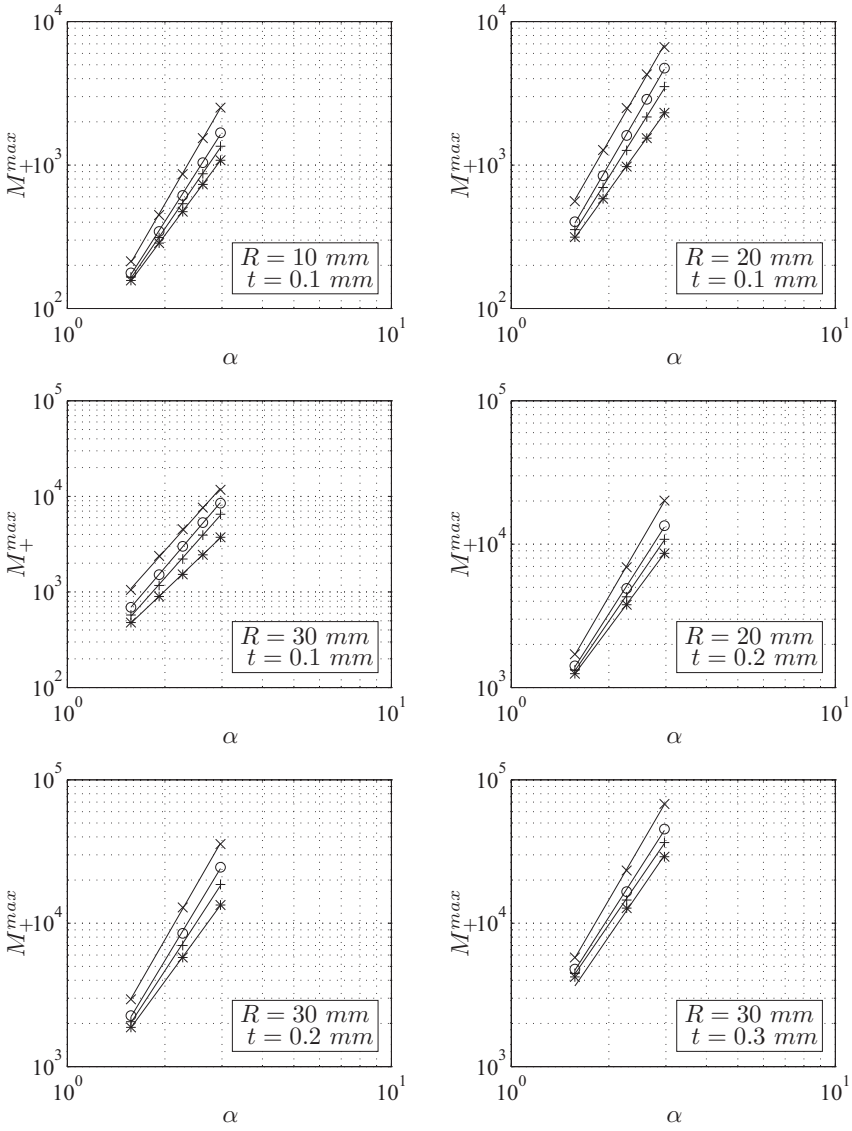

Figure 2.9: Log-log plots of M_+^{max} against α for all tape-spring geometries analysed using ABAQUS. ABAQUS results are plotted as follows: "$\times$", $L = 4R\alpha$; "$\circ$", $L = 6R\alpha$; "$+$", $L = 8R\alpha$; "$*$", $L = 16R\alpha$. Straight line fits through ABAQUS data shown by solid lines.

The determination of a_1, b_1, ..., a_s, b_s, as well as the optimal value of s is analogous to a problem in dynamic identification discussed by Tan and Pellegrino (1996). For each value of l, the four values of R/t, *i.e.* 100, 150, 200, and 300, are substituted separately into Eq. 2.4, along with the corresponding value of A', to give four linear equations in the unknowns a_1 to a_s. For this system to admit a unique solution, s must be less than or equal to four. For s less than

$R\ [mm]$	$t\ [mm]$	$L/(R\alpha)$	A'	m	R/t
10	0.1	4	3.0697	3.8731	100
		6	2.9595	3.5312	
		8	3.0777	3.2947	
		16	3.3013	3.0312	
20	0.1	4	8.199	3.9059	200
		6	5.6743	3.8858	
		8	5.6456	3.6069	
		16	6.3130	3.1337	
30	0.1	4	16.3281	3.7941	300
		6	9.6318	3.9641	
		8	8.2667	3.8239	
		16	9.1744	3.2274	
20	0.2	4	3.0693	3.8737	100
		6	2.9562	3.5273	
		8	3.0870	3.2945	
		16	3.3027	3.0310	
30	0.2	4	5.2705	3.9247	150
		6	4.2950	3.7389	
		8	4.4367	3.4558	
		16	4.8300	3.0883	
30	0.3	4	3.0706	3.8734	100
		6	2.9570	3.5271	
		8	3.0863	3.2949	
		16	3.3027	3.0310	

Table 2.4: Values of A' and m in Eq. 2.3 from best fit lines in Fig. 2.9.

four, the above system of linear equations becomes largely over-determined and, following Tan and Pellegrino (1996), the singular value decomposition (SVD) of the coefficient matrix is used to obtain a solution. The accuracy of the solution is checked by means of a normalised error between the actual values of A' and the values obtained by substituting the estimated parameters a_1 to a_s back into Eq. 2.4. Thus, an accurate set of parameters is obtained when the error falls below a predetermined level as the number of terms is increased.

By a process of trial and error, the following expression produced the smallest error overall, as indicated in Table 2.6

$$A'^2 = a_1 \left(\frac{R}{t}\right)^2 + a_2 \left(\frac{R}{t}\right)^4 + \cdots + a_s \left(\frac{R}{t}\right)^{2s} \tag{2.6}$$

Note that A' is raised to the power of two.

Also note that, for $s = 4$, the error is almost zero since the system of equations

R/t	$L/R\alpha$	A'	m
100	4	3.0699	3.8734
	6	2.9576	3.5285
	8	3.0837	3.2947
	16	3.3022	3.0311
150	4	5.2705	3.9247
	6	4.2950	3.7389
	8	4.4367	3.4558
	16	4.8300	3.0883
200	4	8.1990	3.9059
	6	5.6743	3.8858
	8	5.6456	3.6069
	16	6.3130	3.1337
300	4	16.3281	3.7941
	6	9.6318	3.9641
	8	8.2667	3.8239
	16	9.1744	3.2274

Table 2.5: Condensed version of Table 2.4.

s	% error for $l = 4$	% error for $l = 6$	% error for $l = 8$	% error for $l = 16$
1	21.75	9.14	4.18	3.43
2	$8.78 \cdot 10^{-2}$	2.23	1.91	$6.16 \cdot 10^{-1}$
3	$2.38 \cdot 10^{-2}$	$4.70 \cdot 10^{-2}$	$2.20 \cdot 10^{-2}$	$1.56 \cdot 10^{-1}$
4	$4.11 \cdot 10^{-5}$	$3.59 \cdot 10^{-5}$	$4.68 \cdot 10^{-5}$	$4.05 \cdot 10^{-5}$

Table 2.6: Percentage error between calculated and actual values of A'.

is perfectly conditioned. For, $s = 2$, the maximum error is just over two percent, which shows that the bending-membrane split identified by Calladine is a perfectly acceptable approximation. Thus, Eq. 2.6 becomes

$$A' = \frac{R}{t}\left[a_1 + a_2\left(\frac{R}{t}\right)^2\right]^{\frac{1}{2}} \tag{2.7}$$

The values of a_1 and a_2, for each value of l, are indicated in Table 2.7.

Next, a_1 and a_2 will be expressed as functions of l only. Assuming that in general a polynomial expression will apply

$$a_1 = c_1 l^{d_1} + c_2 l^{d_2} + \cdots + c_s l^{d_s} \tag{2.8}$$

where c_1 to c_s are constants, and so are d_1 to d_s. A similar expression can be written for a_2. Therefore, for the four values of a_1 given in Table 2.7, a system of

	$l = 4$	$l = 6$	$l = 8$	$l = 16$
a_1	$6.546 \cdot 10^{-4}$	$6.875 \cdot 10^{-4}$	$8.692 \cdot 10^{-4}$	$1.060 \cdot 10^{-3}$
a_2	$2.564 \cdot 10^{-8}$	$3.791 \cdot 10^{-9}$	$-1.243 \cdot 10^{-9}$	$-1.394 \cdot 10^{-9}$

Table 2.7: Values of a_1 and a_2 in Eq. 2.7.

four linear equations is obtained in the unknowns c_1 to c_s. For a unique solution, the total number of terms in each equation must be less than or equal to four and, again, the SVD method used before is employed to find c_1 to c_s.

Again, by a process of trial and error, the following expressions for a_1 and a_2 were obtained

$$a_1 = 1.152 \cdot 10^{-3} - \frac{2.210 \cdot 10^{-3}}{l} \tag{2.9}$$

$$a_2 = -2.061 \cdot 10^{-9} + \frac{7.096 \cdot 10^{-6}}{l^4} \tag{2.10}$$

The inverse powers of l ensure that a_1 and a_2 have finite values when the length of the tape-spring becomes large. Equations 2.9 and 2.10 give values of a_1 and a_2 which differ from those in Table 2.7 by a maximum of 7.2% and 4.4%, respectively. The final expression for A' is given by substituting Eqs. 2.9 and 2.10 into Eq. 2.7, *i.e.*

$$\begin{aligned} A' &= \frac{R}{t}\Bigg[1.152 \cdot 10^{-3} - \frac{2.210 \cdot 10^{-3}}{l} \\ &\quad + \left(-2.061 \cdot 10^{-9} + \frac{7.096 \cdot 10^{-6}}{l^4}\right)\left(\frac{R}{t}\right)^2\Bigg]^{\frac{1}{2}} \end{aligned} \tag{2.11}$$

Using a similar procedure, an expression for m is set up as a polynomial where each R/t term is multiplied by a function of l. It is desirable that, for given values of R/t and α, the expression for m tends to a finite value, as l tends to infinity. This ensures that the value of M_+^{max} in Eq. 2.3 becomes constant as end-effects become negligible. The resulting expression is

$$\begin{aligned} m &= 2.840 + \frac{18.170}{l^2} \\ &\quad + \left[-2.281 \cdot 10^{-3} + \frac{6.809 \cdot 10^{-2}}{l} - \frac{0.245}{l^2}\right]\frac{R}{t} \end{aligned} \tag{2.12}$$

Equations 2.11 and 2.12 are now substituted into Eq. 2.3 to give a complete expression for M_+^{max}, in Nmm. Values from this expression have been plotted in Fig. 2.10 against α for $R = 10\ mm$, $t = \ 0.1\ mm$, and each of the indicated spring lengths. As can be clearly seen, the error between the actual values of M_+^{max} and the computed values is very small indeed, and is typical for all of the springs analysed.

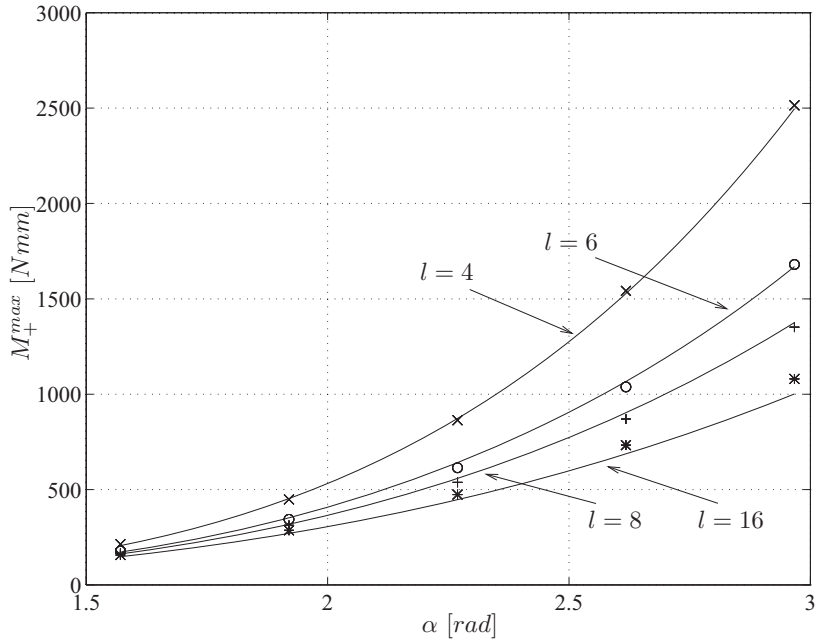

Figure 2.10: Comparison of M_+^{max} from ABAQUS: "$\times$", $l = 4$; "$\circ$", $l = 6$; "$+$", $l = 8$; "$*$", $l = 16$, and analytical predictions from Eq. 2.3 after back substitution of Eqs. 2.11 and 2.12. Section parameters are $R = 10\ mm$ and $t = 0.1\ mm$.

2.3.2 Expression for θ_+^{max}

The same procedure outlined in the previous section will now be used to obtain an expression for θ_+^{max}.

Consider Fig. 2.11, where each sub-figure contains plots of $\log(R\theta_+^{max}/L)$ against $\log(\alpha)$, for a given R and t, and indicated spring length. Because the ABAQUS results lie on virtually straight lines, it may be written

$$R\theta_+^{max}/L = B\alpha^n \tag{2.13}$$

where B and n are dimensionless functions of R/t (Calladine 1983) and l. Table 2.8 indicates the variation in B and n with l for each value of R/t. Note again that for $R/t = 100$, the corresponding values of B and n, respectively, for equal values of l, but for different values of R were the same in Fig. 2.11.

In analogy with the previous section

$$B = e_1 \left(\frac{R}{t}\right)^{f_1} + e_2 \left(\frac{R}{t}\right)^{f_2} + \cdots + e_s \left(\frac{R}{t}\right)^{f_s} \tag{2.14}$$

where e_1 to e_s are functions of l only, f_1 to f_s are constant values and s is, again, the total number of terms in the polynomial. The SVD technique was then applied

in a two-stage process. First, for an arbitrary choice of f_1 to f_s, values of e_1 to e_s were computed for each value of l. Equation 2.14 was reduced to a simpler form which gives accurate values of B. Second, e_1 to e_s were found as functions of l. The final expression for B is

$$\begin{aligned} B &= \left[1.520 \cdot 10^{-4} - \frac{4.365 \cdot 10^{-3}}{l} + \frac{1.993 \cdot 10^{-2}}{l^2}\right. \\ &\quad \left. + \left(13.45 - \frac{564.5}{l^4} + \frac{9.929 \cdot 10^5}{l^8}\right]\right)\left(\frac{t}{R}\right)^2\Bigg]^{\frac{1}{2}} \end{aligned} \tag{2.15}$$

By the same process, the expression for n is given by

$$\begin{aligned} n &= -2.860 + \frac{26.69}{l} - \frac{81.49}{l^2} \\ &\quad + \left[-\frac{1.071 \cdot 10^4}{l^2} + \frac{4.134 \cdot 10^5}{l^4} - \frac{3.740 \cdot 10^6}{l^6}\right]\frac{t}{R} \end{aligned} \tag{2.16}$$

Substituting Eqs. 2.15 and 2.16 back into Eq. 2.13 yields an expression for θ_+^{max}, in radians. Values of θ_+^{max} from this expression are plotted in Fig. 2.12, along with values from the ABAQUS analyses. The comparison between computed and actual values is reasonably good.

R/t	l	B	n
100	4	$3.0863{\cdot}10^{-2}$	-0.9786
	6	$3.0928{\cdot}10^{-2}$	-1.3064
	8	$3.4083{\cdot}10^{-2}$	-1.5827
	16	$3.5701{\cdot}10^{-2}$	-1.7754
150	4	$2.4518{\cdot}10^{-2}$	-0.9977
	6	$1.9716{\cdot}10^{-2}$	-1.0901
	8	$2.0936{\cdot}10^{-2}$	-1.3976
	16	$2.4249{\cdot}10^{-2}$	-1.7888
200	4	$2.2758{\cdot}10^{-2}$	-1.1255
	6	$1.3927{\cdot}10^{-2}$	-0.9199
	8	$1.3559{\cdot}10^{-2}$	-1.1254
	16	$1.5250{\cdot}10^{-2}$	-1.5936
300	4	$1.8325{\cdot}10^{-2}$	-1.1854
	6	$1.1276{\cdot}10^{-2}$	-0.9668
	8	$9.8182{\cdot}10^{-3}$	-1.0390
	16	$1.1266{\cdot}10^{-2}$	-1.6236

Table 2.8: Values of B and n in Eq. 2.13 from best fit lines in Fig. 2.11.

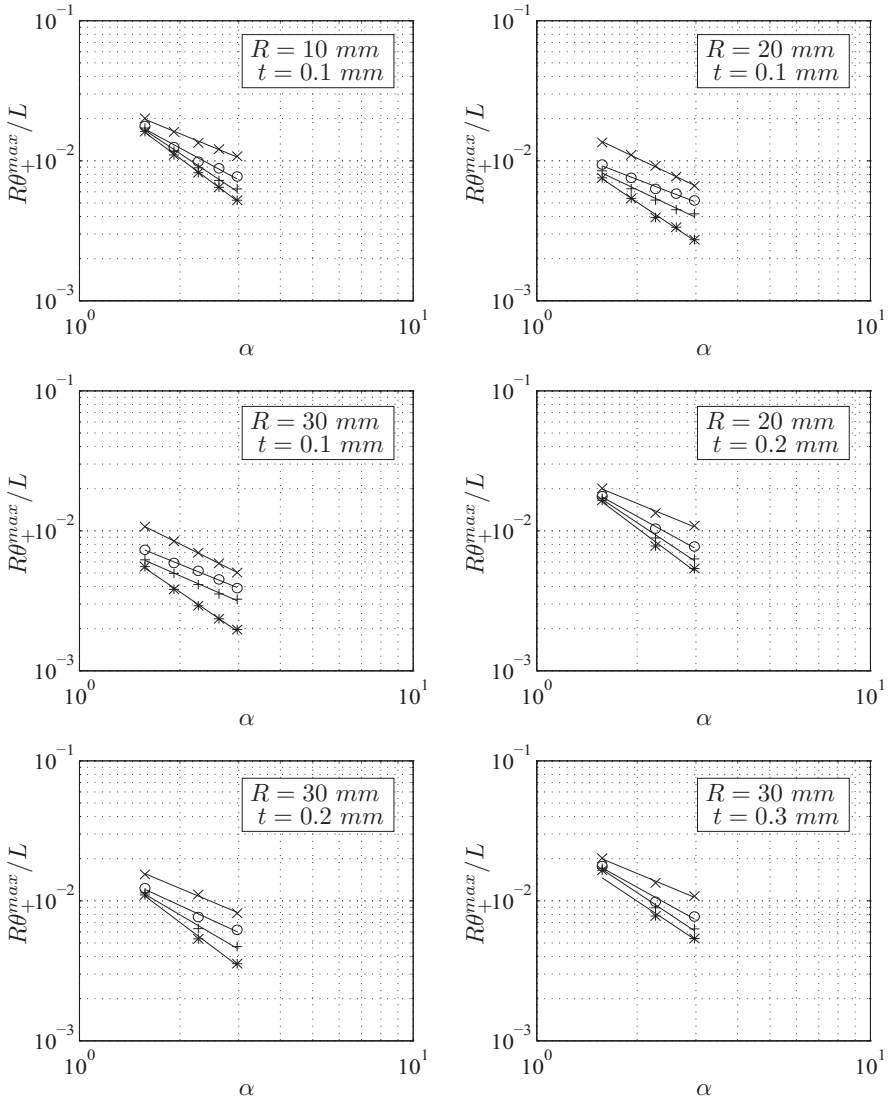

Figure 2.11: Log-log plots of $R\theta_+^{max}/L$ against α for all tape-spring geometries analysed using ABAQUS. ABAQUS results plotted as follows: "$\times$", $L = 4R\alpha$; "$\circ$", $L = 6R\alpha$; "$+$", $L = 8R\alpha$; "$*$", $L = 16R\alpha$. Straight line fits through ABAQUS data shown by solid lines.

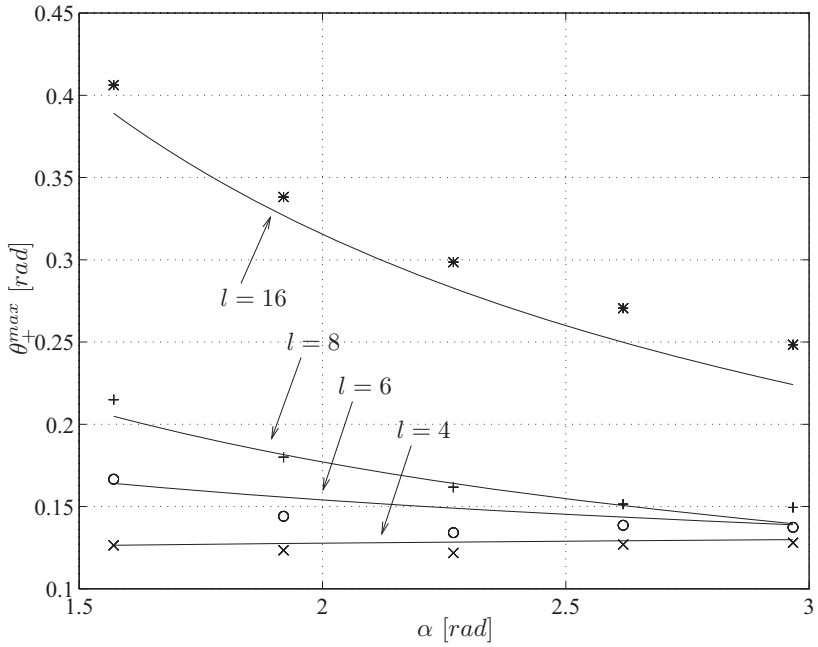

Figure 2.12: Comparison of θ_+^{max} from ABAQUS:"$\times$", $l = 4$; "$\circ$", $l = 6$; "$+$", $l = 8$; "$*$", $l = 16$, and values computed from Eq. 2.13 after back substitution of Eqs. 2.15 and 2.16.

2.3.3 Expression for θ_+^{heel}

An expression θ_+^{heel} will now be derived. From Section 2.2, θ_+^{heel} is assumed to be independent of L and, as already for θ_+^{max}, R/t is the only relevant dimensionless group. Hence

$$\theta_+^{heel} = g_1 \left(\frac{R}{t}\right)^{h_1} + g_2 \left(\frac{R}{t}\right)^{h_2} + \cdots + g_s \left(\frac{R}{t}\right)^{h_s} \tag{2.17}$$

Here, g_1 to g_s are functions of α, s is the total number of terms and h_1 to h_s are constants. For each value of α in Fig. 2.4, a system of linear equations in the unknowns g_1 to g_s is obtained by substitution of the appropriate values of θ_+^{heel} and R/t. This system is solved using SVD, and the values of h_1 to h_s are varied to minimise the error for the smallest possible s. Thus, Eq. 2.17 was reduced to

$$\theta_+^{heel} = g_1 + g_2 \left(\frac{R}{t}\right)^{-1} \tag{2.18}$$

The values of g_1 and g_2 are given in Table 2.9. Typically

$$g_1 = j_1\alpha^{k_1} + j_2\alpha^{k_2} + \cdots + j_s\alpha^{k_s} \tag{2.19}$$

Again, each of the subscripted terms on the right-hand side is a constant, and the powers k_1 to k_s are chosen arbitrarily. The SVD technique is applied to solve for the unknowns j_1 to j_s, for each value of g_1. The expression which gives the best error performance is

$$g_1 = 3.673 \cdot 10^{-2}\alpha - 4.932 \cdot 10^{-2}\alpha^2 + 1.080 \cdot 10^{-2}\alpha^3 \tag{2.20}$$

Similarly, for g_2, the following, rather neat expression was found

$$g_2 = e^{\pi}\alpha^{-0.80} \tag{2.21}$$

	$\alpha = 90°$	$\alpha = 110°$	$\alpha = 130°$	$\alpha = 150°$	$\alpha = 170°$
g_1	-2.275 $\times 10^{-2}$	-3.282 $\times 10^{-2}$	-4.673 $\times 10^{-2}$	-4.669 $\times 10^{-2}$	-4.324 $\times 10^{-2}$
g_2	16.14	13.73	13.38	10.63	9.68

Table 2.9: Values of g_1 and g_2 in Eq. 2.18.

The complete expression for θ_+^{heel}, in *rad*, is obtained by substituting Eqs. 2.20 and 2.21 into Eq. 2.18

$$\theta_+^{heel} = \frac{3.673}{10^2}\alpha - \frac{4.932}{10^2}\alpha^2 + \frac{1.080}{10^2}\alpha^3 + \frac{t}{R}e^{\pi}\alpha^{-0.80} \tag{2.22}$$

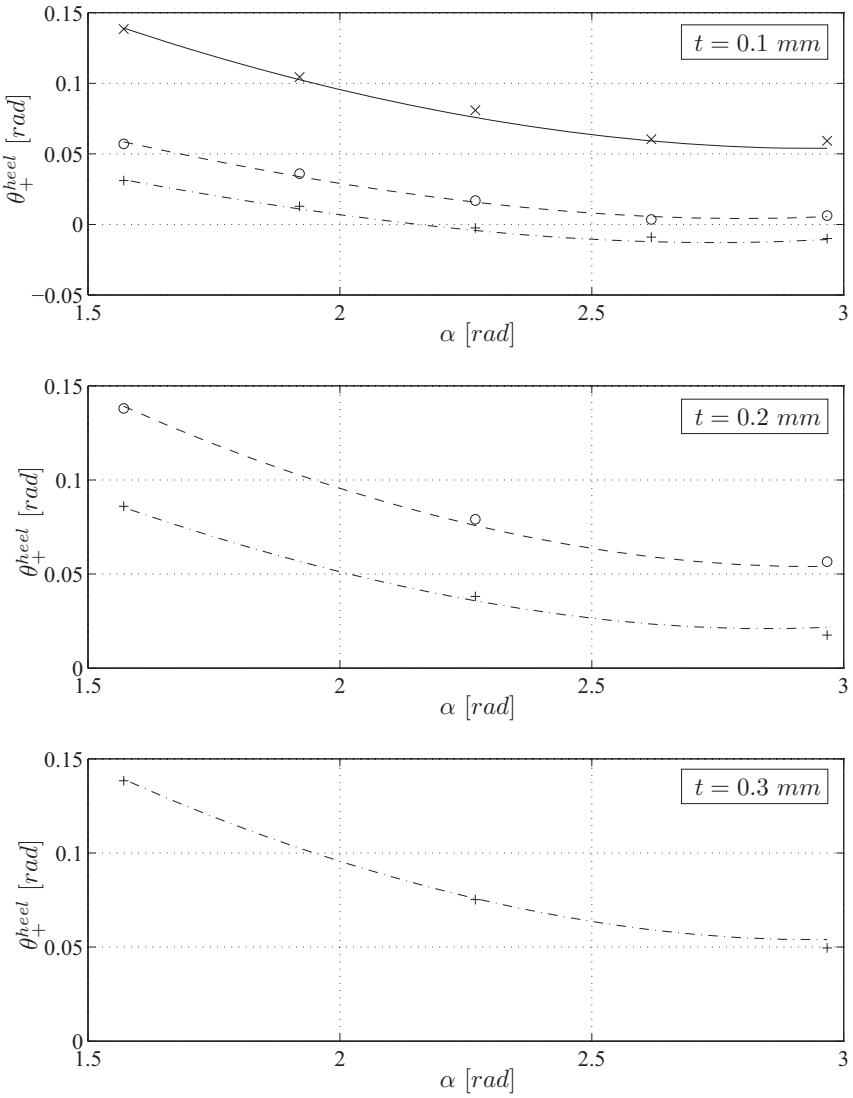

Figure 2.13: Comparison of θ_+^{heel} from ABAQUS (symbols) and values computed from Eq. 2.22 (continuous lines). Solid line and "×", $R = 10\ mm$; dashed lines and "○", $R = 20\ mm$; dot-dashed lines and "+", $R = 30\ mm$.

Predictions from Eq. 2.22 are compared with the values of θ_+^{heel} from ABAQUS in Fig. 2.13.

Note that the above result is similar to that for determining expressions for M_+^{max} and θ_+^{max}, despite there being one less dimensionless group.

2.3.4 Expression for M_-^{max}

Figure 2.14 contains plots of $\log(|M_-^{max}|/D)$ against $\log(\alpha)$ for all finite-element analyses. Points shown by the same symbol correspond to a fixed value of R/t and lie on a straight line, as shown. Therefore

$$\frac{|M_-^{max}|}{D} = C\alpha^p \tag{2.23}$$

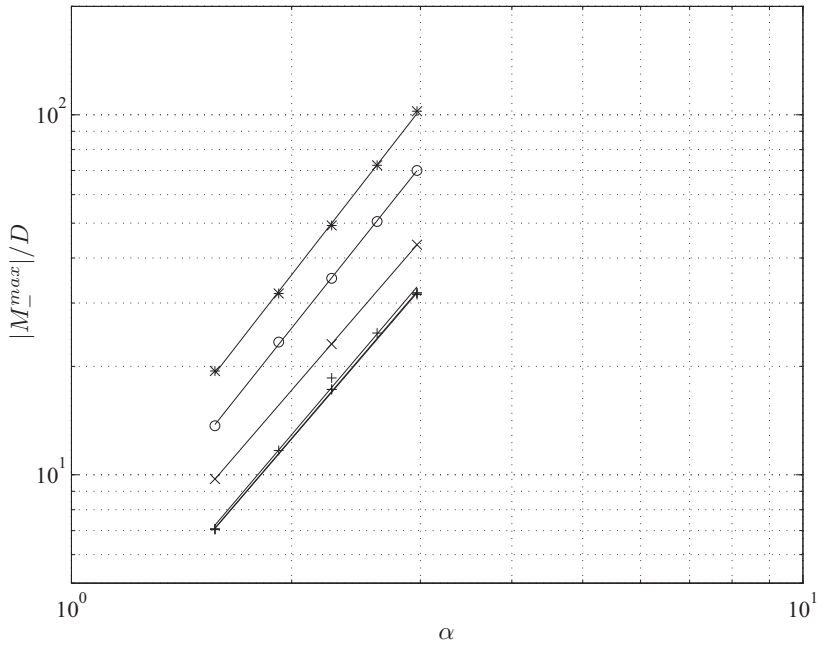

Figure 2.14: Log-log plots of $|M_-^{max}|/D$ *vs* α for all ABAQUS results: "+", $R/t = 100$; "×", $R/t = 150$; "○", $R/t = 200$; "∗", $R/t = 300$. Solid lines are straight line fits of ABAQUS results.

M_-^{max} does not depend on the length of the tape-spring and, therefore, C and p are functions of R/t only. Using the SVD technique described previously

$$C = 2.600 \cdot 10^{-2}\frac{R}{t} - 2.143 \cdot 10^{-5}\left(\frac{R}{t}\right)^2 \tag{2.24}$$

$$p = 2.224 + 1.338 \cdot 10^{-3}\frac{R}{t} \tag{2.25}$$

Substituting Eqs. 2.24 and 2.25 into Eq. 2.23 and rearranging gives $|M_-^{max}|$ in Nmm

$$|M_-^{max}| = D\left[\frac{2.600}{10^2}\frac{R}{t} - \frac{2.143}{10^5}\left(\frac{R}{t}\right)^2\right]\alpha^{\left[2.224+\frac{1.338}{10^3}\frac{R}{t}\right]} \tag{2.26}$$

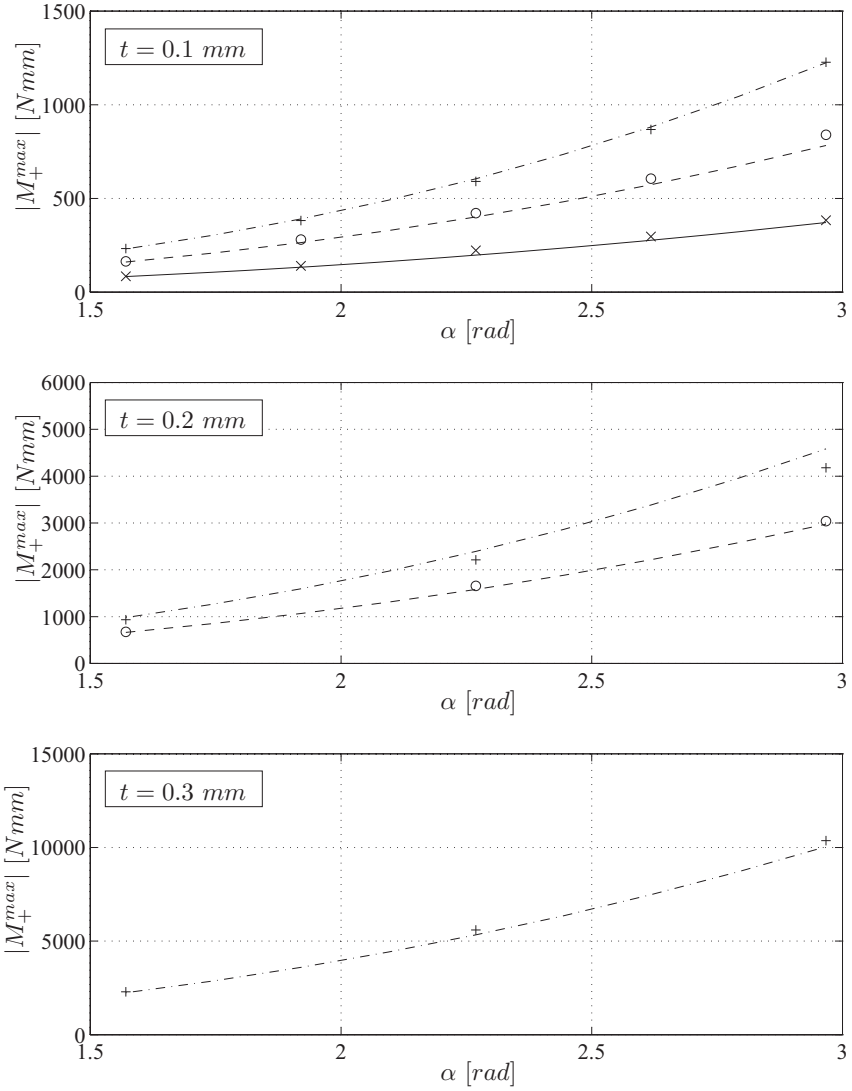

Figure 2.15: Comparison of $|M_+^{max}|$ from ABAQUS (symbols) and values computed from Eq. 2.22 (continuous lines). Solid line and "×", $R = 10\ mm$; dashed lines and "○", $R = 20\ mm$; dot-dashed lines and "+", $R = 30\ mm$.

Figure 2.15 compares predictions from Eq. 2.26 with all finite-element predictions — the difference between corresponding curves is very small.

2.3.5 Expression for θ_-^{ramp}

An expression for the relative end rotation at which the gradient first becomes zero after M_-^{max} will now be derived.

Consider the plots in Fig. 2.6. The variation of $|\theta_-^{ramp}|$ with α, for each value of

R/t, is a little irregular as the resolution of the finite-element results is insufficient to define accurately these local stationary points. Nonetheless, each curve is well represented by a straight line, whose equation is

$$|\theta_{-}^{ramp}| = F\alpha + G \tag{2.27}$$

where F is the average slope for all curves and is equal to $0.1293 \approx 1/8$. The intercepts are found to be approximately related to t/R in a linear fashion. The constant of linearity is $17.992 \approx 18$. Thus, Eq. 2.27 becomes

$$|\theta_{-}^{ramp}| = \frac{\alpha}{8} + 18\frac{t}{R} \tag{2.28}$$

2.3.6 Expressions for M_{+}^{*} and M_{-}^{*}

In Section 1.2.1 it was noticed that the longitudinal radius of curvature in the fold region is approximately equal to the transverse radius of curvature R of the undeformed tape-spring. Also, the transverse radius of curvature in the fold is approximately zero, *i.e.* the fold region is approximately cylindrical. Since both surfaces are cylindrical, there is no change in Gaussian curvature, and hence the stretching energy in the shell is zero. Hence, by minimising the bending strain energy in the fold it can be shown that both the original, undeformed surface and the deformed surface have the same radius of curvature R (Wüst 1954, Rimrott 1970, Calladine 1988).

If the changes of curvature associated with the fold in the longitudinal and transverse directions are κ_l and κ_t, respectively, then, from Calladine (1983), the corresponding bending moment is given by

$$M^* = DR\alpha(\kappa_l + \nu\kappa_t) \tag{2.29}$$

For opposite-sense bending $\kappa_t = 1/R$ and $\kappa_l = 1/R$. Substituting these values into Eq. 2.29 yields

$$M_{+}^{*} = (1+\nu)D\alpha \tag{2.30}$$

For equal-sense bending κ_t is also $1/R$, but $\kappa_l = -1/R$. Thus, the expression analogous to Eq. 2.38 is

$$M_{-}^{*} = -(1-\nu)D\alpha \tag{2.31}$$

Expressions equivalent to Eqs. 2.30 and 2.31 can be obtained also by integration of the "stowage stress" for a STEM tube, obtained by Rimrott (1966*a*).

2.3.7 Summary of Key Features

Expressions have now been determined for all key parameters listed at the start of this section and are listed below:

$$M_+^{max} = D\frac{R}{t}\left[\frac{1.152}{10^3} - \frac{2.210}{10^3 l} + \left(\frac{-2.061}{10^9} + \frac{7.096}{10^6 l^4}\right)\left(\frac{R}{t}\right)^2\right]^{\frac{1}{2}} \alpha^{\left[2.840+\frac{18.17}{l^2}+\left(\frac{-2.281}{10^3}+\frac{6.809}{10^2 l}-\frac{0.245}{l^2}\right)\frac{R}{t}\right]} \quad (2.32)$$

$$\theta_+^{max} = \frac{L}{R}\left[\frac{1.520}{10^4} - \frac{4.365}{10^3 l} + \frac{1.993}{10^2 l^2} + \left(13.45 - \frac{564.5}{l^4} + \frac{9.929}{10^5 l^8}\right)\left(\frac{t}{R}\right)^2\right]^{\frac{1}{2}} \alpha^{\left[-2.860+\frac{26.69}{l}-\frac{81.49}{l^2}+\left(\frac{-1.071}{10^{-4} l^2}+\frac{4.134}{10^{-5} l^4}-\frac{3.740}{10^{-6} l^6}\right)\frac{t}{R}\right]} \quad (2.33)$$

$$\theta_+^{heel} = \frac{3.673}{10^2}\alpha - \frac{4.932}{10^2}\alpha^2 + \frac{1.080}{10^2}\alpha^3 + \frac{t}{R}e^{\pi}\alpha^{-0.80} \quad (2.34)$$

$$|M_-^{max}| = D\left[\frac{2.600}{10^2}\frac{R}{t} - \frac{2.143}{10^5}\left(\frac{R}{t}\right)^2\right]\alpha^{\left[2.224+\frac{1.338}{10^3}\frac{R}{t}\right]} \quad (2.35)$$

$$|\theta_-^{ramp}| = \frac{\alpha}{8} + 18\frac{t}{R} \quad (2.36)$$

$$M_+^* = (1+\nu)D\alpha \quad (2.37)$$

$$M_-^* = -(1-\nu)D\alpha \quad (2.38)$$

Chapter 3

Deployment Implications

This chapter illustrates the potential of tape-springs, acting as short hinges, to deploy and then hold in position an attached *rigid element*. In practice, this would be a way of replacing a complete deployment system, without the need for additional latching mechanisms, to provide a relatively stiff interface between the deployed element and the base of the tape-springs, which could be attached directly to the spacecraft. Section 3.1 introduces the key problems associated with the deployment of a rigid element by a singly-folded tape-spring. In Section 3.2 a composite hinge, comprising identical tape-springs mounted alongside, with their convex sides alternately up and down, is shown to behave symmetrically under positive and negative bending moments.

3.1 Introduction

The free deployment of a rigid element connected to one end of a rigidly mounted tape-spring is governed by the energy stored in the tape-spring and the direction in which the tape-spring has been initially folded. Figure 3.1(a) shows the relationship between the moment applied to the rigid element and the rotation θ of the this element relative to the base of the tape. The shape of this relationship is similar to that of Fig. 1.3, but for the purposes of the following discussion, equal-sense bending moment and rotation have been plotted as positive and opposite-sense bending moment and rotation have been plotted as negative.

The spring has been initially folded in the direction of equal-sense bending to θ_0, and the amount of strain energy available for free deployment is given by the shaded area under the graph. The rigid element deploys by a release of this stored energy, whilst the relative end rotation decreases. It is assumed that, first, the mass of the tape-spring can be neglected in comparison with the mass of the rigid element; second, that end-effects prevent any appreciable motion of the fold along the tape-spring; and third that the gravitational potential energy of the rigid element does not change during deployment.

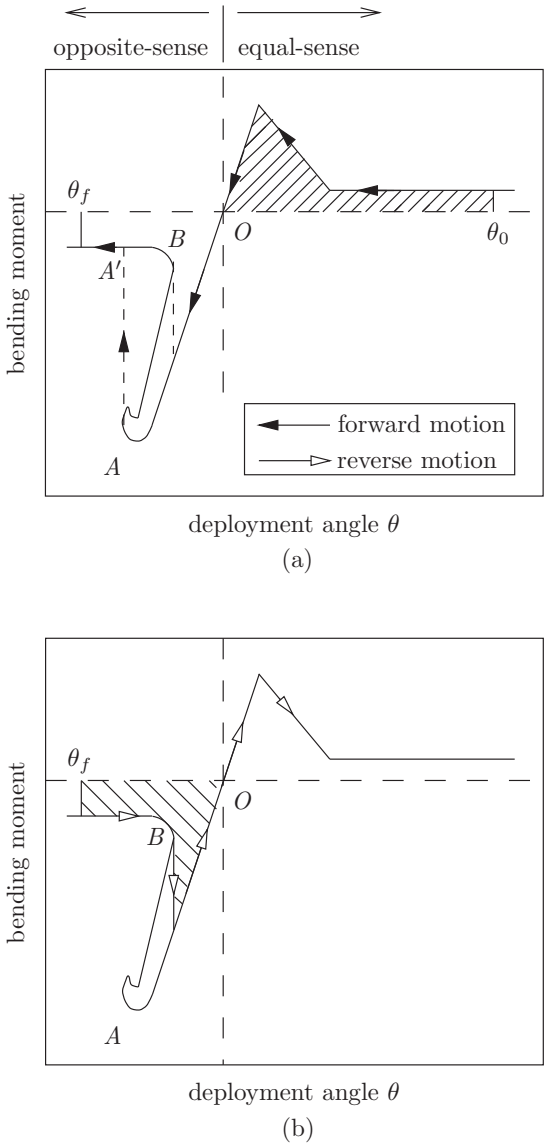

Figure 3.1: Moment applied by tape-spring to a rigid element connected to its free end. (a) The initial fold angle is θ_0 and the maximum opposite-sense rotation is θ_f. (b) Behaviour during reverse motion.

When the tape-spring becomes straight, the strain energy stored in the system is zero and, assuming that no energy has been dissipated, the kinetic energy of the system will be equal to the initial area under the graph. The rigid element then begins to slow down as kinetic energy converts back to strain energy under opposite-sense bending. If the area under the peak portion of the opposite-sense bending curve is smaller than the strain energy initially stored in the spring, the tape-spring will snap-through. Then the moment applied to the rigid element

jumps from the value at the nose, point A, to the steady-state value at the same relative end rotation, at A'. This behaviour will be referred to as *overshoot*. The rigid element continues to slow down until all the kinetic energy has been converted into strain energy for opposite-sense bending in the fold at a rotation of θ_f; the end then begins to rotate in the opposite direction. The moment applied by the tape-spring to the rigid element now follows the steady-state curve until the *heel* at point B. Thereafter, the fold snaps-back to the pre-buckled state and a higher bending moment. This bending moment, however, is lower than the peak moment at A and thus, the strain energy stored in the system is now smaller than the initial value, as shown in Fig. 3.1(b). Therefore, an angle smaller than θ_0 is attained when the rigid element stops again during equal-sense bending. This cycle continues until the system has dissipated enough energy to avoid overshooting and, from this point onwards, the motion of the system is a small-amplitude, lightly damped oscillation about the equilibrium state.

To avoid overshoot the kinetic energy of the rigid element as it passes through the origin must be smaller than the area under the steep part of the graph, OA, of the moment-rotation plot.

The features of the moment-rotation plot that are central to the deployment behaviour described above are: the initial bending stiffness; the behaviour in the region of the peak moments; the *steady state*, *i.e.* constant bending moment values; and the heel on the opposite-sense bending curve.

3.2 Moment-Rotation Relationship for a Composite Hinge

Two identical tape-springs that are mounted in parallel and with their centres of curvature on opposite sides are shown in Fig. 3.2. This arrangement is known as a *composite hinge*. Note that the principal axes of bending at each end coincide with the centre lines of the blocks. Unlike tape-springs mounted with their curvatures in the same direction, this arrangement of tape-springs will produce a hinge with *equal* positive and negative locking moments, as will now be discussed.

The moment applied by a composite hinge to a rigid element can be obtained from the moment-rotation relationship of its components, and is constructed by adding together the values of bending moment of each tape-spring for each value of θ, as shown in Fig. 3.3. In this figure, each tape-spring has $R = 10\ mm$, $L = 100\ mm$, $t = 0.1\ mm$ and $\alpha = 110°$; the moment-rotation relationship of a single tape-spring with this geometry is shown in Fig. 3.4.

Consider the behaviour of a composite hinge that is initially folded to an angle $\theta_0 > 0$. During deployment, Fig. 3.3(a), both tape-springs *unload*, *i.e.* the amount of stored strain energy decreases as the rigid element acquires kinetic energy. Again, it is assumed that the gravitational potential energy of the panel does not

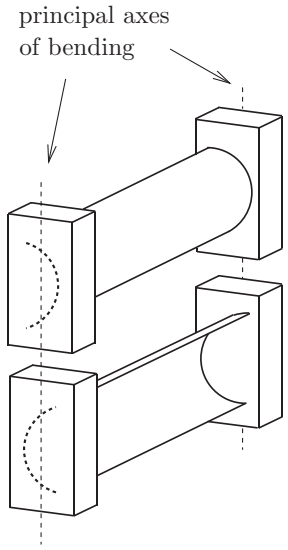

Figure 3.2: Composite tape-spring hinge in the straight configuration.

change during deployment. As the rotation angle becomes approximately zero, tape-spring 2, initially folded in the opposite sense, snaps-back whilst tape-spring 1 gradually straightens out as the moment increases and then decreases. The kinetic energy of the rigid element reaches a maximum when both tape-springs are completely straight, and is equal to the area from θ_0 under the solid line to the origin O, Fig. 3.3(b). At this point, both tape-springs bend in the opposite direction, *i.e.* $\theta < 0$, and store strain energy thus *absorbing* the kinetic energy of the rigid element. The rigid element stops when all the kinetic energy has been converted into potential energy, *i.e.* at an angle such that the area above the curve in Fig. 3.3(b) is equal to the energy initially stored in the composite hinge. Tape-spring 1 will snap through if the amount of energy to be absorbed to completely arrest the rigid element is greater than the area above the curve from O to point B. Therefore, the condition for avoiding overshoot is that the initial energy stored in the folded tape-springs is less than or equal to the energy that can be absorbed without one tape-spring snapping in the opposite-sense direction. In other words, the difference between these two energies needs to be considered in order to decide if the system will overshoot.

The difference between the energy released and absorbed during deployment from an initial angle θ_0 is indicated by the shaded areas, respectively area 1 and area 2, in Fig. 3.3(c). The maximum initial angle of folding that avoids overshoot, θ_0^{max}, has area 1 equal to area 2. *It can be shown that this result is independent of the inertia properties of the rigid element and of the number of pairs of tape-springs.*

After the rigid element has locked out without overshooting, the tape-springs

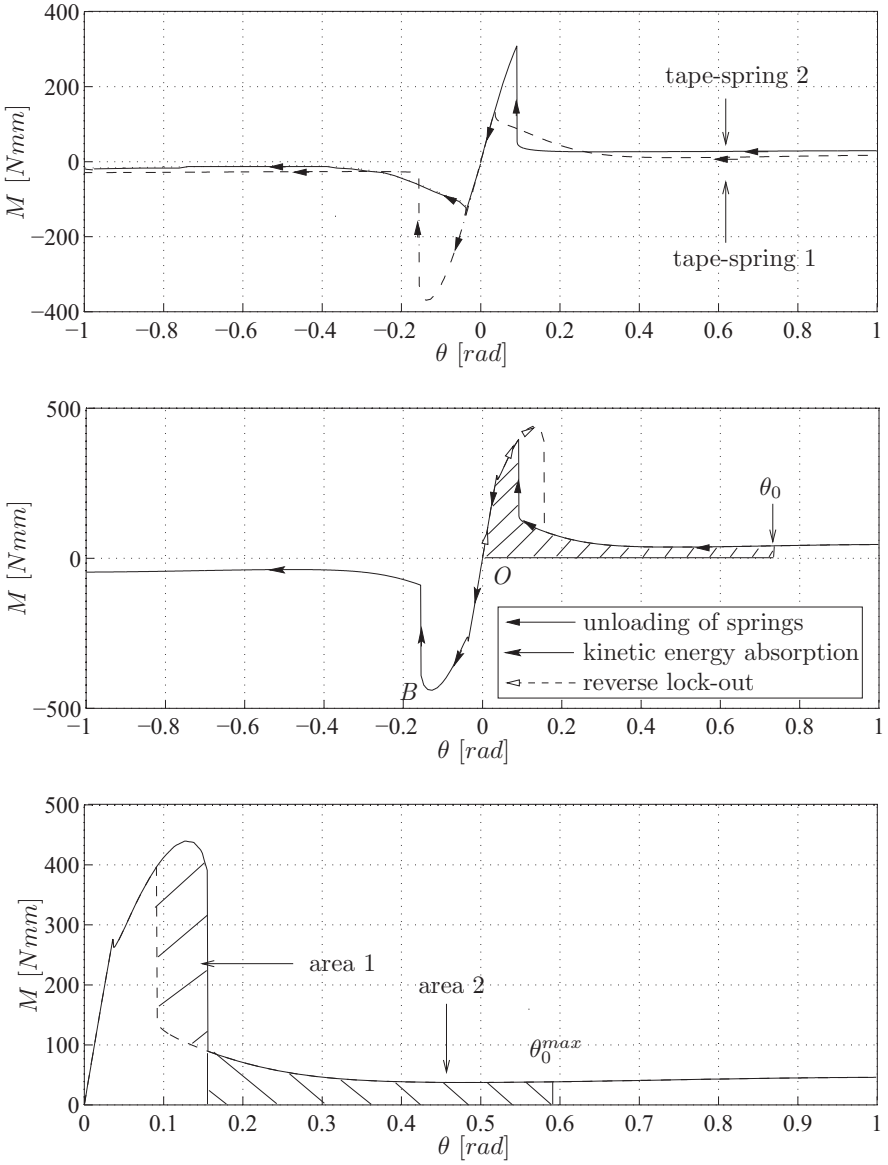

Figure 3.3: Moment-rotation relationship of a composite hinge: (a) separate relationships for the two tape-springs; (b) relationship for the composite hinge; (c) difference between positive and negative moment areas. Each tape-spring is of $R = 10\ mm$, $L = 100\ mm$, $t = 0.1\ mm$ and $\alpha = 110°$.

unload in the opposite direction. Since the bending behaviour is now restricted to the pre-buckled states of both springs, the moment response in the opposite direction, after the rigid element has passed through the zero angle position, is the same, see Fig. 3.3(b). Therefore, the rigid element oscillates back and forth. The frequency of oscillation depends on the inertia properties of the rigid element

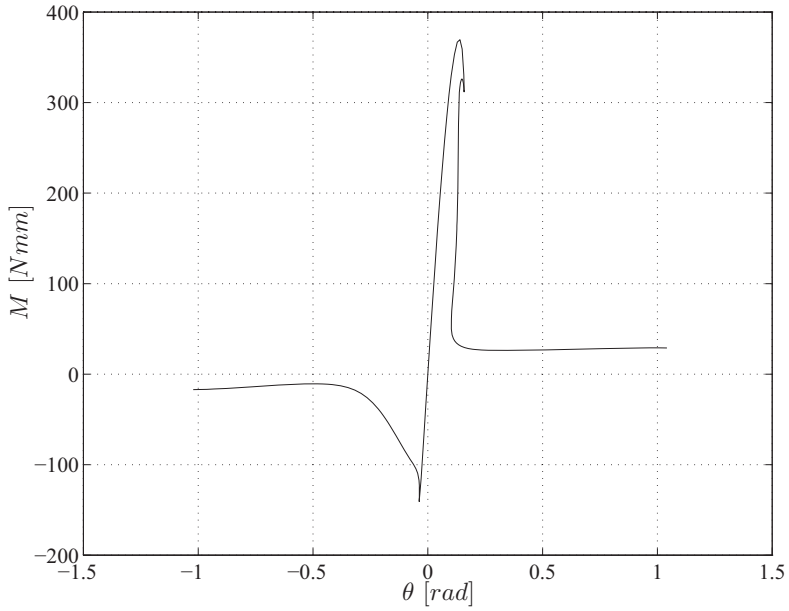

Figure 3.4: Moment-rotation relationship of single tape-spring in the composite hinge described by Fig. 3.3.

and on the pre-buckled bending stiffness of the composite tape-springs.

Note that knowledge of the unstable portion of the moment-rotation relationship of an individual tape-spring, between the nose and the heel for bending in the opposite sense, see Chapter 2, is not required to construct any of these plots.

Figure 3.5 summarises the deployment behaviour for sets of composite tape-springs with radius $R = 10\ mm$. The individual tape-spring bending responses were obtained using the finite-element procedure of Chapter 2. Appendix B gives further details on the deployment behaviour of many different tape-spring geometries.

There a several points to note regarding the relationship between the maximum deployment angle and the composite hinge geometry.

In Chapter 2, it was noted that tape-springs with the same cross-sectional properties and subject to equal-sense bending have the same peak moment, approximately the same behaviour as the fold begins to form, and the same steady state moment values regardless of the length of spring. However, the initial stiffness against bending, both in the equal and opposite sense of bending, increases for a decreasing length of spring. For opposite-sense bending the rotation at which the heel forms is also approximately the same, regardless of length. This tape-spring, therefore, snaps back to a higher bending moment. The available energy for deployment of the rigid element, and hence its maximum kinetic energy, slightly increases as the the length of the composite spring decreases. From

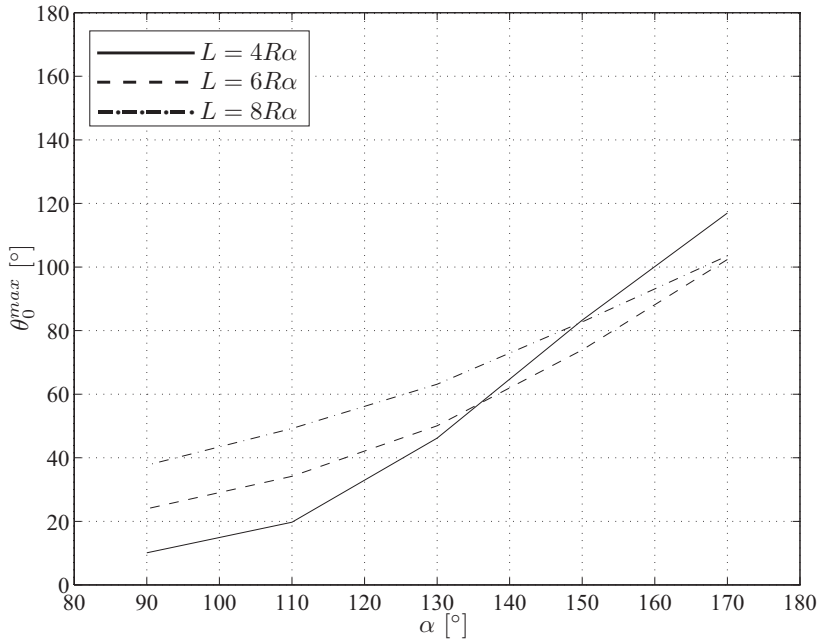

Figure 3.5: Maximum deployment angle that avoids overshoot for composite tape-springs with $R = 10\ mm$ and $t = 0.1\ mm$.

Fig. 2.7 and the plots of Appendix A, the kinetic energy that can be absorbed without snap-through also increases as the tape-spring becomes shorter. Thus, by the equal areas argument, the relationship between the length of the composite hinge and maximum deployment angle is non-linear, for a given α.

Chapter 4

Experiment Design

This chapter describes the design of an experiment that enables deployment of a rigid element, *i.e.* a panel, by a set of composite tape-spring hinges. Section 4.1 presents the design of a variable inertia, hinge deployed panel. The location of the centre of rotation of the panel is discussed in Section 4.2. The suspension rig, that compensates for the effects of gravity during deployment, is designed in Section 4.3.

4.1 Design of Panel

A panel that is deployed by a set of tape-springs was made according to the following design criteria:

- the panel should be effectively rigid compared to the stiffness of the deploying tape-springs;
- the section dimensions and inertia properties are representative of actual panels, namely, a surface area of 1 m^2, a mass of about 10 kg, and a moment of inertia about the edge connected to the tape-springs between 5 kgm^2 and 10 kgm^2;
- the panel provides a universal mount for tape-springs of different cross-sections;
- the moment of inertia of the panel can be varied.

The panel was constructed and is shown schematically in Fig. 4.1. The depth and length are 1.0 m and 1.3 m, respectively. The vertical base element of the panel is made from solid Al-alloy bar into which sets of threaded holes 60 mm apart have been tapped to provide fixtures for the tape-springs. Three lengths

of right-angled Dexion bar are connected to the base by means of machined Al-alloy adaptor blocks. The Dexion bars are connected together at the end of the panel. This triangulated arrangement imparts in-plane stiffness to the panel. A steel block of mass 3.20 kg is attached to the end of the horizontal element to increase the moment of inertia of the panel about its base. The moment of inertia of the panel can then be varied by connecting two additional, identical mass blocks at equal distances on either side of the vertical centroidal axis on the horizontal Dexion element. Thus, the designated position of the centre of mass of the panel remains unchanged when its inertia is varied and, hence, the position of the gravity-compensation suspension point need not be changed.

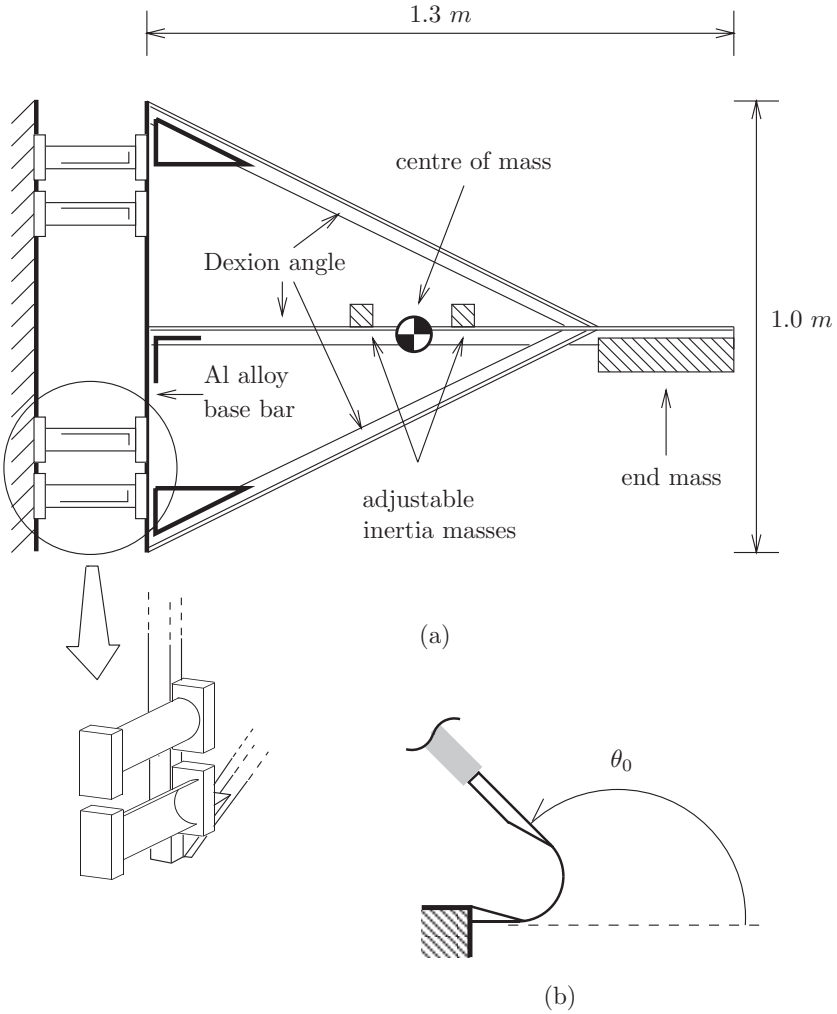

Figure 4.1: Schematic layout of panel: (a) side-view with composite hinge detail; (b) partial plan view and initial folded angle.

The panel was weighed to obtain its mass. The vertical centroidal axis was located by positioning the panel on a knife-edge until it balanced. The moment of inertia of the panel about it centre of mass was found by mounting the panel vertically in a fixed bearing bracket and measuring the period of oscillation for free vibrations. These properties are listed in Table 4.1 and have been confirmed by calculation using the individual masses and moments of inertia of each component as constructed in the panel.

mass, m_p $[kg]$	8.622
moment of inertia about centroid, I_p $[kgm^2]$	2.129
distance of vertical centroidal axis from base edge, a_p $[m]$	0.737

Table 4.1: Panel properties without additional masses.

The moment of inertia of the panel about its base, I_0, is thus

$$I_0 = I_p + m_p {a_p}^2 = 6.9 \ \ kgm^2 \tag{4.1}$$

4.2 Position of Centre of Rotation

The tape-springs have a finite length. Therefore, the centre of rotation of the panel is not located at the fixed support of the tape-springs. During initial deployment, the inertia loading applied by the panel to the tape-springs causes the folds to move *slowly* towards the fixed support end. The constraint applied by the rigidly encased ends stops any further advance of the folds. It is assumed that all tape-springs deform identically. Therefore, the distance of the start of each fold from the base is p_1, see detail in Fig. 4.2.

As the panel deploys, the arc-length of the folds decreases. All points from the base to the end of the fold have zero velocity. Thus, at any instant, the centre of rotation of the panel is located at the end of the fold as shown in detail in Fig. 4.2. By considering the position of the end of the folds for the folded and deployed configurations, an average position for the centre of rotation can be obtained. This is given by point C, with coordinates

$$\begin{aligned} C_x &= p_1 + \frac{R\pi}{2} \\ C_y &= R \end{aligned} \tag{4.2}$$

for $\theta_0 = \pi \ rad$. The locus of the centre of mass of the panel during deployment is shown in the main part of Fig. 4.2. A semi-circular arc, originating from point C and passing through the start and end positions of the panel, is fitted to the locus. This provides a fixed radius for the point of suspension of the gravity compensation system. Its axis of rotation is therefore coincident with the average centre of rotation of the panel.

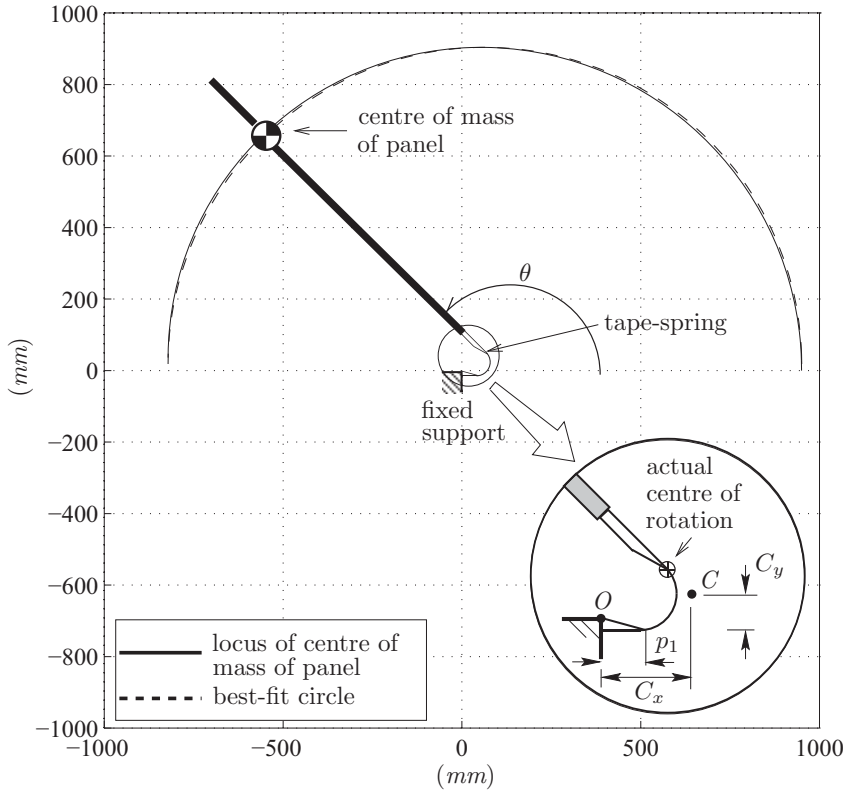

Figure 4.2: Position of the centre of mass of the panel during deployment. Inset: positions of actual centre of rotation of the panel centre of mass for a deployment angle θ and average centre C for deployment angle range of 180°.

4.3 Design of Experimental Rig

An experimental rig was designed and constructed that enabled the panel and tape-springs to be connected to a fixed foundation, as well as providing a means of compensating for the effects of gravity during deployment.

The influence of gravity is overcome by having the axis of rotation of the panel in the vertical direction so that each tape-spring rotates in a horizontal plane. The weight of the panel is offloaded from the ends of the tape-springs by means of a suspension system that rotates with the panel during deployment. The suspension system consists of a light Al-alloy jib with its vertical axis mounted in virtually frictionless, self-aligning bearings. The panel is connected from its centroid to a steel cable passing over pulleys to a counterweight that is located on the axis of rotation of the jib, see Fig. 4.3.

The counterweight consists of a steel box filled with lead shot. Its total mass

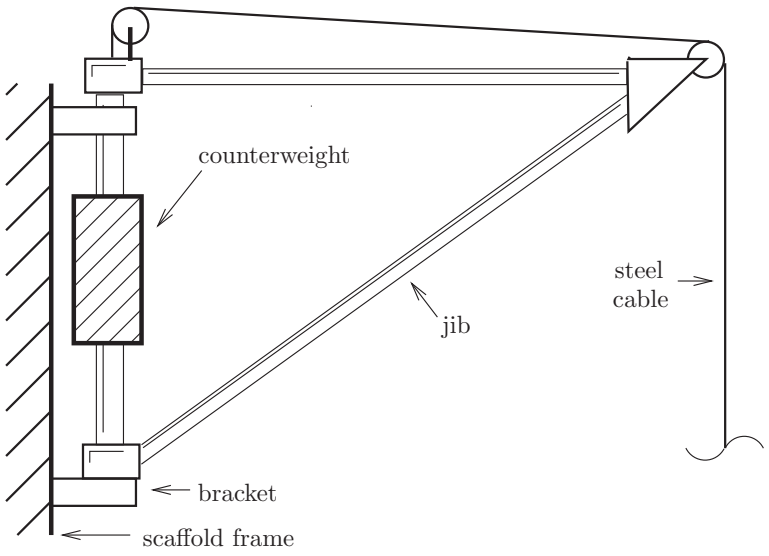

Figure 4.3: Schematic layout of suspension system.

is equal to the mass of the panel and it is free to move in the vertical direction to accommodate any lag in motion between the panel and the jib. The counterweight, however, cannot rotate relative to the vertical axis of the jib. The suspension system is connected by steel brackets to a purpose-built scaffold frame and is located well above the panel so that any changes in the vertical cable angle during deployment give rise to small components of horizontal force applied to the panel. The fixed ends of the tape-springs are connected to a vertical bar, which is in turn connected by adjustable clamps to the scaffold frame. The position of the bar in the horizontal plane can be adjusted to align the axes of rotation of the jib and of the panel. The length of the jib is fixed and hence, to test tape-springs of different lengths, balance masses are attached to the panel to ensure that its centre of mass is directly below the end of the jib.

mass, m_j $[kg]$	1.550
length of jib, l_j $[m]$	0.855
distance of centroid from vertical shaft, a_j $[m]$	0.340
moment of inertia about centroid, I_j $[kgm^2]$	0.153

Table 4.2: Suspension system properties for the jib components.

A video camera is mounted above the suspension system to provide a vertical view and record of the deployment sequence. The properties of the suspension system, excluding the counterweight, are given in Table 4.2. The counterweight has a moment of inertia about its centroid of approximately 0.0166 kgm^2 when not filled with shot.

Chapter 5

Experiments and Theoretical Analysis

This chapter begins by presenting deployment experiments of the panel. Then, Section 5.2 details the derivation of two-degree of freedom model that simulates the coupled deployment of the panel and compensation system. A comparison of theoretical and predicted results is carried out in Section 5.3. The chapter concludes with a brief discussion in Section 5.4.

5.1 Experimental Procedure and Results

The panel was deployed by two sets of tape-springs whose section properties are given in Table 5.1. Each set consisted of two identical pairs of composite hinges. The values of p_1, Fig. 4.2, were obtained by direct measurement when the panel was folded. No inertia masses were attached to the panel and, hence, its properties are those of Table 4.1. A steel balance block of mass 0.881 kg was fixed to the panel, but offset normal to the plane of the panel to ensure alignment of the base of the panel with the vertical. This increased the mass of the panel, m_p, to 9.503 kg without appreciable change in I_p; the position of the centre of mass of the panel also changed to $a_p = 741$ mm for the first set of tape-springs, and $a_p = 725$ mm for the second set.

A tape-spring from the first set was tested in a bending jig (Fischer 1995) to measure its moment-rotation relationship. The geometry of the second set was chosen with reference to Section 3.2 to enable the panel to deploy without overshooting from a large initial folded angle.

The rotation of the panel during deployment was recorded with a video camera, and the angular position of the panel in each frame was digitised and plotted. An accelerometer was attached to the tip of the panel to provide data on the post lock-out vibration. A dial indicator was fixed to the vertical shaft of the suspension

system and pressed against the base of the counterweight. This indicated any vertical motion of the counterweight.

tape-set	$R\ [mm]$	$\alpha\ [^\circ]$	$L\ [mm]\ (\times R\alpha)$	$t\ [mm]$	$p_1\ [\times R]$
1	28.1	103.4	210 (4.14)	0.1	2.5
2	20.6	144.8	230 (4.42)	0.1	3.7

Table 5.1: Tape-spring section properties of composite hinges.

The rotation of the panel, deployed by the first set of tape-springs, up until the initial lock-out phase is shown in Fig. 5.1(a).

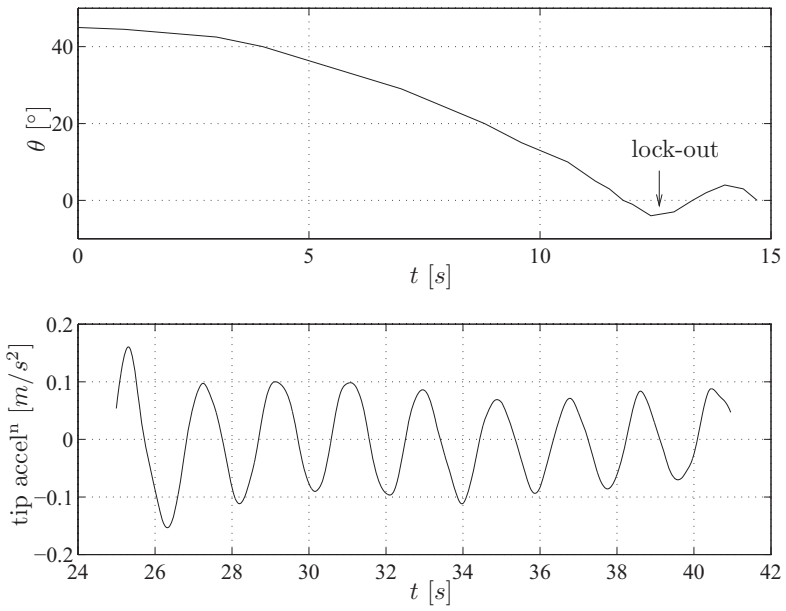

Figure 5.1: Experimental deployment by first set of tape-springs: (a) plot of deployment; (b) post lock-out vibration (filtered to remove signal noise in the original data).

A maximum initial deployment angle of approximately 45° was attainable without the panel overshooting. The tape-springs initially straighten out 12.0 seconds after the start of deployment. The direction of rotation of the panel reverses and the tape-springs subsequently prevent overshoot in the opposite direction. The panel then continues to oscillate about the zero angle position as the amplitude of the tip decreases. The lateral acceleration of the tip of the panel during the post lock-out vibration stage is shown in Fig. 5.1(b). The period of oscillation is approximately 1.9 seconds. Deployment of the panel with overshoot was carried out several times and the tape-springs showed no obvious damage on account on snapping through.

Figure 5.2 details the experimental moment-rotation relationship of one of the tape-springs. A prediction of the bending response by a finite-element analysis is also shown. The elastic compliance of the testing apparatus results in a smaller initial bending stiffness for the tape-spring when compared to the finite-element data.

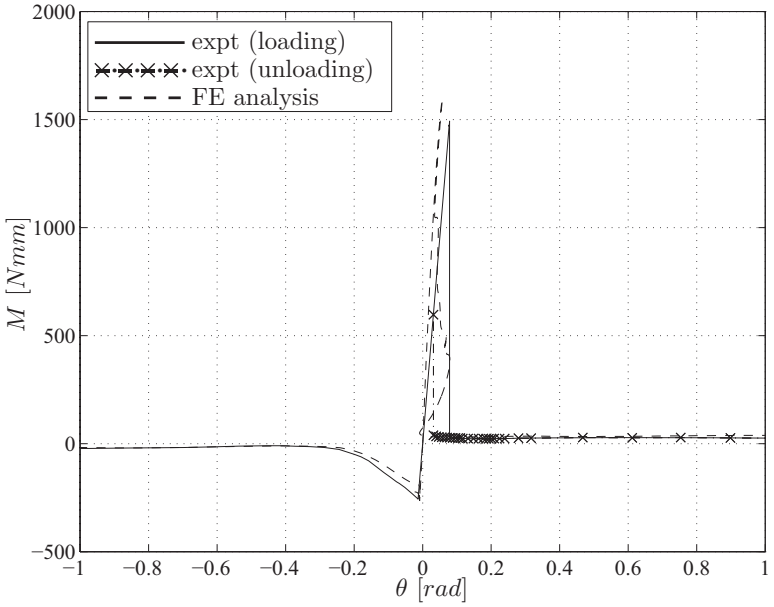

Figure 5.2: Moment-rotation relationship of a single tape-spring from the first set (see Table 5.1). Note that loading and unloading for equal-sense bending is the same, and hence the unloading curve for this direction is not shown.

Two experiments for the deployment of the panel by the second set of tape-springs are shown in Fig. 5.3. Deployment from an initial folded angle of 138° did not cause overshooting, but when this angle was increased to 152° the panel overshot lock-out; this is verified in Fig. 5.4 where values of θ_0^{max} are plotted against α for $R = 20.6\ mm$, $t = 0.1\ mm$ and $L = 4.42R\alpha$. This plot was obtained using the deployment predictions from Appendix B. From Fig. B.1, linear interpolation between the lines $L = 4R\alpha$ and $L = 6R\alpha$ for $L = 4.42R\alpha$ gives values of θ_0^{max} for $R = 20\ mm$. Similarly, from Fig. B.2 ($R = 30\ mm$), values of θ_0^{max} are also computed for spring lengths of $L = 4.42R\alpha$. Finally, by further linear interpolation between these two sets of values of maximum deployment angle for a radius of 20.6 mm gives the resulting curve in Fig. 5.4. The experiments are also shown in this figure and, as it can be seen, the first experiment lies below the line of maximum deployment angle, whereas the second experiment lies above, indicating that the panel overshoots. Table 5.2 summarises the experimental and theoretical behaviour. The tape-springs incurred plastic damage in the second experiment as they snapped through and further rotation beyond this point, in

the same direction, was impaired. In both experiments the panel locks out in the reverse direction and then continues to oscillate with a decaying amplitude. Post lock-out vibration details are given in Table 5.3. Note that the large initial stiffness of the tape-springs made it impossible to measure their moment-rotation relationship on the testing apparatus.

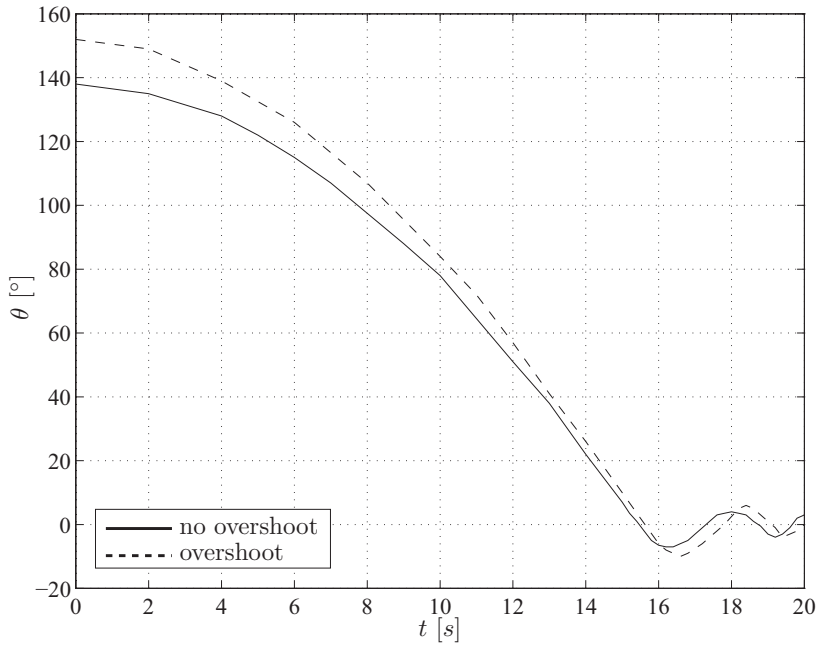

Figure 5.3: Deployment angle of panel, tape-set 2.

In all of the experiments, the fully deployed state of the panel corresponded exactly to the initial, extended position of the panel, *i.e.* the tip of the panel did not move vertically during deployment. The counterweight moved by only a few millimetres just before the first lock-out of the tape-springs took place. During post lock-out vibration the amount of relative displacement between the counterweight and the vertical shaft of the suspension system was less than 1 mm.

θ_0 [°]	experiment	theory
138	does not overshoot	does not overshoot
152	overshoots	overshoots

Table 5.2: Comparison between experimental behaviour and theoretical predictions from Fig. 5.4.

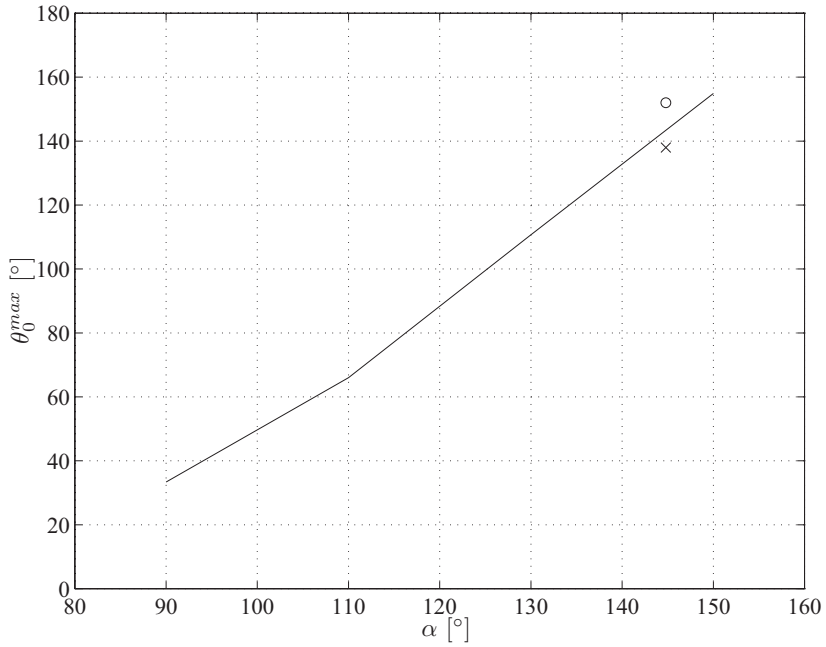

Figure 5.4: Maximum deployment angle that avoids overshoot for a composite hinge with $R = 20.6\ mm$, $t = 0.1\ mm$ and $L = 4.42R\alpha$, and corresponding to the second set of tape-springs. First and second experiments denoted by "×" and "○", respectively.

Experiment	Number of oscillations to zero amplitude vibration	time of decay $[s]$	frequency of vibration $[Hz]$
no overshoot	72	116.5	0.62
overshoot	78	122.4	0.64

Table 5.3: Post lock-out vibration behaviour of the panel when deployed by second set of tape-springs.

5.2 Analysis of Deployment

Experimental observation suggests that the centroid of the panel moves in a horizontal plane during deployment. Thus, the counterweight moves up and down to accommodate any changes in distance between the tip of the suspension system and the panel. Figure 5.5 shows the two degree-of-freedom model that takes account of these features.

The panel is modelled as a rigid element GH of mass m_p and of moment of inertia I_p about its centroid. The distance from the edge of the panel to its centroid is a_p. The panel is connected to a rigid foundation O by n pairs of composite tape-spring hinges which are flexible in the horizontal plane only. Each tape-spring is idealised as three interconnected bodies; OE, EF and FG. In analogy with

Section 4.2, body OE is rigid and of a fixed length p_1. Body EF, representing the fold region, subtends an arc-length $R\theta$, where θ is the angle between the current configuration of the panel and its fully deployed configuration. Body FG is rigid, but of variable length p_2. If the total length of the tape-spring is L, then p_2 can be related to θ by

$$p_2 = L - p_1 - R\theta \tag{5.1}$$

The unit vectors $\mathbf{i}$, $\mathbf{j}$ and $\mathbf{k}$ form a fixed, orthogonal, right-handed set, and $\mathbf{e}_\theta$, $\mathbf{e}_\theta^*$ are the auxiliary unit vectors, respectively parallel and normal to the panel.

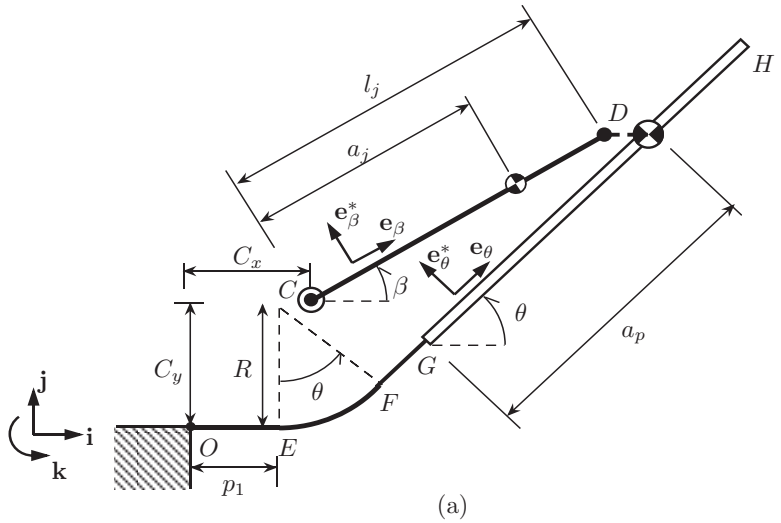

(a)

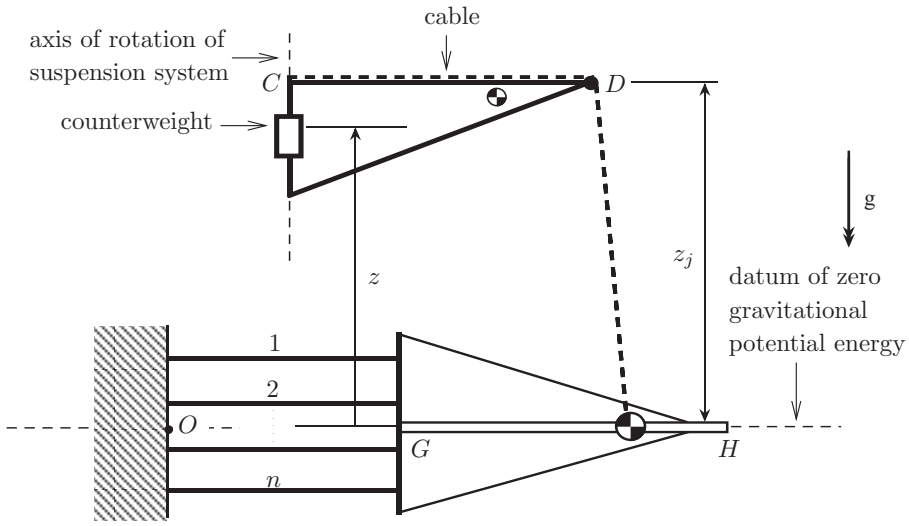

(b)

Figure 5.5: Theoretical model of panel and suspension system: (a) plan view; (b) side view.

The suspension, comprising all moving components of the suspension system except for the counterweight, see Fig. 4.3, is also modelled as a rigid element *CD* that rotates about a vertical axis. Let z_j be the vertical distance between the horizontal plane of the centroid of the panel and the horizontal plane of the tip of jib. The associated angle of rotation is β. The axis of rotation of the jib is offset from O by the distances C_x and C_y in the $\mathbf{i}$ and $\mathbf{j}$ directions, respectively, see Section 4.2. The distance from the vertical axis of rotation to the centroid is a_j and the overall length of the jib is l_j. The centroid has mass m_j and moment of inertia I_j about its centroid. The auxiliary unit vectors $\mathbf{e}_\beta$ and $\mathbf{e}^*_\beta$ are parallel and normal to the suspension system, respectively.

The counterweight is located on the axis of rotation of the suspension at a vertical height z above the panel. Its mass is m_w and the moment of inertia about its centroid is I_w.

The datum for zero gravitational potential energy is defined as the horizontal plane passing through the centroid of the panel.

The three coordinates for this system are θ, β and z. However, an equation of constraint relates z to θ and β since the cable connecting the counterweight to the panel is of a fixed length. Therefore, θ and β are the two degrees of freedom of the combined system and the equations of motion are formulated using a *Lagrangian* approach, *i.e.* in terms of kinetic and potential energies.

The height of the counterweight above the horizontal plane of motion of the panel can be expressed in terms of the total cable length l_c and associated terms as follows

$$z = z' + \sqrt{a^2 + b^2 + c^2} \tag{5.2}$$

where

$$\begin{aligned} z' &= z_j - l_c + l_j \\ a &= [C_x - p_1 + l_j \cos\beta - R\sin\theta - (p_2 + a_p)\cos\theta] \\ b &= [C_y - R + l_j \sin\beta + R\cos\theta - (p_2 + a_p)\sin\theta] \\ c &= z_j \end{aligned} \tag{5.3}$$

5.2.1 Formulation of Lagrangian

The centroid of the panel is identified by the vector

$$\mathbf{r}_p = p_1\mathbf{i} + R(\mathbf{j} - \mathbf{e}^*_\theta) + (p_2 + a_p)\mathbf{e}_\theta \tag{5.4}$$

Substituting Eq. 5.1 into Eq. 5.4 and differentiating with respect to time yields

$$\dot{\mathbf{r}}_p = (L - p_1 - R\theta + a_p)\dot{\theta}\mathbf{e}^*_\theta \tag{5.5}$$

The kinetic energy of the panel can expressed as

$$T_p = \frac{1}{2} m_p \dot{\mathbf{r}}_p^2 + \frac{1}{2} I_p \dot{\theta}^2 \tag{5.6}$$

Inserting Eq. 5.5 into Eq. 5.6 gives

$$T_p = \frac{1}{2} m_p (L - p_1 - R\theta + a_p)^2 \dot{\theta}^2 + \frac{1}{2} I_p \dot{\theta}^2 \tag{5.7}$$

Similarly, the centroid of the jib is given by the position vector

$$\mathbf{r}_s = C_x \mathbf{i} + C_y \mathbf{j} + z_j \mathbf{k} + a_j \mathbf{e}_\beta \tag{5.8}$$

Hence, its velocity is

$$\dot{\mathbf{r}}_s = a_j \dot{\beta} \mathbf{e}_\beta^* \tag{5.9}$$

and its kinetic energy is therefore

$$T_j = \frac{1}{2} m_j a_j^2 \dot{\beta}^2 + \frac{1}{2} I_j \dot{\beta}^2 \tag{5.10}$$

The counterweight has a centroidal velocity $\dot{z}\mathbf{k}$ and an angular velocity of $\dot{\beta}\mathbf{k}$. Its kinetic energy is, by analogy with the above,

$$T_w = \frac{1}{2} m_w \dot{z}^2 + \frac{1}{2} I_w \dot{\beta}^2 \tag{5.11}$$

Since the motions of the panel and of the suspension jib take place in the horizontal planes containing their respective centroids, their gravitational potential energy does not change during deployment. However, the counterweight can displace in the vertical direction and therefore its gravitational potential energy term contributes to the equations of motion and is given by

$$V_w = m_w g z \tag{5.12}$$

where g is the acceleration due to gravity. The tape-springs have a combined elastic potential energy of

$$V = V(\theta) \tag{5.13}$$

$V(\theta)$ is equal to the area under the appropriate composite moment-rotation relationship curve. The Lagrangian for the system, $\mathcal{L}$, defined as the difference between the total kinetic and potential energies, is

$$\mathcal{L} = T_p + T_j + T_w - V_w - V \tag{5.14}$$

Therefore, by substitution of the appropriate terms

$$\begin{aligned} \mathcal{L} \;=\; & \frac{1}{2} m_p (L - p_1 - R\theta + a_p)^2 \dot{\theta}^2 + \frac{1}{2} I_p \dot{\theta}^2 + \frac{1}{2} m_j a_j^2 \dot{\beta}^2 \\ & + \frac{1}{2} I_j \dot{\beta}^2 + \frac{1}{2} m_w \dot{z}^2 + \frac{1}{2} I_w \dot{\beta}^2 - m_w g z - V(\theta) \end{aligned} \tag{5.15}$$

5.2.2 Equations of Motion

In analogy with Rimrott (1980), the equations of motion for this system are derived by an application of Lagrange's equations (Synge and Griffith 1970)

$$\frac{d}{dt}\left(\frac{\partial \mathcal{L}}{\partial \dot{q}_i}\right) - \frac{\partial \mathcal{L}}{\partial q_i} = Q_i \tag{5.16}$$

In this equation q_i represent the generalised coordinates of the system, *i.e.* θ and β; Q_i are the generalised forces corresponding to non-conservative forces acting on the system and are: aerodynamic drag acting on the panel, friction in the support bearings and material damping in the tape-springs.

The first equation of motion is obtained by differentiating Eq. 5.15 with respect to θ, and also to $\dot{\theta}$ and then t, and then substituting into Eq. 5.16 to give

$$\begin{aligned} m_p\big[(L - p_1 - R\theta + a_p)\ddot{\theta} - R\dot{\theta}^2\big](L - p_1 - R\theta + a_p) + I_p\ddot{\theta} \\ + \frac{1}{2}m_w\left[\frac{d}{dt}\frac{\partial(\dot{z}^2)}{\partial\dot{\theta}} - \frac{\partial(\dot{z}^2)}{\partial\theta} + 2g\frac{\partial z}{\partial\theta}\right] + \frac{\partial V}{\partial\theta} &= Q_\theta \end{aligned} \tag{5.17}$$

The first term inside the bracket on the second line of Eq. 5.17 can be expressed as

$$\frac{\partial(\dot{z}^2)}{\partial\dot{\theta}} = \frac{\partial(\dot{z})^2}{\partial\dot{z}}\frac{\partial\dot{z}}{\partial\dot{\theta}} = 2\dot{z}\frac{\partial\dot{z}}{\partial\dot{\theta}} \tag{5.18}$$

However

$$\frac{\partial\dot{z}}{\partial\dot{\theta}} = \frac{\partial z}{\partial\theta} \tag{5.19}$$

and by virtue of Eq. 5.2

$$\frac{\partial z}{\partial\theta} = (a^2 + b^2 + c^2)^{-\frac{1}{2}}\left[a\frac{\partial a}{\partial\theta} + b\frac{\partial b}{\partial\theta}\right] \tag{5.20}$$

$$\dot{z} = (a^2 + b^2 + c^2)^{-\frac{1}{2}}(a\dot{a} + b\dot{b}) \tag{5.21}$$

Substituting Eq. 5.20 into Eq. 5.19, and then substituting the resulting expression along with Eq. 5.21 into Eq. 5.18 yields

$$\frac{\partial(\dot{z}^2)}{\partial\dot{\theta}} = 2(a^2 + b^2 + c^2)^{-1}(a\dot{a} + b\dot{b})\left[a\frac{\partial a}{\partial\theta} + b\frac{\partial b}{\partial\theta}\right] \tag{5.22}$$

The second term inside the bracket of Eq. 5.17 can be written as

$$\frac{\partial(\dot{z}^2)}{\partial\theta} = 2\dot{z}\frac{\partial\dot{z}}{\partial\theta} \tag{5.23}$$

where

$$\begin{aligned}\frac{\partial \dot{z}}{\partial \theta} &= -\frac{1}{2}(a^2+b^2+c^2)^{-\frac{3}{2}}\left[2a\frac{\partial a}{\partial \theta}+2b\frac{\partial b}{\partial \theta}\right](a\dot{a}+b\dot{b}) \\ &\quad +(a^2+b^2+c^2)^{-\frac{1}{2}}\left[a\frac{\partial \dot{a}}{\partial \theta}+\dot{a}\frac{\partial a}{\partial \theta}+b\frac{\partial \dot{b}}{\partial \theta}+\dot{b}\frac{\partial b}{\partial \theta}\right] \end{aligned} \tag{5.24}$$

from Eq. 5.21. Therefore, substituting Eq. 5.21 and Eq. 5.24 into Eq. 5.23 gives

$$\begin{aligned}\frac{\partial(\dot{z}^2)}{\partial \theta} &= 2(a\dot{a}+b\dot{b})\left[a\frac{\partial \dot{a}}{\partial \theta}+\dot{a}\frac{\partial a}{\partial \theta}+b\frac{\partial \dot{b}}{\partial \theta}+\dot{b}\frac{\partial b}{\partial \theta}\right](a^2+b^2+c^2)^{-1} \\ &\quad -(a\dot{a}+b\dot{b})^2\left[2a\frac{\partial a}{\partial \theta}+2b\frac{\partial b}{\partial \theta}\right](a^2+b^2+c^2)^{-2} \end{aligned} \tag{5.25}$$

Differentiation of Eq. 5.22 with respect to time and substitution of the resulting expression along with Eq. 5.20 and Eq. 5.25 into Eq. 5.17 and tidying up of terms results in the equation of motion in θ as

$$\begin{aligned} & m_p\left[(L-p_1-R\theta+a_p)\ddot{\theta}-R\dot{\theta}^2\right](L-p_1-R\theta+a_p)+I_p\ddot{\theta} \\ & +\frac{m_w}{a^2+b^2+c^2}\left[a\frac{\partial a}{\partial \theta}+b\frac{\partial b}{\partial \theta}\right]\left[\dot{a}^2+\dot{b}^2+a\ddot{a}+b\ddot{b}-\frac{(a\dot{a}+b\dot{b})^2}{a^2+b^2+c^2}\right] \\ & +\frac{m_w g}{\sqrt{a^2+b^2+c^2}}\left[a\frac{\partial a}{\partial \theta}+b\frac{\partial b}{\partial \theta}\right]+\frac{\partial V}{\partial \theta}=Q_\theta \end{aligned} \tag{5.26}$$

where

$$\dot{a}=(L-p_1-R\theta+a_p)\dot{\theta}\sin\theta-l_j\dot{\beta}\sin\beta \tag{5.27}$$

$$\begin{aligned}\ddot{a} &= (L-p_1-R\theta+a_p)(\ddot{\theta}\sin\theta+\dot{\theta}^2\cos\theta) \\ &\quad -l_j(\ddot{\beta}\sin\beta+\dot{\beta}^2\cos\beta)-R\dot{\theta}^2\sin\theta \end{aligned} \tag{5.28}$$

$$\dot{b}=-(L-p_1-R\theta+a_p)\dot{\theta}\cos\theta+l_j\dot{\beta}\cos\beta \tag{5.29}$$

$$\begin{aligned}\ddot{b} &= (L-p_1-R\theta+a_p)(\dot{\theta}^2\sin\theta-\ddot{\theta}\cos\theta) \\ &\quad +l_j(\ddot{\beta}\cos\beta-\dot{\beta}^2\sin\beta)+R\dot{\theta}^2\cos\theta \end{aligned} \tag{5.30}$$

$$\frac{\partial a}{\partial \theta}=(L-p_1-R\theta+a_p)\sin\theta \tag{5.31}$$

$$\frac{\partial b}{\partial \theta}=-(L-p_1-R\theta+a_p)\cos\theta \tag{5.32}$$

from the relationships in Eqs. 5.3. $\partial V/\partial\theta$ is simply the moment-rotation response of all of the composite hinges.

A second, independent equation of motion is obtained by differentiating $\mathcal{L}$ with respect to β, and also to $\dot{\beta}$ and t and substituting into Eq. 5.16, and by performing similar calculus operations as in Eqs. 5.18 to 5.25 to yield

$$\frac{m_w}{a^2+b^2+c^2}\left[a\frac{\partial a}{\partial\beta}+b\frac{\partial b}{\partial\beta}\right]\left[\dot{a}^2+\dot{b}^2+a\ddot{a}+b\ddot{b}-\frac{(a\dot{a}+b\dot{b})^2}{a^2+b^2+c^2}\right]$$
$$+m_j a_j^2\ddot{\beta}+I_j\ddot{\beta}+I_w\ddot{\beta}+\frac{m_w g}{\sqrt{a^2+b^2+c^2}}\left[a\frac{\partial a}{\partial\beta}+b\frac{\partial b}{\partial\beta}\right]=Q_\beta \tag{5.33}$$

where

$$\frac{\partial a}{\partial\beta}=-l_j\sin\beta \tag{5.34}$$

$$\frac{\partial b}{\partial\beta}=l_j\cos\beta \tag{5.35}$$

Equations 5.26 and 5.33 form a system of two non-linear, coupled differential equations which are solved numerically using the fourth-order Runge-Kutta routine available within the software package MATLAB (Mathworks 1995).

For an initial folded angle of the panel, θ_0, the suspension is at an angle β_0 such that the connecting cable applies zero force perpendicular to the vertical plane of the suspension system, *i.e.*

$$\tan^{-1}\frac{a}{b}=\beta_0 \tag{5.36}$$

Equation 5.36 is solved iteratively to obtain the appropriate value of β_0 for a given θ_0.

5.3 Comparison of Simulation and Experiment

The measured relationship between bending moment and deployment angle of the first set of tape-springs is shown in Fig. 5.6. Similarly, Fig. 5.7 indicates the response simulated by a finite-element analysis of a single tape-spring, and assembling the results as shown in Fig. 5.2. Both plots are only valid for deployment without overshoot, *c.f.* Fig. 3.3(b). In general, there is good agreement between the plots, however, the finite-element analysis predicts a slightly higher unstable peak moment. There is also no jump in moment just before the zero angle position during initial unloading. For a general angle of rotation of the panel, the value of $\partial V/\partial\theta$ in Eq. 5.26 is obtained by reading the corresponding value of moment from either curve.

The equal areas condition for deployment without overshoot, Section 3.2, yields an initial deployment angle $\theta_0^{max}=0.895\ rad$ (51.3°) if the measured response

curve is used, whereas the curve predicted by the finite-element analysis results in $\theta_0^{max} = 0.883\ rad\ (50.6°)$.

It is assumed that the effects of air drag, friction in the support bearings, and material damping in the tape-springs are small. Therefore, Q_θ and Q_β are set to zero in Eqs. 5.26 and 5.33, respectively. The appropriate panel, suspension system and tape-spring properties are substituted into the equations of motion along with the values of the parameters in Table 5.4.

$C_x\ [mm]$	$C_y\ [mm]$	$a_p\ [m]$	$z_j\ [m]$	$l_c\ [m]$	$\theta_0\ [°]$	$\beta_0\ [°]$
100.3	18	0.741	1.7	2.75	45.0	45.13

Table 5.4: Geometric parameters used in deployment simulation with first set of tape-springs.

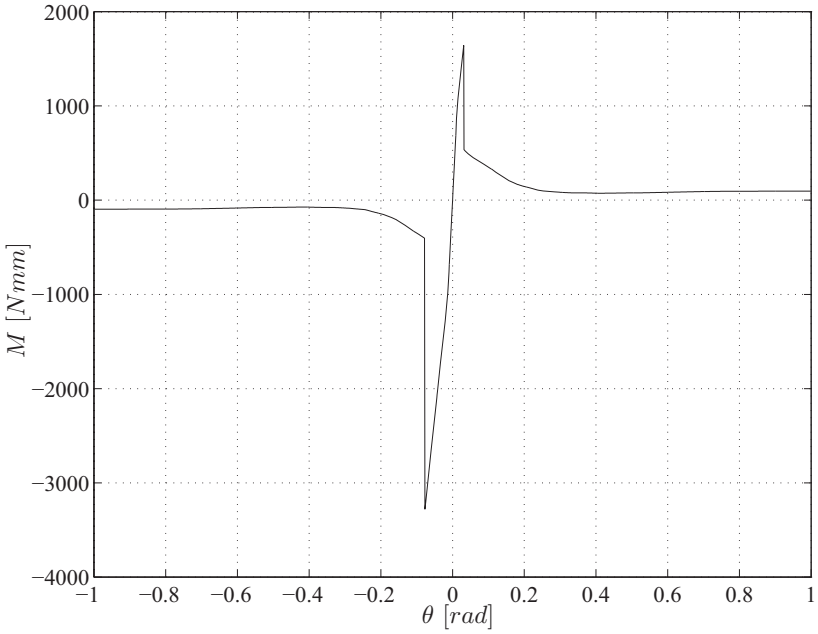

Figure 5.6: Measured behaviour of composite tape-spring hinges.

Figure 5.8 shows two different deployment simulations, corresponding to the two different moment-rotation relationships. The deployment response using the finite-element relationship predicts that the panel first stops moving after 12.2 s, and the corresponding deployment angle is $-0.053\ rad\ (-3.08°)$. Thereafter, a post lock-out vibration occurs, with a period of approximately 2.5 s. If, instead of using the finite-element based relationship, the experimental relationship is used, the predicted times to the first cessation of motion and period of oscillation are 13.2 s and 2.89 s, respectively, and the corresponding deployment angle

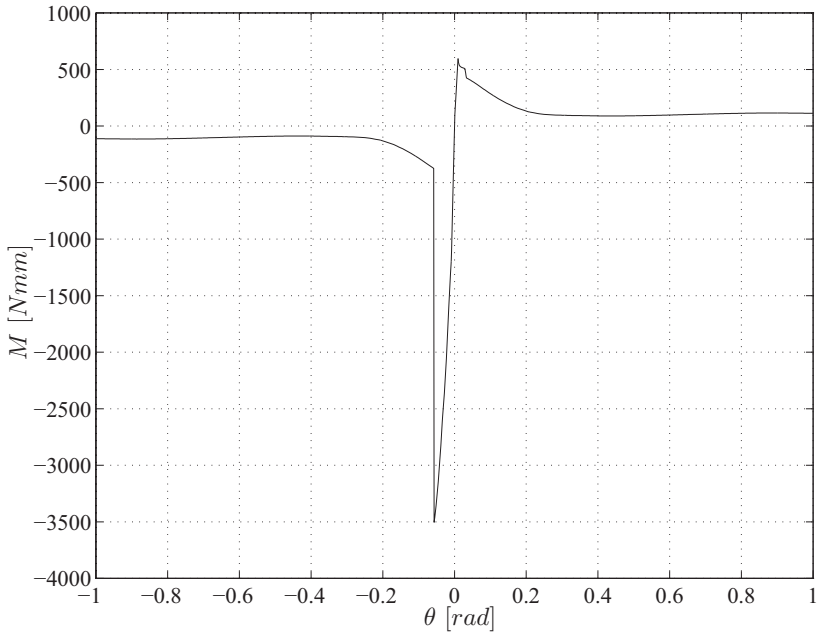

Figure 5.7: Moment-rotation relationship of composite tape-spring hinges by finite-element analysis.

is $-0.074\ rad$ ($-4.23°$). In both simulations the suspension system rotation is practically equal to the panel rotation, both before initial lock-out and after.

The finite-element data gives rise to larger steady-state moments for the composite tape-spring hinges and, hence, the deploying torque is greater and the panel deploys in a shorter time. Also, from Fig. 5.7, the largest deployment angle that the panel can reach without overshooting is $-0.056\ rad$. Figure 5.6 indicates a maximum deployment angle of $-0.077\ rad$ by the measured response for successful lock-out. From Fig. 5.8, both simulations yield smaller lock-out rotations, respectively, for $\theta_0 = 45°$; thus, the panel does not overshoot, and the values of θ_0^{max} obtained by the equal-areas calculation are confirmed. Since dissipative effects have not been included, the amplitude of free vibrations is constant and equal to the initial value of lock-out rotation.

The discrepancy between the predicted values of the post lock-out vibration period and the measured value of 1.9 s, Fig. 5.1(b), can be explained as follows.

The natural frequency of vibration of the panel after lock-out can also be estimated simply by modelling the system as a single degree-of-freedom system. The panel and tape-springs are modelled as a rigid element of length $L+a_p$, equal to the distance from the base of the tape-springs to the centroid of the panel. The moment of inertia of the panel about the base of the tape-springs I_b is thus

$$I_b = m_p(L + a_p)^2 + I_p \tag{5.37}$$

Substitution of m_p, L, a_p and I_p into Eq. 5.37 results in $I_b = 10.72\ kgm^2$.

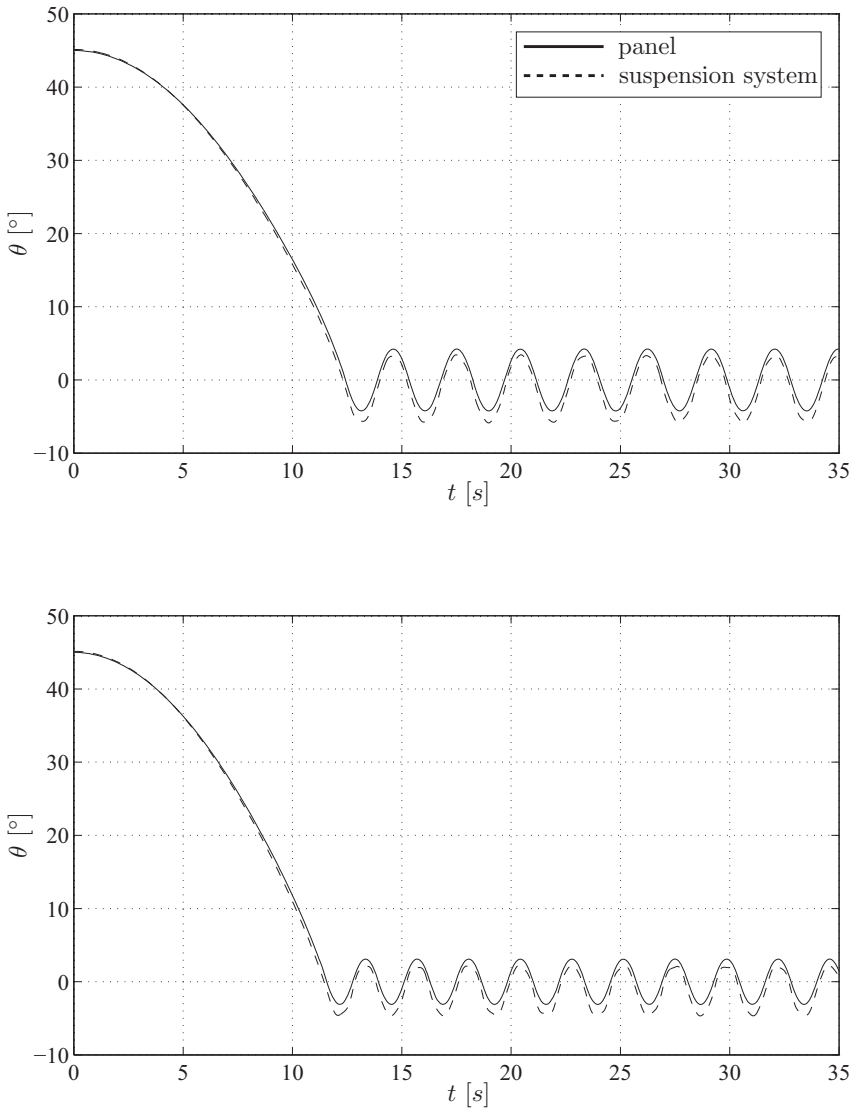

Figure 5.8: Predictions of panel deployment by first set of tape-springs: (a) experimental response and; (b) finite-element response.

The rotational stiffness of this system, k, is given by the initial slope of the relationships in Figs. 5.6 and 5.7, for $\theta < 0$. Hence, the equation of motion for vibration of the panel is

$$I_b\ddot{\theta} + k\theta = 0 \tag{5.38}$$

and the natural period of the panel is therefore

$$T = 2\pi\sqrt{\frac{I_b}{k}} \tag{5.39}$$

It has been noted that the predicted amplitude of oscillation is equal to the maximum rotation of the tape-springs without overshoot. For the finite-element composite response of Fig. 5.7, the initial gradient is approximately 66.9 Nm/rad. The period of vibration, from Eq. 5.39, is 2.52 s. However, closer inspection of Fig. 5.7 shows a bi-linear response, with higher stiffness equal to 119.7 Nm/rad up to a rotation of 0.01 rad. This results in a modified period of 1.88 s for a smaller amplitude of oscillation. This would seem consistent with a decreasing amplitude of oscillation due to dissipative effects during the deployment experiment, see Fig. 5.1(b). The initial value of k, from Fig. 5.6, is 76.1 Nm/rad for the measured moment response and the period of vibration of the panel is therefore 2.36 s. Thus, a more accurate period is obtained using the finite-element response. However, as noted in Section 5.1, the initial stiffness of the measured response may be larger due to the compliance of the bending apparatus, and, hence the calculated value of period would decrease.

Material damping in the tape-springs causes the amplitude of post lock-out vibration to slowly decrease. It is due to hysteresis effects in the CuBe and also to a lack of fixity between the CuBe, the tape-spring end-blocks and the panel/scaffold interfaces. An estimate of the degree of damping can be obtained by inclusion of a rotational damping term into Eq. 5.38, *i.e.*

$$I_b\ddot{\theta} + c\dot{\theta} + k\theta = 0 \tag{5.40}$$

where c is of units Nms. A value of c can be found, provided the time, t', is known for which the initial amplitude of vibration decays by a particular percentage p'. Let the natural frequency of vibration of the panel be $w_n = \sqrt{k/I_b}$, and the damping factor is c', equal to $cw_n/2k$. Therefore, solving Eq. 5.40 yields

$$c' = -\frac{1}{w_n t'} \log\left[\frac{1-p'}{\cos w_n t'}\right] \tag{5.41}$$

Choosing a value of $1-p'$ equal to 0.01 and substitution of the values of frequency and time of decay from Table 5.3 into Eq. 5.41 results in values of c' of 0.0024 and 0.0039 for the experiments without and with overshoot, respectively. Plastic deformation of the tape-springs during overshoot causes c' to increase.

5.4 Discussion

Consider Fig. 5.9. In this plot, the deployment of the panel by the first set of tape-springs is shown for $m_j = 0$, $I_j = 0$, $m_w = 0$, and $I_w = 0$ substituted into

Eqs. 5.26 and 5.33, with $Q_\theta = 0$ and $Q_\beta = 0$. Therefore, Eq. 5.33 has zero on both sides and gravitational terms in Eq. 5.26 become zero. Thus, this prediction corresponds to simulated deployment of the panel in space.

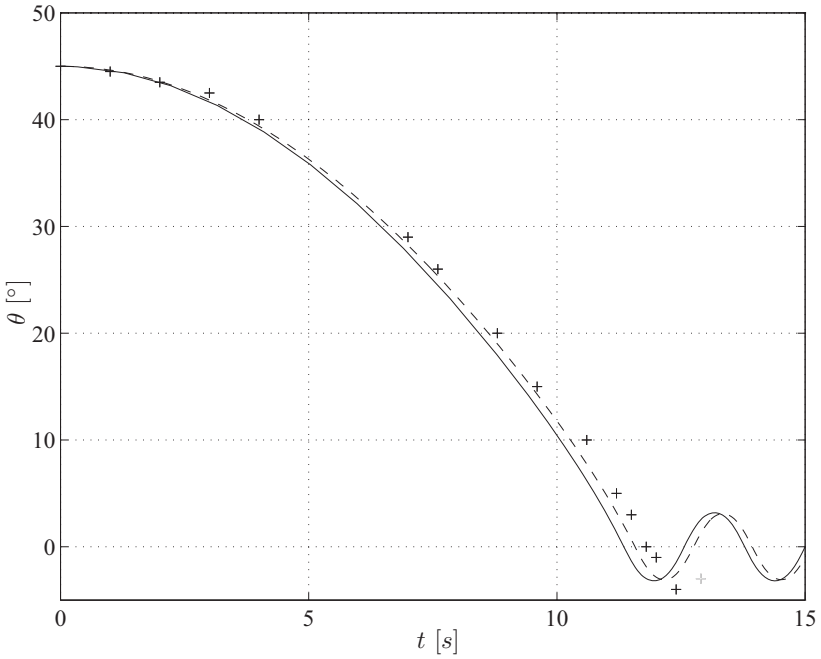

Figure 5.9: Comparison between measured deployment of panel ("+"), predicted deployment behaviour with suspension system (dashed line) and predicted deployment behaviour without suspension system and gravity (continuous line).

Also, shown are the predicted deployment from Fig. 5.8(b) and the measured response before first lock-out from Fig. 5.1(a). There are two points to note. First, the initial deployment is practically the same for all curves, the zero-gravity deployment is slightly faster since there is no suspension system inertia. Second, the period and amplitude of post lock-out vibration from both predictions are also practically identical. Thus, the experimental set-up and the corresponding analytical model accurately simulate and predict gravity-free deployment, respectively.

Chapter 6

Design of Rigid Panel Deployment System

In this chapter, a series of of formulae are derived which may be used to estimate the type and number of composite hinges required for a desired "deployment performance" of a panel of known dimensions, mass and inertia properties. The bending behaviour of the tape-springs that make up a composite hinge will be described by in terms of the key features of the moment-rotation relationship obtained in Section 2.3. In this way, R, t, L, α, and the material properties of tape-springs enter directly into the analysis as variable design parameters.

Deployment performance can be described by three parameters. The first parameter is the time t' that it takes for the panel to reach first lock-out from rest; this deployment time is related to the deploying torque required. The second parameter is the frequency of vibration f_n of the panel after lock-out has been achieved. If this frequency is close to the spacecraft natural frequency there may be coupling between the overall spacecraft dynamics and the vibration of the panel, which may be difficult to correct in the absence of damping. The third parameter is the maximum angle of folding, θ_0^{max}, that can be attained by the composite hinges without snap-through occurring during rebound. Overshoots are undesirable because they may cause damage at the edge of the panel, which may result in the clearance tolerances being exceeded in the fully deployed state. The value of θ_0^{max} dictates the stowed configuration of the panel before launch.

At all stages during deployment the tape-springs must remain elastic. Plasticity in the tape-springs may lead to incorrect deployment and might also reduce the fatigue life of the hinges.

In Section 6.1, an approximate expression for the maximum deployment angle of a composite hinge is derived. Section 6.2 deals with the time for deployment and the natural frequency of vibration of the panel. Tape-spring plasticity is examined in Section 6.3. The design formulae are then tested by worked examples in Section 6.4. Finally, Section 6.5 discusses the procedure by which the composite

hinge geometry may be determined in practice.

6.1 Idealisation of Composite Hinge Behaviour

The behaviour of a composite hinge can be simplified as follows. Figure 6.1 shows the moment-rotation relationships of the two tape-springs comprising a composite hinge. The initial folded angle, θ_0, is positive, Section 3.2, and each curve is an idealisation based on Fig. 1.3. The notation for key moment and rotation features has been defined in Chapters 1 and 2.

Unloading of the tape-spring initially folded in the equal-sense direction is shown in Fig. 6.1(a). Initial behaviour is characterised by the line $M = |M_-^*|$; it is assumed, Section 2.2, that the bending moment remains constant until the rotation becomes equal to $|\theta_-^{ramp}|$. Then, as θ decreases further, the moment ramps up to $|M_-^{max}|$ following a straight line. The corresponding rotation is $|\theta_-^{max}|$. Thereafter, the behaviour is linear as the tape-spring passes through the zero angle position. For initial opposite-sense bending of the spring the M, θ relationship follows a straight line of the same slope until peak values of moment and rotation, $-M_+^{max}$ and $-\theta_+^{max}$, respectively. Beyond $-\theta_+^{max}$ the tape-spring snaps through, and this part of the response is indicated by a long-dashed line.

The moment-rotation response for an identical tape-spring initially folded in the opposite sense is shown in Fig. 6.1(b). The tape unloads from θ_0 along the line $M = M_+^*$, and at θ_+^{heel} snaps back to a bending moment M_+^{heel} on the linear portion of the pre-buckled curve. During rebound, the equal-sense bending behaviour is the same as that in Fig. 6.1(a), but with moment and rotation of opposite signs.

The composite hinge does not overshoot if, Section 3.2, the combined area below both curves, from θ_0 to $\theta = 0$, which corresponds to the energy available for deployment, is less than or equal to the magnitude of the area above the curves from $\theta = 0$ to $\theta = -\theta_+^{max}$, *i.e.* the maximum amount of energy that can be absorbed elastically without snap-through.

The respective areas are calculated as follows. The area under the two curves for positive θ, A_1, is obtained by a summation of the elementary areas bounded by the construction lines, *i.e.*

$$\begin{aligned} A_1 &= |M_-^*|\left(\theta_0 - |\theta_-^{ramp}|\right) + \frac{1}{2}M_-^{max}\theta_-^{max} \\ &\quad + A_u + M_+^*\left(\theta_0 - \theta_+^{heel}\right) + \frac{1}{2}M_+^{heel}\theta_+^{heel} \end{aligned} \tag{6.1}$$

where A_u is the area underneath the ramp line from $|\theta_-^{max}|$ to $|\theta_-^{ramp}|$. If $\theta_+^{heel} < 0$, then the tape-spring snaps back onto the linear curve at M_+^* and, thus, the last term in the above equation will become approximately zero. The combined area

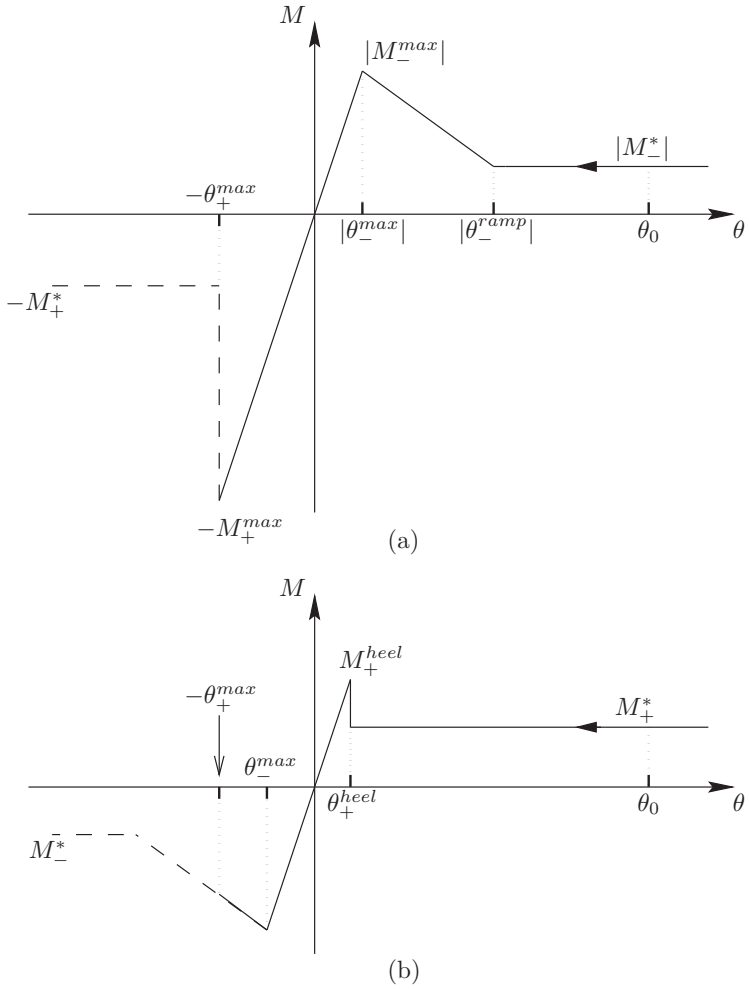

Figure 6.1: Idealisation of composite hinge behaviour using moment-rotation relationships of component tape-springs: (a) equal-sense bending; (b) opposite-sense bending. Construction lines, for the calculation of areas, are shown as dotted lines. Long dashed lines indicate the route followed during overshoot.

with respect to rebound, A_2, is given by

$$A_2 = \frac{1}{2}M_+^{max}\theta_+^{max} + \frac{1}{2}M_-^{max}\theta_-^{max} + A_l \tag{6.2}$$

A_l is the size of the area above the ramp line between $\theta = -|\theta_-^{max}|$ and $\theta = -\theta_+^{max}$. Note that for $\theta_+^{max} \geq |\theta_-^{ramp}|$, $A_l = A_u$. Equating A_1 to A_2 for $\theta_0 = \theta_0^{max}$ and

rearranging terms results in

$$\begin{aligned}\left(M_+^* + |M_-^*|\right)\theta_0^{max} &= A_l - A_u + \frac{1}{2}M_+^{max}\theta_+^{max} + M_-^*\theta_-^{ramp} \\ &\quad + \left[-\frac{1}{2}M_+^{heel} + M_+^*\right]\theta_+^{heel} \end{aligned} \tag{6.3}$$

$A_l - A_u$ will now be calculated. The equation of the ramp line in Fig. 6.1(a) is given by

$$M = |M_-^*| + K\left(\theta - |\theta_-^{ramp}|\right) \tag{6.4}$$

where

$$K = \frac{|M_-^{max}| - |M_-^*|}{|\theta_-^{max}| - |\theta_-^{ramp}|} \tag{6.5}$$

Therefore

$$A_u = \int_{\theta=|\theta_-^{max}|}^{\theta=|\theta_-^{ramp}|} M d\theta \tag{6.6}$$

By symmetry, the equivalent expression for A_l is given by

$$A_l = \int_{\theta=|\theta_-^{max}|}^{\theta=\theta_+^{max}} M d\theta \tag{6.7}$$

Thus

$$A_l - A_u = \int_{|\theta_-^{ramp}|}^{\theta_+^{max}} \left[|M_-^*| + K\left(\theta - |\theta_-^{ramp}|\right)\right] d\theta \tag{6.8}$$

Substitution of Eq. 6.5 into Eq. 6.8 and performing the integration yields

$$A_l - A_u = \frac{1}{2}\frac{|M_-^{max}| - |M_-^*|}{|\theta_-^{max}| - |\theta_-^{ramp}|}\left(\theta_+^{max} - |\theta_-^{ramp}|\right)^2 + |M_-^*|\left(\theta_+^{max} - |\theta_-^{ramp}|\right) \tag{6.9}$$

Replacing $A_l - A_u$ in Eq. 6.3 with Eq. 6.9, the symbolic expression for the maximum deployment angle becomes

$$\begin{aligned}\left(M_+^* + |M_-^*|\right)\theta_0^{max} &= \left[\frac{1}{2}M_+^{max} + |M_-^*|\right]\theta_+^{max} + \left[-\frac{1}{2}M_+^{heel} + M_+^*\right]\theta_+^{heel} \\ &\quad + \frac{1}{2}\frac{|M_-^{max}| - |M_-^*|}{|\theta_-^{max}| - |\theta_-^{ramp}|}\left(\theta_+^{max} - |\theta_-^{ramp}|\right)^2 \end{aligned} \tag{6.10}$$

for $\theta_+^{max} < |\theta_-^{ramp}|$ and $\theta_+^{heel} \geq 0$. Expressions for $|\theta_-^{max}|$ and M_+^{heel} can be obtained by noting that the initial slope of the moment-rotation curve is assumed to be the same for either bending sense. Thus

$$|\theta_-^{max}| = \frac{|M_-^{max}|}{M_+^{max}}\theta_+^{max} \tag{6.11}$$

$$M_+^{heel} = \frac{M_+^{max}}{\theta_+^{max}} \theta_+^{heel} \tag{6.12}$$

The corresponding expressions for M_+^{max}, θ_+^{max}, θ_+^{heel}, $|M_-^{max}|$, $|\theta_-^{ramp}|$, M_+^* and $|M_-^*|$ are given by Eqs. 2.32, 2.33, 2.34, 2.35, 2.36, 2.37 and 2.38, respectively.

A final point concerns the approximations of the functions in Fig. 6.1 when describing real tape-spring behaviour. When the behaviour of tape-springs under opposite-sense bending shows a large non-linearity before snap-through, especially in long and shallow tape-springs, Figs. A.1 - A.4, the $1/2 M_+^{max} \theta_+^{max}$ term in Eq. 6.2 becomes an under-estimation of the actual area underneath the curve up until the end of the nose. This term predominates above all others in Eq. 6.2 in respect of the capacity of the composite hinge to absorb kinetic energy. Therefore, θ_0^{max} will be under-estimated, assuming the other functions to be accurate.

6.2 Deployment Time and Natural Frequency

An estimate of the time it takes for the panel to deploy until first lock-out is obtained as follows.

The kinetic energy of the panel is given by Eq. 5.7. To simplify the equations of motion, the arc-length of the fold is neglected in comparison with the overall dimensions of the panel. Thus, omitting the term $R\theta$ from Eq. 5.7 gives

$$T = \frac{1}{2} m_p [L - p_1 + a_p]^2 \dot{\theta}^2 + \frac{1}{2} I_p \dot{\theta}^2 \tag{6.13}$$

The strain energy stored in the system during deployment, is approximately given by the strain-energy stored in the folds of post-buckled tape-springs, Eqs. 2.37 and 2.38 respectively multiplied by θ. For n pairs of composite hinges

$$V = n[D(1+\nu)\alpha\theta + D(1-\nu)\alpha\theta] = 2nD\alpha\theta \tag{6.14}$$

The Lagrangian is therefore given by

$$\mathcal{L} = \frac{1}{2} m_p \left(L - p_1 + a_p\right)^2 \dot{\theta}^2 + \frac{1}{2} I_p \dot{\theta}^2 - 2nD\alpha\theta \tag{6.15}$$

Differentiating Eq. 6.15 with respect to θ, and also to $\dot{\theta}$ and then t, and then substituting into Eq. 5.16 results in the following governing equation of motion

$$\left[m_p \left(L - p_1 + a_p\right)^2 + I_p\right] \ddot{\theta} + 2nD\alpha = 0 \tag{6.16}$$

Equation 6.16 can be integrated twice with respect to time, with initial conditions $\dot{\theta} = 0$ and $\theta = \theta_0^{max}$ at time $t = 0$. Substituting for $\theta = 0$ into the resulting

expression in θ yields the time for deployment, t',

$$t' = \sqrt{\frac{[m_p(L - p_1 + a_p)^2 + I_p]\,\theta_0^{max}}{nD\alpha}} \tag{6.17}$$

The frequency of post lock-out vibration, f_n, is obtained by inverting Eq. 5.39. The stiffness term in this equation is replaced by an equivalent term for n pairs of composite hinges. This term is equal to the initial slope of both relationships in Fig. 6.1 added together, *i.e.* $2M_+^{max}/\theta_+^{max}$. Therefore

$$f_n = \frac{1}{2\pi}\sqrt{\frac{2nM_+^{max}}{[m_p(L + a_p)^2 + I_p]\theta_+^{max}}} \tag{6.18}$$

For an amplitude of oscillation greater than $|\theta_-^{max}|$, the rotational stiffness becomes non-linear, and the governing equation of motion changes. Hence, Eq. 6.18 is only valid for small oscillations.

6.3 Yield Limits

Tape-springs may deform plastically if the bending stresses exceed the yield stress of CuBe. High bending stresses occur either when a large bending moment is applied to the tape-spring during rebound of the panel in the tape-spring of Fig. 6.1(b), or when large changes of curvature are imposed to the folded tape-springs. The relevant expressions for both limit states are obtained as follows.

The maximum bending moment that can be applied to the straightened out tape-spring is M_+^{max}, the associated stress can be estimated using simple, linear beam theory. It is assumed that the cross-section does not deform in the transverse direction, *i.e.* the degree of flattening of the section is neglected. This, of course, produces an over-estimate of the actual bending stresses in the tape-spring. The "extreme-fibre" stresses in the tape-spring are therefore given by

$$\sigma_{1,2} = -\frac{M_+^{max} d_{1,2}}{I} \tag{6.19}$$

where $d_{1,2}$ are the distances between the neutral axis and points at a maximum distance above and below it, respectively, see Fig. 6.2. I is the second moment of area. By simple geometry

$$I = \frac{R^3 t}{2\alpha}\left[\alpha^2 - 4\,(1 - \cos\alpha) + \alpha\sin\alpha\right] \tag{6.20}$$

and

$$d_1 = \frac{R}{\alpha}\left[\alpha - 2\sin\frac{\alpha}{2}\right] \tag{6.21}$$

$$d_2 = -\frac{R}{\alpha}\left[2\sin\frac{\alpha}{2} - \alpha\cos\frac{\alpha}{2}\right] \tag{6.22}$$

For any value of α, $|d_2|$ is always greater than d_1 and, hence, the tensile stresses along the tape-spring edges are greatest. Assuming all other principal stresses to be zero, the limiting elastic moment, M_+^{cr}, is given by

$$M_+^{cr} = \sigma_y R^2 t \frac{[\alpha^2 - 4(1-\cos\alpha) + \alpha\sin\alpha]}{2\left(2\sin\frac{\alpha}{2} - \alpha\cos\frac{\alpha}{2}\right)} \tag{6.23}$$

where σ_y is the yield stress of the material. It cannot be discounted, however, that local buckling may occur at point 1, or indeed, anywhere within the compressive region above the neutral bending axis well before plasticity takes effect, especially if the tape-spring is thin. This is beyond the scope of the present study and is discussed no further.

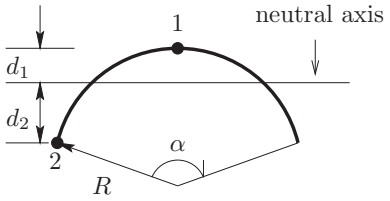

Figure 6.2: Points of maximum stress on tape-spring cross-section at M_+^{max}.

The maximum bending stresses in the fold are now obtained. From Calladine (1983), the in-plane transverse and longitudinal bending stresses, σ_t and σ_l, respectively, are given by

$$\begin{aligned} \sigma_t &= \frac{E}{(1-\nu^2)} u(\kappa_t + \nu\kappa_l), \\ \sigma_l &= \frac{E}{(1-\nu^2)} u(\kappa_l + \nu\kappa_t) \end{aligned} \tag{6.24}$$

where u is now the out-of-plane distance with respect to the central surface of the fold. The terms in Eq. 6.24 are also principal stresses, and their maximum values will be reached on the either surface of the fold, *i.e.*, when $u = \pm t/2$; the through-thickness stress is assumed to be zero.

From the Tresca yield criterion, the maximum difference between the principal stresses occurs for equal-sense bending, that is when $\kappa_l = -1/R$ and $\kappa_t = 1/R$, and is equal to σ_y. Thus

$$\frac{R}{t} \geq \frac{E}{\sigma_y(1+\nu)} \tag{6.25}$$

Substituting for the values of E, σ_y and ν from Table 1.1 into Eq. 6.25 requires $R/t \geq 85.6$ for elastic behaviour.

6.4 Examples

This section verifies the accuracy of the above design criteria by applying them to the system tested in Section 5.1.

Consider the two sets of composite hinges that deployed the panel without overshoot in Section 5.1. Individual tape-spring geometries are given in Table 5.1. Tables 6.1 and 6.2 list computed values of the key moment and rotation parameters, respectively, for a tape-spring from each set. Recall that for both sets of tape-springs $n = 2$.

tape-set	M_+^{max} $[Nmm]$ Eq. 2.32	$\lvert M_-^{max}\rvert$ $[Nmm]$ Eq. 2.35	M_+^{*} $[Nmm]$ Eq. 2.37	$\lvert M_-^{*}\rvert$ $[Nmm]$ Eq. 2.38	M_+^{heel} $[Nmm]$ Eq. 6.12
1	1583.1	312.6	28.1	15.2	373.0
2	3253.9	539.6	39.4	21.2	155.7

Table 6.1: Key moment values for both sets of tape-springs in Section 5.1.

tape-set	θ_+^{max} $[^\circ]$ Eq. 2.33	$\lvert\theta_-^{max}\rvert$ $[^\circ]$ Eq. 6.11	θ_+^{heel} $[^\circ]$ Eq. 2.34	$\lvert\theta_-^{ramp}\rvert$ $[^\circ]$ Eq. 2.36
1	4.985	0.974	1.203	16.616
2	6.876	1.146	0.327	23.090

Table 6.2: Key rotation values for both sets of tape-springs in Section 5.1.

Note that the computed parameters in the above tables, for the first set of tape-springs, are in good agreement with Fig. 5.2.

Table 6.3 compares the computed deployment behaviour of the panel, by substituting the values from Tables 6.1 and 6.2 into the relevant design formula, to the actual behaviour. Included in this table are the measured deployment results from Section 5.1 and the values of θ_0^{max} obtained from the equal-areas (E.A.) condition applied to the finite-element data, Section 5.3.

tape-set	θ_0^{max} $[^\circ]$ expt	θ_0^{max} $[^\circ]$ Eq. 6.10	θ_0^{max} $[^\circ]$ (E.A.)	t' $[s]$ expt	t' $[s]$ Eq. 6.17	f_n $[Hz]$ expt	f_n $[Hz]$ Eq. 6.18
1	45	58	51	12.0	13.1	0.526	0.414
2	138	135	143	15.5	19.4	0.62	0.505

Table 6.3: Comparison of measured deployment behaviour and predictions from design formulae.

In general, there is good agreement between the values of θ_0^{max}, despite the approximation of Eq. 6.10. Equation 6.18 tends to under-estimate the natural frequency of the panel after lock-out by about 10%. A possible reason may be that either M_+^{max} is too small, or θ_+^{max} is too large. Inspection of Fig. 2.12 suggests that, indeed, values of θ_+^{max} from Eq. 2.33 are larger than values from finite element analyses, for lengths of spring less than $8R\alpha$. The computed value of t', for the second set of tape-springs, is some 20% greater than the measured value. The approximation of the deploying torque of the composite hinge is too large. This may be due to the rigidly encased ends interacting with the steady-state folds. The result would be to cause a smaller radius of longitudinal curvature in the fold, resulting in a larger deploying torque from Eq. 2.29. Table 6.4 summarises the yield performance.

tape-set	M_+^{cr} $[Nmm]$ Eq. 6.23	$M_+^{max} \leq M_+^{cr}$	R/t	elastic fold? Eq. 6.25
1	8781	yes	281	yes
2	12504	yes	206	yes

Table 6.4: Material performance of both sets of tape-springs at extremities of deployment.

Overall, the design formulae correlate with the measured behaviour within approximately 15%.

6.5 Design Procedure

The analysis of the previous sections has yielded a total of 22 parameters: m_p, I_p, a_p, L, R, α, t, p_1, n, M_+^{max}, θ_+^{max}, θ_+^{heel}, M_-^{max}, θ_-^{ramp}, M_+^*, M_-^*, θ_0^{max}, t', f_n, E, ν and σ_y.

The values of the seven moment and rotation terms, are functions of —at most— L, R, α, t, E and ν. From the previous examples, it can be assumed that $p_1 = 1/3L$. The values of E, ν and σ_y are unique to the material chosen for the tape-springs. Therefore, the number of unknowns decreases to 11. The mass and geometry of the panel (m_p, a_p and I_p) are dictated by the structural, material and functional properties of the panel and, hence, will be known.

The values of t', θ_0^{max} and f_n are governed by the deployment requirements for the panel, and will lie within particular bounds, but at any instant can assume particular values. For example, there may be a lower bound value for the deployment time so that large accelerations are not applied to fragile elements on the panel. Also, the natural frequency of panel vibration must be different from the spacecraft fundamental mode, and the maximum amplitude of oscillation, θ_+^{max}, is to be as small as possible to permit accurate performance of any sensing devices

on the panel. The stowed angle of the composite hinges is dictated by the design of the spacecraft.

The total number of unknowns now reduces to five; L, R, α, t, and the number of pairs of composite-hinges, n. Equations 6.10, 6.17, 6.18, 6.23 and 6.25 are the five constitutive design equations and, thus, can be solved by a numerical method to yield unique values of the five unknown parameters, subject to n being an integer.

Alternatively, the two equations pertaining to material performance could be used as "running" check on selection of a given tape-spring geometry. There are still the above five unknowns, but only three design equations. This therefore requires the values of two of the five unknowns to be declared, for example, n and L, which may be constrained to limiting bounds by the panel and spacecraft dimensions. Next, the design equations are solved to find R, t and α. The procedure can then be repeated many times by varying the declared variables until a "sensible" geometry is found.

The following example illustrates the above procedure. A panel has $m_p = 15\ kg$, $I_p = 5\ kgm^2$, and $a_p = 0.9\ m$. The tape-springs are made of CuBe and their material properties are given in Table 1.1. The number of composite hinges, n, is 3, and each hinge has a length of 250 mm. θ_0^{max} is chosen to equal 100°, t' and f_n have arbitrary values of 7.5 s and 0.7 Hz, respectively. Table 6.5 summarises the tape-spring properties that were computed by simultaneously solving the design equations with these deployment parameters. Furthermore, the tape-springs remain elastic at all times during deployment.

R $[mm]$	α [°]	t $[mm]$	L $[mm]$	R/t	M_+^{max} $[Nmm]$	M_+^{cr} $[Nmm]$
23.7	148.0	0.194	250	122.0	$1.308 \cdot 10^4$	$3.442 \cdot 10^4$

Table 6.5: Example tape-spring properties obtained using design equations.

Chapter 7

Conclusions

The generic bending behaviour of tape-springs has been presented. This behaviour results in a fold —a localised, elastic region of uniform curvature— either by the tape-spring snapping through, or by a gradual flattening of the central section, depending on the direction of bending. This has been confirmed by experiments and by a finite-element analysis.

The bending response of relatively short tape-springs with their ends encased in solid blocks has been determined by finite-element analysis for a wide range of section geometries. It has been shown that tape-springs with the same cross-section, but different lengths, have many common moment-rotation properties; thereby reducing the amount of computation needed to produce equivalent relationships. Expressions characterising key features of the moment-rotation relationship in terms of geometric and material parameters have been obtained.

The deployment of a rigid element attached to the free end of a rigidly mounted tape-spring, initially folded in the equal-sense direction, has been presented. The behaviour has been described by an interchange of kinetic energy of the element and elastic strain energy stored in the spring. The steady-state propagation moment of the fold deploys the element to an almost straight configuration; the high peak moment prevents overshoot.

It has been demonstrated that the combined moment response of two identical tape-springs mounted in parallel, and with their centres of curvature on opposite sides, results in an energy well corresponding to the fully deployed configuration of an attached rigid element. It has been shown that if the kinetic energy accumulated by the rigid element during deployment from the folded state is less than the energy to come out of the well, the element does not overshoot its intended deployed configuration. It then vibrates according to the stiffness of the composite hinge locking moment.

A rigid element has been designed and built in the form of a triangular panel whose mass and inertia properties are representative of panels used on spacecraft, and has been deployed without overshoot by composite hinges fixed to a rig that

compensates for the effects of gravity. A two dimensional, analytical model has been derived that takes account of dynamic coupling between the panel and suspension. This model has verified the computed maximum deployment angle of composite hinges, and also, the effectiveness of the suspension.

The first steps towards a design philosophy for composite hinges have been made by deriving expressions for the key parameters that determine the panel deployment. An example has demonstrated that the determination of an appropriate composite hinge geometry can be automated.

In terms of further work, there are many paths to follow. First, Seffen (1997) has shown that a fold begins to interact with a single, rigid support at a distance $\approx 1.5R\alpha^2$ from the support, at which point the deformation within the fold becomes asymmetric. It cannot be discounted that bending of short tape-springs produces simultaneous interaction on both sides of the fold with the encased ends. Indeed, for a fold of infinitesimal length, it may be suggested that if $L \leq 3R\alpha^2$ then such an interaction will occur. This will, of course, produce a longitudinal radius of curvature greater than R everywhere in the fold and, hence, the deploying torque of the tape-spring will increase. The implications of this are that the energy available for deployment of a panel increases and, therefore, the maximum angle of deployment, θ_0^{max}, calculated from Eq. 6.10, decreases.

It is also expected that if the mass of deploying panel is small, the folds in the composite hinges may not remain at a fixed position during deployment. Seffen (1997) has shown that the self-deployment process of a folded tape-spring with no attached tip mass results in rapid propagation of the fold between its equilibrium configuration before deployment and the fixed base, as the tape becomes straight. Thus, the dynamics of a light-weight panel system become more complex and to simulate this, an analytical model is needed that combines the moment-rotation properties of composite hinges with the travelling fold mechanics of singly-folded tape-springs in Chapter 6 of Seffen (1997).

Finally, the design procedure of Section 6.5 needs to be refined numerically in order to provide a reliable and viable design tool.

Bibliography

Calladine, C.R. (1983), *Theory of Shell Structures*, Cambridge University Press.

Calladine, C.R. (1988), The theory of thin shell structures 1888-1988, *Proc. Inst. Mech. Eng* **202**, 1–9.

Crisfield, M.A. (1991), *Non-Linear Finite Element Analysis of Solids and Structures. Volume 1: Essentials.*, John Wiley & Sons, Chichester.

Fischer, A. (1995), Bending instabilities of thin-walled transversely curved metallic strips, Technical Report CUED/D-STRUCT/TR 154, Cambridge University Engineering Department.

Hibbit, Karlsson and Sorenson (1994), *ABAQUS Version 5.4*, Hibbit, Karlsson & Sorenson Ltd, Pawtucket.

Mansfield, E.H. (1973), Large-deflexion torsion and flexure of initially curved strips, *Proc. Roy. Soc. London A* **334**, 279–298.

Mathworks (1995), *MATLAB Version 4.2*, The Mathworks Inc., Natick.

Riks, E. (1972), The application of Newton's method to the problem of elastic stability, *J. Appl. Mech* **39**, 1060–1066.

Rimrott, F.P.J. (1966*a*), Storable tubular extendible members, *Engineering Digest* .

Rimrott, F.P.J. (1966*b*), Two secondary effects in bending of slit thin-walled tubes, *J. Appl. Mech.* .

Rimrott, F.P.J. (1970), Querschnittsverformung bei torsion offnerer profile, *Zeitschrift für angewandte Mathematik und Mechanik* **50**, 775–778.

Rimrott, F.P.J. (1980), Self-extension of an open-section tube, *in* 'Theory of Shells', North-Holland Publishing Co., pp. 495–508.

Seffen, K.A. (1997), Analysis of Structures Deployed by Tape-Springs, PhD thesis, Cambridge University.

Synge, J.L. and Griffith, B.A. (1970), *Principles of Mechanics*, third edn, M^{c}Graw-Hill, Singapore.

Tan, G.E.B. and Pellegrino, S. (1996), Non-linear dynamic identification: An application to prestressed cable systems, *in* B.Augusti and Spinelli, eds, 'Structural Dynamics - EURODYN'96'.

Wüst, W. (1954), Einige anvendungen der theorie der zylinderschale, *Z. angew. Math. Mech* **34**, 444–454.

Appendix A

Results from Finite-Element Analysis

This appendix presents additional results from finite-element analysis. Plots of dimensionless moment-curvature relationships are shown in Figs. A.1 - A.4. These are for opposite-sense bending only and extend as far as the nose of the curve. For a section thickness of 0.1 mm, plots have been obtained for five different subtended angles of cross-section; 90° to 170° in steps of 20°. For $t = 0.2$ mm and $t = 0.3$ mm, the plots have been constructed for $\alpha = 90°$, 130° and 170°, respectively. The number inside the circle close to the nose of each plot refers to the length of the tape-spring $\times R\alpha$.

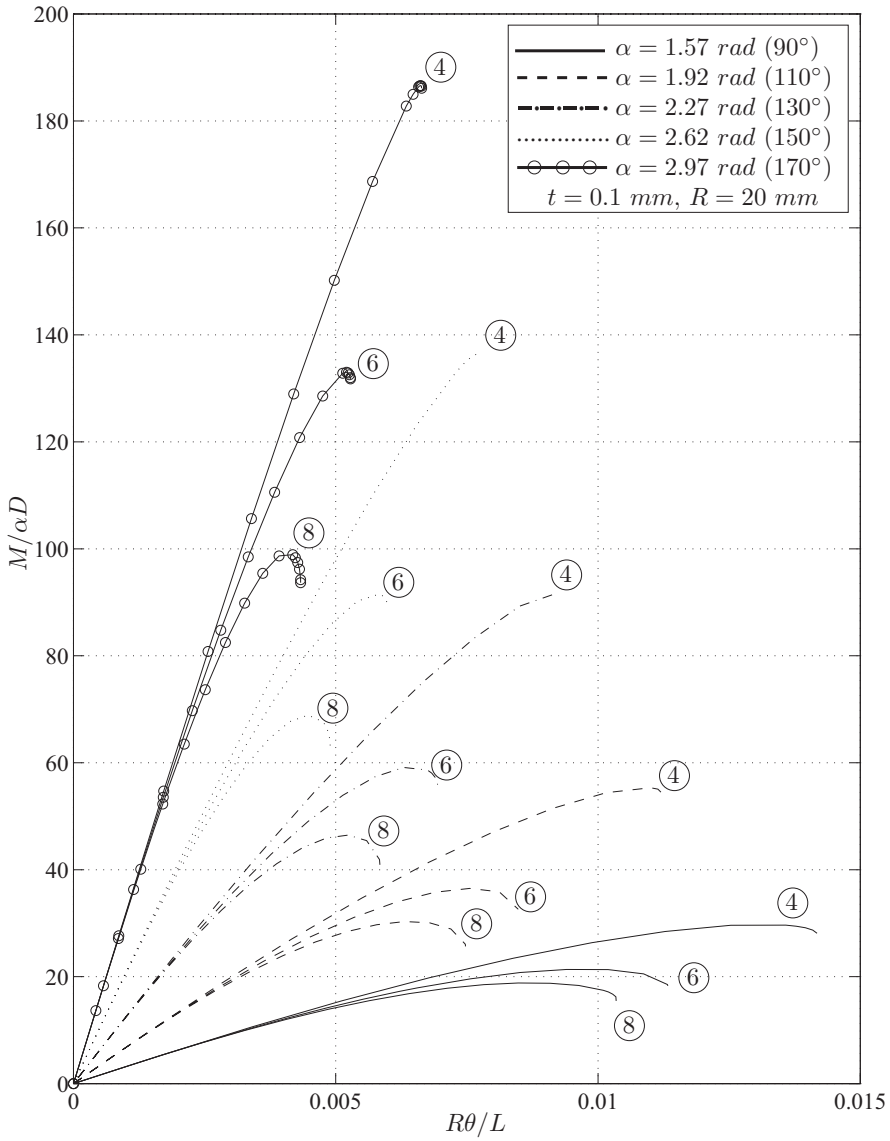

Figure A.1: Dimensionless opposite-sense bending behaviour, before buckling, for $R = 20\ mm$ and $t = 0.1\ mm$.

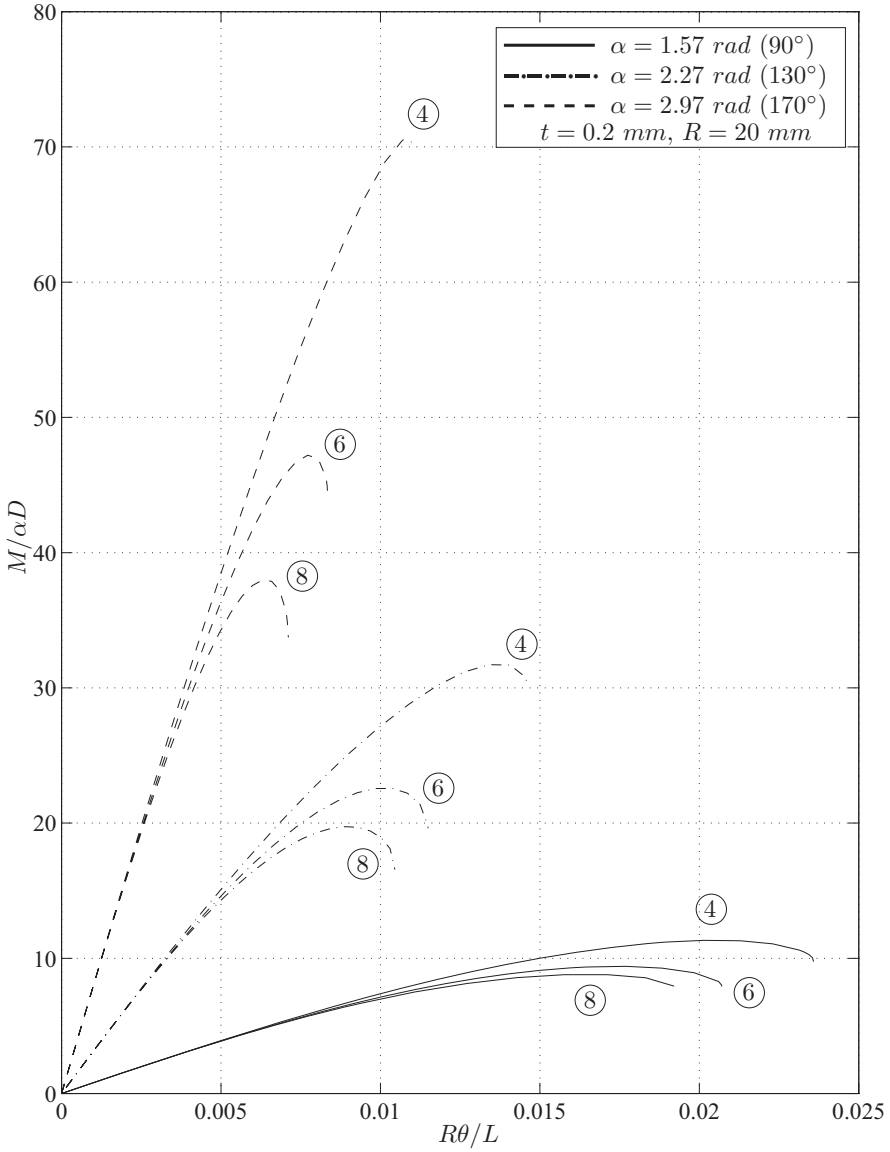

Figure A.2: Dimensionless opposite-sense bending behaviour, before buckling, for $R = 20\ mm$ and $t = 0.2\ mm$.

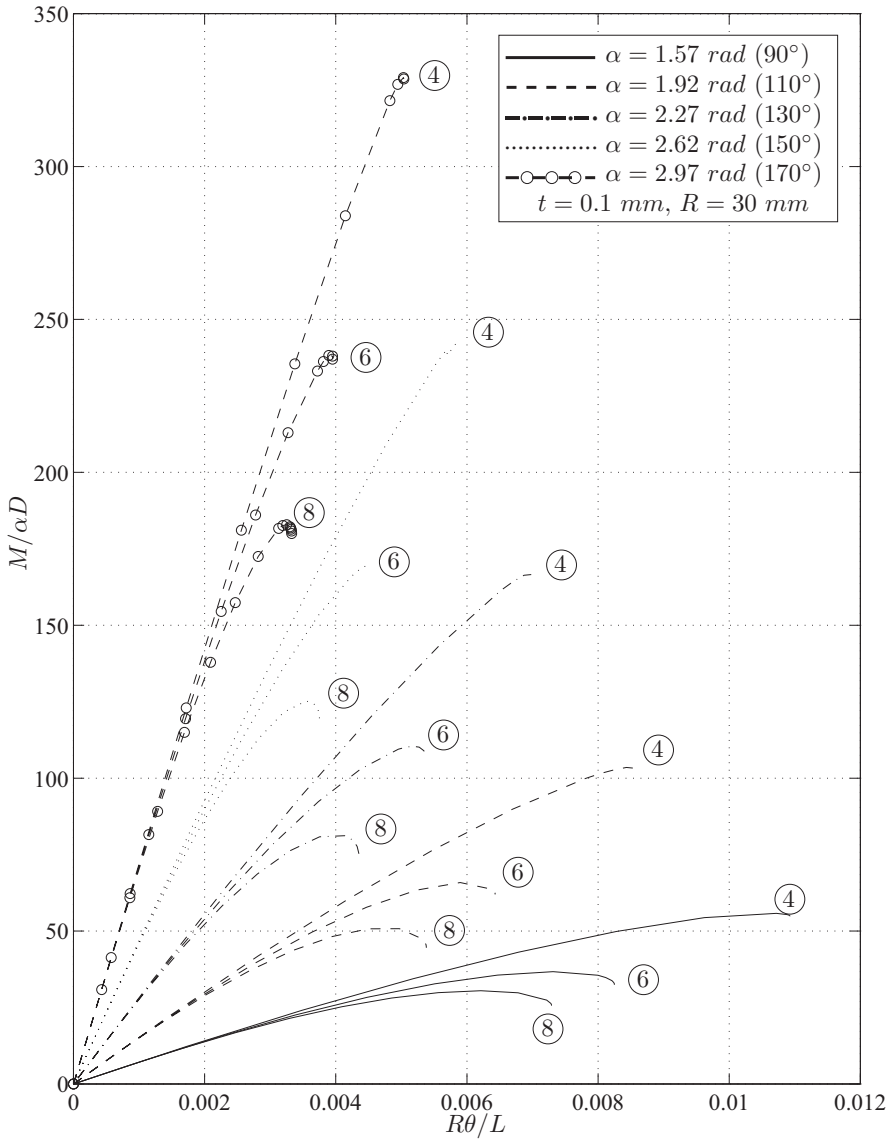

Figure A.3: Dimensionless opposite-sense bending behaviour, before buckling, for $R = 30\ mm$ and $t = 0.1\ mm$.

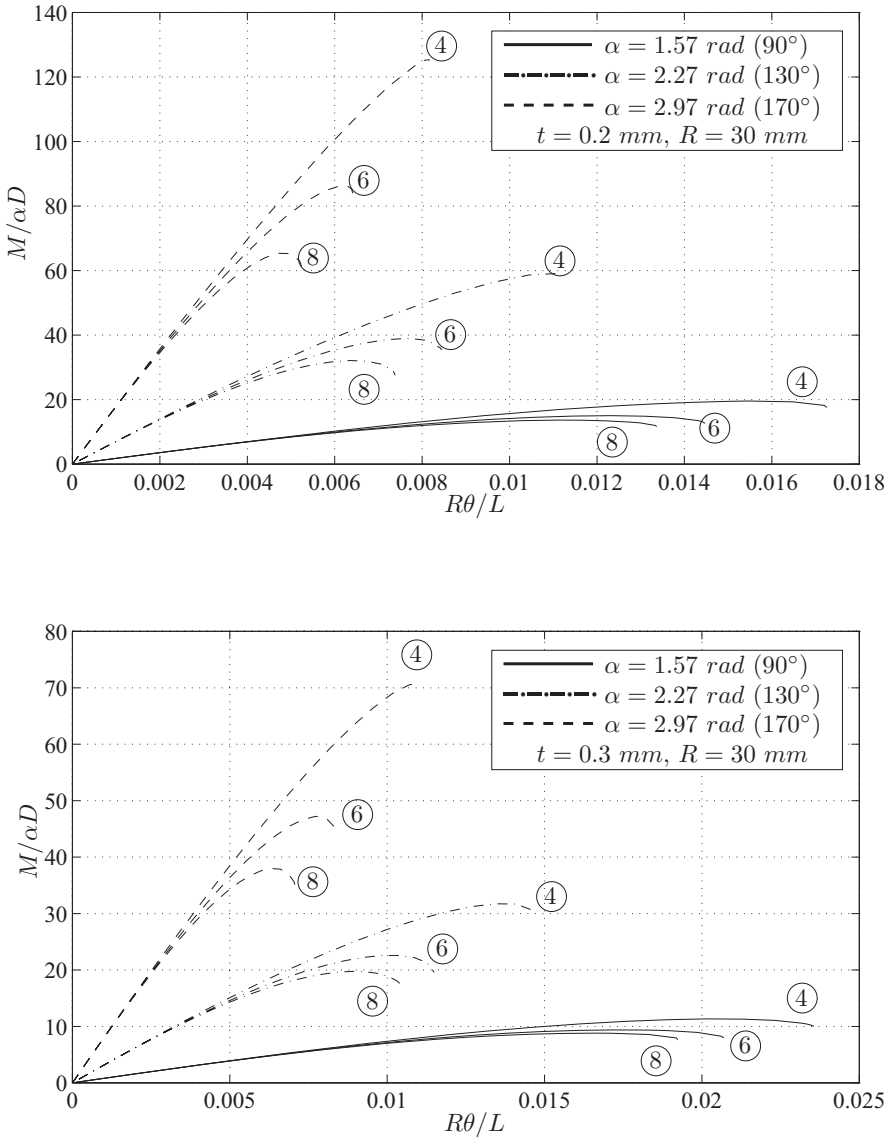

Figure A.4: Dimensionless opposite-sense bending behaviour, before buckling, for $R = 30\ mm$ and; (a) $t = 0.2\ mm$, (b) $t = 0.3\ mm$.

Appendix B

Maximum Deployment Angle of Panel

This appendix contains plots of the maximum angle that a panel can be folded to, to permit deployment without overshoot.

Figures B.1 and B.2 summarise the deployment behaviour for pairs of identical tape-springs forming a composite hinge of the indicated cross-sectional geometry.

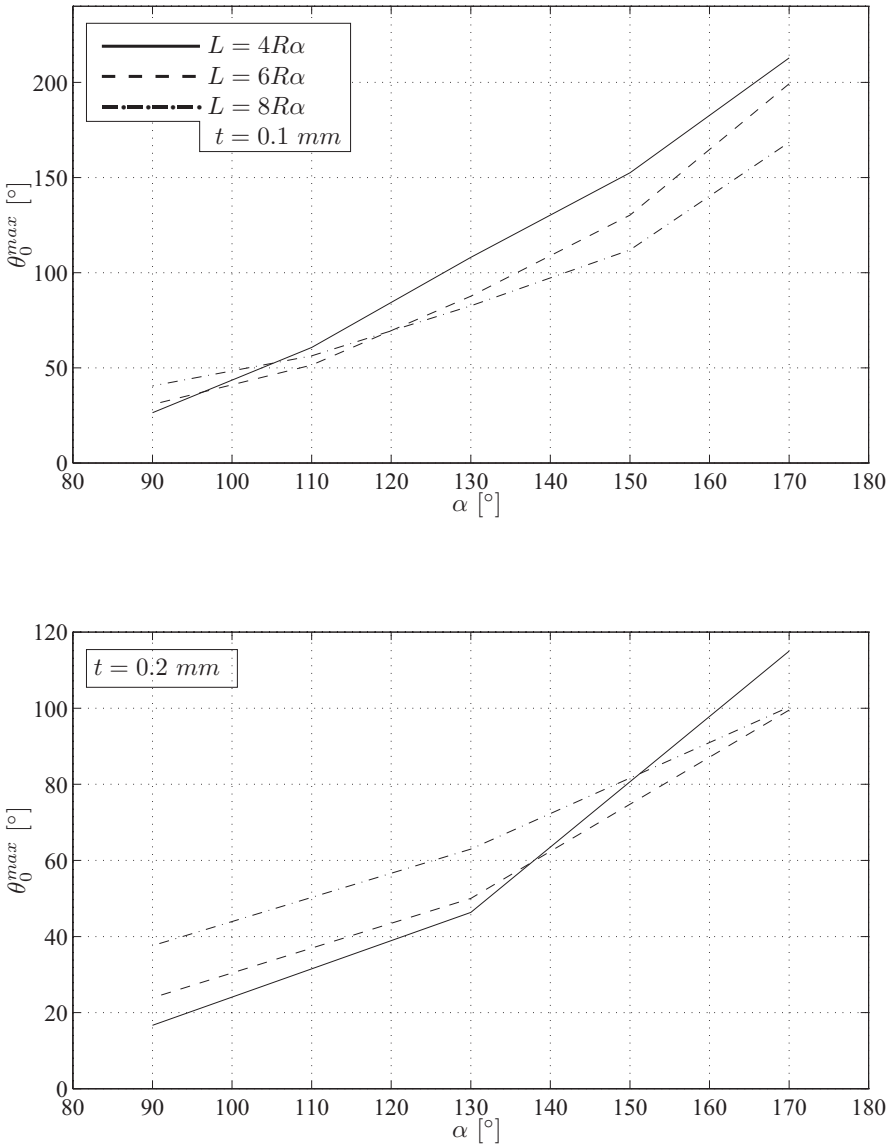

Figure B.1: Maximum deployment angle that avoids overshoot for composite tape-springs of natural radius $R = 20\ mm$.

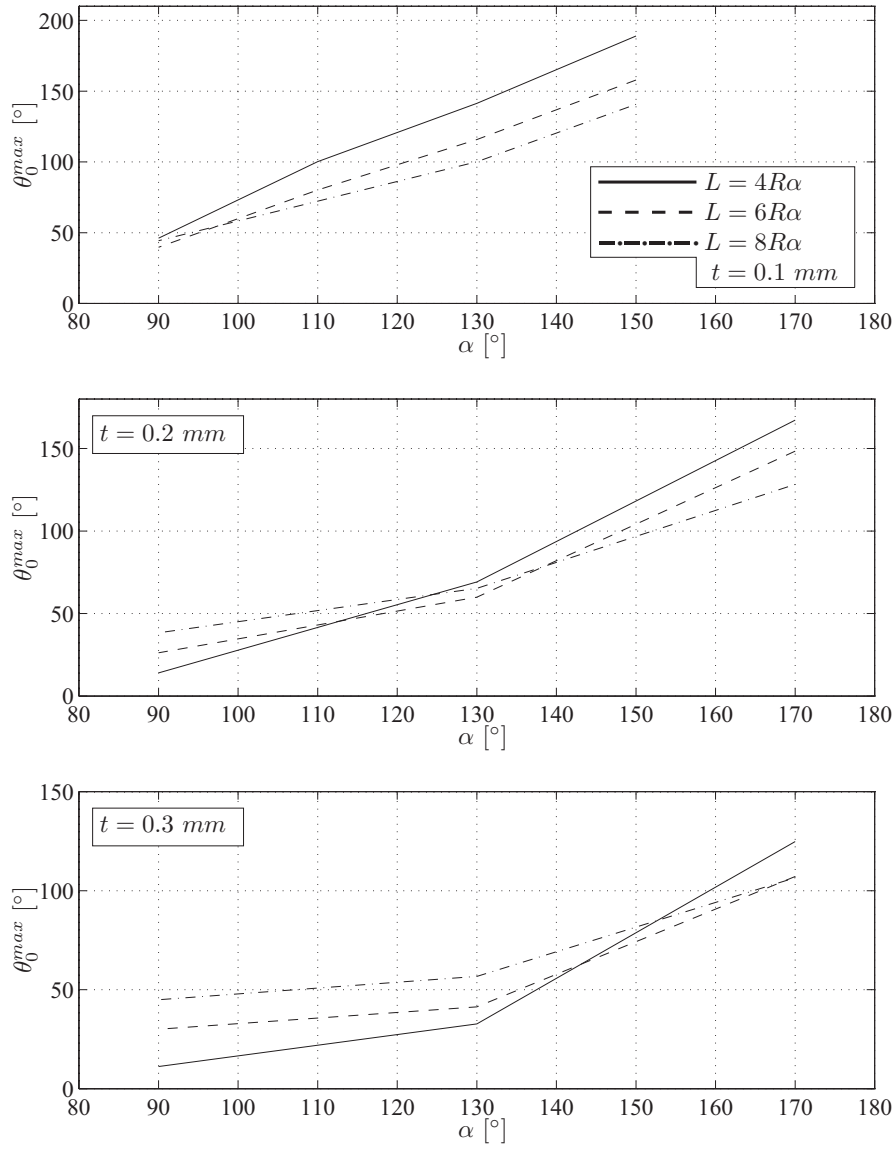

Figure B.2: Maximum deployment angle that avoids overshoot for composite tape-springs of natural radius $R = 30\ mm$.